

Simulations of Solid Oxide Fuel Cell Electrodes with Complex Microstructures

by

Hsun-Yi Chen

A dissertation submitted in partial fulfillment
of the requirements for the degree of
Doctor of Philosophy
(Materials Science and Engineering)
in The University of Michigan
2011

Doctoral Committee:

Associate Professor Katsuyo S. Thornton, Chair
Professor John W. Halloran
Assistant Professor Anton Van der Ven
Assistant Professor Charles W. Monroe
Associate Professor Stuart B. Adler, University of Washington

development specimen
phase effects
evolution experiments
fuel
SEM high
volume surface
modeling
oxygen
TPBS
transport path
simulations
electrode
structures
transport
model
length
material
boundary
end two
caption
Ni-YSZ
geometries
parameters
processes
excellent
numerical
complex
experimental
beam
reduction
compressing
anode
microstructural
cathode
examine
simulation
diagram
active
reactions
cell
structure
various
highly
microscopy
study
effect
impedance
Model
found
SBM
implementation
FIB-SEM
one
system
materials
experimentally

SOFCs
reconstruction
large-scale
approach
TPB
operation
contact
conditions
mechanism
performance
composite
usually
electron
height
properties
analysis
techniques
diffusion
LSM
electrodes
cathodes
link
porous
torquosity
method
YSZ
electrochemical
including
kinetics
stability
computational
different
oxide
facilitate
provides
reconstruction
utilization
porous
reaction
composites
provides
modeling
impedance
found
SBM
implementation
FIB-SEM
one
system
materials
experimentally

© Hsun-Yi Chen 2011

All Rights Reserved

ACKNOWLEDGEMENTS

I sincerely thank my advisor, Prof. Thornton, for her guidance and her efforts on my dissertation to warrant its quality. I would also like to thank the committee members for their useful comments and various perspectives to make this work more comprehensive. The funding support from NSF DMR-0542619 and DMR-0907070 is appreciated.

Many of my labmates in Thornton's group have been nice and helpful during my ph.D. Especially, I thank the help from Dr. Hui-Chia Yu for answering many questions that are associated with the smoothed boundary method. I would also like to thank Chal, Victor, and Nirand for many useful discussions in different subjects, and Chloe for answering many English questions.

I greatly appreciate Prof. Feak from English Language Institute-UM for her help on correcting my English in my dissertation and publications. The amount of time she invested on my manuscripts is incredible. It has been a great pleasure to work with her.

Many friends in Ann Arbor are helpful: Hsien-Kai, Yi-Hao, Sam, and many others. I especially thank Peter for his kindness and generosity. My girl friend, Ching-Fan Lin, has been standing by me during the tough period of my ph.D studies. Without her, I would never have accomplished my degree.

I am deeply in debt to my parents for their unconditional supports. During the several years of my ph.D., I did not have many opportunities to express my love and gratitude to them.

TABLE OF CONTENTS

ACKNOWLEDGEMENTS	ii
LIST OF FIGURES	v
LIST OF TABLES	xi
ABSTRACT	xii
CHAPTER	
I. Introduction	1
1.1 Thesis objective	1
1.2 Material design using microstructures	2
1.3 Microstructures in SOFC electrodes	3
1.4 Modeling of SOFCs	8
1.5 Three-dimensional microstructure reconstruction	9
1.6 Thesis overview	11
II. Multifunctionality of Three-Dimensional Composites	13
2.1 Composite materials and multifunctionality	13
2.2 Minimal surfaces and self-assembled composites	16
2.3 Tortuosity and effective transport properties	19
2.4 Results	25
2.4.1 Model validation	25
2.4.2 Transport in SD composites and minimal-surface structures	27
2.4.3 Tortuosity of experimental composite samples	32
III. Quantitative Modeling of Nickel Coarsening in SOFC Cermet Anodes	39
3.1 Nickel coarsening in SOFC anodes	39

3.2	The phase-field model	42
3.3	The smoothed boundary method	44
3.4	Descriptions of the models and methods	47
3.4.1	Model A	50
3.4.2	Model B	53
3.4.3	Nondimensionalization and asymptotic analysis	56
3.5	Numerical methods	63
3.6	Error analysis: contact angles and the interfacial width	66
3.7	Parameterization of the models	68
3.7.1	Mobility prefactors	69
3.7.2	Bulk and gradient energy coefficients	70
3.8	Initial smoothing, boundary filling, and post processing of Model B	72
3.9	3D data analysis	78
3.10	Results and Discussion	81
3.10.1	Contact angles at triple junctions	81
3.10.2	Comparison of Model A, Model B, and experimental results	82
3.10.3	Effects of contact angles at triple junctions on anode stability	85
3.10.4	Phase connectivity and TPB activity	86
3.10.5	Tortuosity of pores	92
3.10.6	The active Ni surface	93
3.10.7	Size effects and evolution kinetics	95
3.11	Conclusion	98
 IV. Simulation of Oxygen Ion Transport in Mixed-Conducting SOFC Cathodes		102
4.1	Nonstoichiometric thermodynamics of mixed conducting perovskites	102
4.2	Surface reaction mechanisms in LSC	107
4.3	Model framework of oxygen reduction and transport in LSC	109
4.4	Model implementation with the smoothed boundary method	116
4.5	Results and discussion	117
4.5.1	Smoothed boundary method validation	117
4.5.2	Oxygen vacancy concentration in the experimentally obtained LSC cathode microstructure	120
 V. Summary and Future Work		125
5.1	Summary of the thesis	125
5.2	Future Work	129
 BIBLIOGRAPHY		132

LIST OF FIGURES

Figure

1.1	Schematic diagram showing the operation of a SOFC. Oxygen is reduced at the cathode, while hydrogen is oxidized at the anode. Oxygen ions are transported from the cathode to the anode through the electrolyte. Electrons released at the anode are collected by a current collector and generate a current in an external circuit.	3
1.2	Illustration of a segment of two layers of a SOFC stack. This configuration demonstrates a counter-flow stacking in which oxygen and hydrogen flow in opposite directions. [1]	4
1.3	Comparison of 2D SEM images before and after exposure of a Ni-YSZ anode to a H ₂ environment for 4000 hours (work by Swimonis et al. [2]). The Ni phase consists of white particles that increase in size.	6
1.4	Schematic diagram showing the FIB-SEM technique that was used to acquire structural data of a SOFC electrode [3]. The FIB mills the surface of the specimen to expose cross-sections while the SEM images them.	9
1.5	The 3D microstructure reconstruction through the stacking of 2D serial images acquired via FIB-SEM [3].	10
1.6	View of a reconstructed Ni-YSZ anode using FIB-SEM [3]. The Ni phase is green, the pores are blue, and the YSZ phase is grey. . . .	11
2.1	Schwarz P (top left), Schwarz D (top right), Schoen's G (bottom left) and S (bottom right) surfaces.	19
2.2	A portion (1/64 of the computational domain in volume) of the conserved-dynamics coarsened bicontinuous structure at the dimensionless time of 179200.	20

2.3	Self-similar morphology of the SD composite characterized on the interfacial shape distribution diagram [4].	20
2.4	Self-similar topology of the SD composite characterized via genus per characteristic volume plotted versus time [4].	21
2.5	The difference of the effective flux calculated with the interpolation method and that calculated with a standard surface mesh.	26
2.6	Tortuosity factor of the SD composite as a function of coarsening time.	28
2.7	Tortuosity factors for the SD composite and minimal surfaces. . . .	29
2.8	A schematic interfacial shape distribution diagram, which is scaled by the surface area per volume S_V and shows the distribution of interfacial principal curvatures [5].	31
2.9	The microstructure of a porous alumina sample of dimensions $742.2\mu m$ by $742.2\mu m$ by $742\mu m$ (the entire sample, left), and a $(92.8\mu m)^3$ portion (right). The semi-transparent grey phase represents alumina and the blue phase illustrates pores. This alumina sample has only 23% porosity.	33
2.10	The tortuosity factor calculated using our finite-difference code versus the domain size.	35
2.11	A view of the reconstructed LSM-YSZ cathodes. Yellow represents the YSZ phase, red the LSM phase, and grey shading the pore phase. The figure on the left has 70% YSZ and 30% LSM in weight, and the one on the right has 30% YSZ and 70% LSM.	36
2.12	Tortuosity factors averaged over three axial directions at different YSZ volume fractions.	38
3.1	Normalized angle plotted with the ratio of the domain size to the interfacial width. The error decreases with an increasing ratio of the domain size to the interfacial width.	68
3.2	Comparison of microstructures of the Ni phase of a $(1.74\mu m)^3$ sample. The left figure shows the voxelated experimental data and the right figure shows the smoothed structure using Allen-Cahn dynamics (evolved for 0.8 unit of dimensionless time with grid spacing of one).	73

3.3	2D contour plots of the Ni phase of a $(1.74\mu m)^3$ sample. The axes are represented in the mesh unit, each of which equals $0.348\mu m$. The left figure shows the $z=20$ slice, and the right one represents the $z=40$ slice. White curves are the 0.1, 0.5, and 0.9 contours of the smoothed Ni OP values. The blue curves indicate the Ni interfaces of the experimental data. The 0.5 contours differ from the original Ni interfaces by less than one mesh size for the most part, which indicates that the initial smoothing generally preserves the original morphological features.	74
3.4	Moving droplet tests for the boundary filling effect on evolution dynamics. The droplet motion is driven by unequal surface tensions and the mass transport is mediated by surface diffusion. The top left figure (a) shows the initial shape of a droplet that is filled above $\psi = 0.5$ whereas the top right figure (b) shows a droplet that is filled above $\psi = 0.1$ (dashed curves are contours of ϕ). Solid lines are contours of ψ at levels 0.1, 0.5, and 0.9 (from the bottom to top). In the bottom figure, blue dash-dot curves represent the contour of the 90% filled droplet, whereas the white ones show the half-filled droplet. After 2500000 dimensionless time of evolution (with $\Delta x = 1$), the center of mass of the two droplets are nearly identical, even though the initial filling slightly altered the mass.	75
3.5	A 1D profile of the order and domain parameters from Model B simulation. The blue curve shows the profiles of ψ , green shows that of ϕ , the red curve indicates the profile of the intermediate variable ϕ' , and the white curve is the profile of ϕ_{Ni} . The profile of ϕ_{Ni} at the overlapped Ni and YSZ interfacial regions are accurately described with the proposed post processing.	77
3.6	Comparison of the microstructure (a) and TPB distributions in a $(1.28\mu m)^3$ portion of a 3D anode sample after initial-smoothing (b) (TPB density of $5.5\mu m^{-2}$), boundary filling (c) (TPB density of $5.7\mu m^{-2}$), and ten-second coarsening using Model B (d) (TPB density of $5.5\mu m^{-2}$). The Ni, pore, and YSZ phases are represented in green, semi-transparent blue, and semi-transparent grey, respectively. TPBs (light blue) are accurately identified with our post processing. While there are small changes between (b) and (c), they are not significant compared to the change of TPBs after evolving over a long time (here, 11 hrs) (e)	79

3.7	A comparison of equilibrium contact angles at triple junctions with three different models; phase 1, 2, and 3 are represented in green, gray, and blue, respectively: (A) the result of Model A; (B) the result of Model B; and (C) the result from evolving one order parameter in Model A. Note that the triple junction no longer exists at equilibrium in (C).	82
3.8	Comparison of the three phase anode before (left) and after (right) coarsening for 100 hours using Model B for the reference case. The Ni, pore, and YSZ phases are represented in green, blue, and semi-transparent, respectively (with volume fractions 26.9%, 16.6%, and 56.5%, respectively). The initial TPB density is $\sim 6.74 \mu\text{m}^{-2}$, and was reduced by 32.4% after coarsening.	83
3.9	Comparison of the TPB reduction of Model A and Model B for the reference case.	84
3.10	Comparison of the TPB reduction among three different Ni-YSZ interfacial energies using Model B.	86
3.11	Initial Ni-YSZ anode microstructure for a set of larger simulations. The dimensions of the microstructure are $4 \mu\text{m} \times 4 \mu\text{m} \times 4 \mu\text{m}$. The Ni, pore, and YSZ phases are represented in green, blue, and semi-transparent, respectively (with volume fractions 23.8%, 18.7%, and 55.4%, respectively). The initial TPB density is $\sim 5.2 \mu\text{m}^{-2}$	87
3.12	The pore volume change in three different categories over 500 hours of coarsening. The change in each category is relative to its initial value.	89
3.13	TPB density change in each category over 500 hours of coarsening. The active TPB length reduction is $\sim 89\%$ of the total TPB reduction after 500 hours.	91
3.14	Tortuosity factors in three orthogonal directions of the pore phase over 500 hours of coarsening.	93
3.15	Ni surface area reduction over 500 hours of coarsening.	94
3.16	Reduction of the Ni surface areas for three different sample sizes over 300 hours of coarsening.	95
3.17	Reduction of the Ni surface area per Ni volume for three different sample sizes over 300 hours of coarsening.	96

3.18	TPB densities for three different sample sizes over 500 hours of coarsening. The initial TPB densities of the $(3.2 \mu\text{m})^3$, $(4 \mu\text{m})^3$, and the $(4.8 \mu\text{m})^3$ samples are $5.45 \mu\text{m}^{-2}$, $5.22 \mu\text{m}^{-2}$, and $5.25 \mu\text{m}^{-2}$, respectively.	97
3.19	Numerical smoothing of Ni microstructures in Model B. The circled particle is numerically smoothed after a very short time of coarsening. (a) mean-curvature ($H = (\kappa_1 + \kappa_2)/2$) plot of Ni interfaces; (b) ISD diagram of Ni interfaces; (c) the Ni microstructure before coarsening; (d) Ni microstructure after coarsening for 3 minutes. (Figures (a) and (b) were plotted by Chal Park in Thornton's group.)	99
4.1	Basic atomic structural element of ABO_3 , which consists of a BO_6 octahedron surrounded by charge-compensating A-site cations [6].	103
4.2	The bulk path for oxygen transport following a surface reaction mixed conducting oxides. The blue color represents the oxide, grey shows the gas phase, and green indicates the electrolyte. The oxygen is completely reduced to oxygen ions on the oxide surface (a) then transported through the bulk (b) to the electrolyte (c).	110
4.3	The surface path for oxygen transport in mixed-conducting oxides. The blue color represents the oxide, grey illustrates the gas phase, and green shows the electrolyte. The oxygen is partially reduced to intermediate species on the oxide surface (a), then transport on the surface (b), and subsequently fully reduced to oxygen ions before entering the electrolyte (c).	111
4.4	A schematic diagram that describes the mass balance at a surface element on mixed conducting oxides. \mathbf{N}_v represents the bulk flux, \mathbf{N}_{O_s} is the surface flux, r_{O_2} is the surface reaction rate, and \hat{n} is the unit normal vector of the surface element.	113
4.5	A schematic diagram that describes how the domain parameter ψ is introduced in the SBM framework. The irregular shape in the middle is the LSC particle. The rectangular box is the expanded domain for SBM implementation.	117
4.6	The domain configuration for the cylindrical geometry case to demonstrate the validity of the SBM implementation of the LSC model.	118
4.7	A comparison of the analytical solution and the SBM results for a cylinder case. The nondimensional vacancy concentration is plotted versus the cylinder height normalized to the cylinder radius, z	119

4.8	A view of the FIB-SEM 3D reconstruction of the LSC cathode. The grey color represents the LSC phase (with a volume fraction of 60.9%), and the transparent space indicates the pores (with a volume fraction of 30.1%).	121
4.9	A view of the spatial distribution of the dimensionless vacancy concentration in the reconstructed LSC cathode. The color transitions from red to black, which corresponds to high to low logarithm of the concentrations. Note that the distribution is affected locally by the microstructures.	121
4.10	A view of the spatial distribution of the dimensionless vacancy concentration in the experimentally acquired LSC cathode, with an AC voltage applied at the side wall. The grid spacing is 25 nm in each axial direction. The utilization length scales inversely with $\sqrt{\kappa}$ in principle, but is affected locally by the microstructures.	122
4.11	The modeled Nyquist plot for the case where the surface transport path is not considered. Each curve contains 200 data points obtained by varying the dimensionless frequency from 0 to 210. (This work was performed by Hui-Chia Yu in Thornton's group.)	123
4.12	The spatial distribution of the dimensionless vacancy concentration in the experimentally obtained LSC cathode (without surface diffusion). Note that at a sufficiently high frequency the utilization length is restricted to a small portion of the specimen height.	124
5.1	A schematic diagram showing the finite volume scheme used in the resistor network model [7]. Each of the finite volume elements is assigned to a material property according to the microstructural configuration. The conservation of charges can then be solved with Ohm's law.	130
5.2	A schematic diagram describing how the simulation results of the 1D electrochemical model (top right) can be used as the boundary conditions for the 3D model, which employs the experimentally obtained microstructure (shown as the cube in the bottom).	130
5.3	SEM image of the textured Ni-YSZ cermet prepared by the reduction of directionally solidified NiO-YSZ eutectics. The lamellar interspacing is a function of growth rate. [8]	131

LIST OF TABLES

Table

2.1	Physical problems governed by the basic transport equations.	15
2.2	A comparison of tortuosity factors calculated from our interpolation and FD procedures for different minimal surface structures	26
2.3	A comparison of the tortuosity factors calculated from our FD procedures for different domain sizes.	34
2.4	Tortuosity factors calculated for various compositions of LSM-YSZ cathodes. The sample is represented in terms of the LSM:YSZ weight ratios. That is, sample 3070 is denoted by 30LSM:70YSZ.	37

ABSTRACT

Simulations of Solid Oxide Fuel Cell Electrodes with Complex Microstructures

by

Hsun-Yi Chen

Chair: Katsuyo S. Thornton

The goal of this research was to determine the relationship between microstructure and properties to aid microstructure analysis and design. A series of continuum modeling frameworks were developed to study microstructural effects in solid oxide fuel cell electrodes. Microstructures experimentally obtained by focused ion beam (FIB)-scanning electron microscopy (SEM) were employed.

The first study identified the characteristics that optimize competing transport in two-phase composites. A model was developed to evaluate tortuosity. It is based on the finite-difference method with regular Cartesian grids. The spinodally-decomposed two-phase composite was found to exhibit simultaneous transport properties comparable to those of optimized minimal-surface structures.

The second study focused on the development of phase-field frameworks to quantitatively model Ni coarsening in a Ni-yttria stabilized zirconia (YSZ) anode. Through asymptotic analysis, two models (A and B) differing in the treatment of YSZ were linked to experiments without fitting parameters. In both models, the contact angles at a triple junction were demonstrated to obey Young's equation. The TPB reduction

predicted by Model B, which employs the smoothed boundary method (SBM), was in reasonable agreement with experimental results, whereas Model A, which couples two Cahn-Hilliard equations, overestimated TPB reduction. The modeling results indicate that reducing the contact angle of Ni on YSZ can enhance anode stability.

In the third study, the SBM was introduced to implement a dual-transport-path electrochemical model for mixed-conducting cathodes. The simulation results were validated against the analytical solution in a cylindrical cathode with bulk transport. The utilization length of an experimentally obtained microstructure was examined. This length was found to be locally affected by microstructures. A Nyquist plot generated using a dual-transport-path simulation for the microstructure is presented. The result shows that this approach can aid the interpretation of electrochemical impedance spectroscopy results, which are usually convoluted with multiple mechanisms and microstructural effects.

These models were implemented into large-scale simulations using state-of-the-art numerical schemes and parallel computing platforms and can be employed to examine the effects of microstructures on the performance of various porous electrodes and other materials for electrochemical devices.

CHAPTER I

Introduction

1.1 Thesis objective

“There’s Plenty of Room at the Bottom,” said physicist Richard Feynman in 1959. This insight did not only lead to the revolutionary development of nanotechnology, but it also inspired researchers to examine the possibility of manipulating microstructures from the bottom to achieve excellent properties in a wide range of materials. To facilitate microstructure design, in-depth studies using advanced experimental techniques and modeling tools are needed to understand the relationship between microstructure and performance.

The aim of this thesis work was to determine the relationship between microstructure and properties by identifying the characteristics of highly optimized microstructures for competing transport, elucidating the effects of microstructure evolution on solid oxide fuel cell (SOFC) anodes during operation, and revealing the link between microstructure and electrochemical performance of SOFCs. To achieve our goals, we developed modeling frameworks that account for the physical and chemical phenomena involved in these processes pertaining to SOFC operation. In addition, contrary to many theoretical studies that are based on simplified geometries, our simulations were based on three-dimensional (3D) reconstructed microstructures to capture the effects of the microstructures that form naturally during processing. State-of-the-

art numerical methods and parallel computing techniques were applied to facilitate large-scale simulations.

We chose the SOFC electrodes as the target systems of our investigation. Important parameters in our models, including diffusivities and surface free energies, can be measured from experiments or calculated using models such as ab initio calculations or Monte Carlo simulations. These developed models and numerical tools are not limited to SOFCs; they can be applied to study various electrochemical systems.

1.2 Material design using microstructures

Numerous experimental studies aiming at improving material performance via microstructure optimization have focused on microstructural characterizations using traditional experimental techniques, such as scanning electron microscopy (SEM), transmission electron microscopy (TEM), and X-ray diffraction (XRD), and novel techniques, such as atom probe microscopy, X-ray computed tomography (CT), and focused ion beam-SEM (FIB-SEM) tomography, to correlate material properties with performance. With the recent advances in computer technology, simulations can now play an important role in microstructure design. Computational methods, such as the first principles approach, Monte Carlo methods, and phase-field models, are commonly applied to calculate the properties of materials and simulate physical processes. Along with the development of protocols and architectures of parallel computing, a new trend that consists of connecting computational models of different length and time scales has emerged. The approach of multi-scale computational material science has enabled researchers to link atomic- and micron-scale phenomena to their apparent continuum-scale effects. Such advancements allow more quantitative predictions of component performance based on the materials comprising them. They are therefore key foundations in computational material design.

1.3 Microstructures in SOFC electrodes

Limited natural resources and environmental deterioration are driving the pursuit of clean energy. In this pursuit, SOFCs have emerged as one of the most promising clean energy devices for medium- to large-scale electricity generation because of their high conversion efficiency, fuel flexibility, superior tolerance against poisoning, and low pollutant emissions.

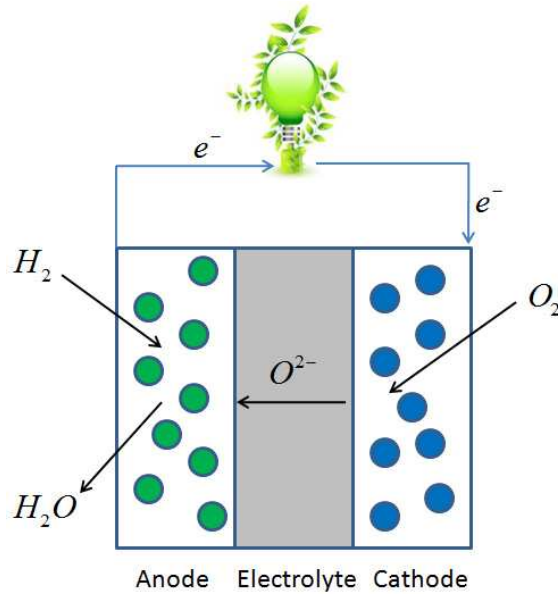


Figure 1.1: Schematic diagram showing the operation of a SOFC. Oxygen is reduced at the cathode, while hydrogen is oxidized at the anode. Oxygen ions are transported from the cathode to the anode through the electrolyte. Electrons released at the anode are collected by a current collector and generate a current in an external circuit.

The pursuit of commercially viable SOFC has necessitated numerous studies of performance improvements and cost reduction. For example, the polarization resistance has been dramatically reduced over the years by making the electrolyte thinner [9]. As such fabrication techniques are becoming more mature, microstructural design has become one of the focal points of recent developments. Higher efficiency, longer component lifetime, and lower operating temperatures of SOFCs may be achieved by optimizing microstructures. Until recently, one major obstacle to

advances in microstructural optimizing was the lack of 3D microstructure data. The development of 3D characterization techniques such as FIB-SEM has removed this impediment. To illustrate how the 3D reconstructed microstructures are acquired by this technique and how to incorporate the acquired to SOFC studies, a brief introduction to FIB-SEM is given in Sec. 1.5 .

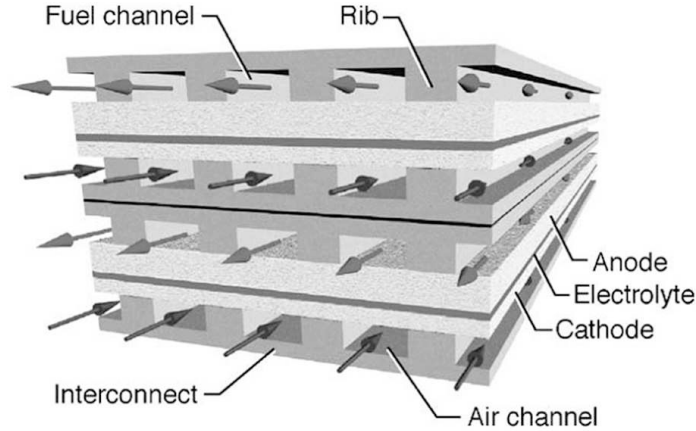
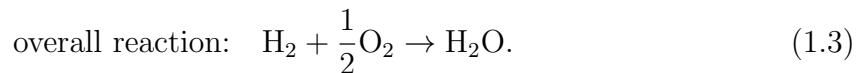
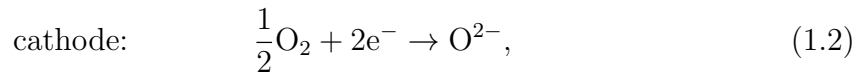
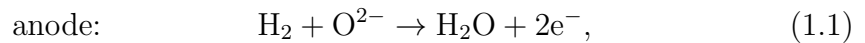


Figure 1.2: Illustration of a segment of two layers of a SOFC stack. This configuration demonstrates a counter-flow stacking in which oxygen and hydrogen flow in opposite directions. [1]

The operation of a SOFC is schematically described in Fig. 1.1. The electrochemical reactions involved when the feeding gases are H_2 and O_2 are



As shown in Fig. 1.2, a SOFC stack is composed of four essential components: an anode, an electrolyte, a cathode, and an interconnect. The interconnect is responsible for connecting the cells in series so that their output electricity can be combined. The electrolyte is a dense layer of ceramics that conducts oxygen ions while blocking the electrons from crossing over. At the anode, hydrogen or other hydrocarbon

fuels are oxidized, and electrons are released and transported out along with water vapor or other products. Oxygen molecules are reduced to oxygen ions at the cathode by gaining electrons supplied from the external circuit. Thus, the electrodes in SOFCs serve to transport reactants and products and facilitate electrochemical reactions. This multifunctionality requirement usually necessitates SOFC electrodes to be made of composite materials having microstructures with complex morphologies. When optimized microstructures are designed and utilized in anodes and cathodes, it is thought that electrochemical efficiency and stability can be greatly improved in SOFCs [10, 11, 12]. To gain insight into the effects of microstructures on transport properties, we developed a numerical model to evaluate the transport properties in a multi-phase composite, which is discussed in Chapter 2.

Due to economical and performance considerations, the most commonly used anode to date is a ceramic-metal composite (cermet) of Ni and yttria-stabilized zirconia (YSZ). In a Ni-YSZ anode, the electrochemical reaction of fuel oxidization occurs in the vicinity of three-phase boundaries (TPBs), where the Ni, YSZ, and pore phases are in contact. The Ni-YSZ anode is thus usually designed so that a complex microstructure is formed and the density of electrochemically active sites is increased. However, the intricate anode microstructure tends to coarsen, which results in degradation of the Ni-YSZ anode.

As shown in Fig. 1.3, a typical microstructural evolution in a Ni-YSZ anode is the coarsening of Ni particles. Simwonis et al. [2] have reported a 26% increase in the average Ni particle size by evaluating two-dimensional (2D) images of a Ni-YSZ anode after exposure to a H_2 environment at $1000^\circ C$ for 4000 hours. Although the quantitative values they measured may be debatable due to the 2D nature of their analysis, there is no doubt that Ni particles substantially coarsen during SOFC operations. One challenge facing experimental investigation of the effects of Ni particle coarsening is the time-consuming nature of the investigation, resulting from the ten-to-fifteen-year

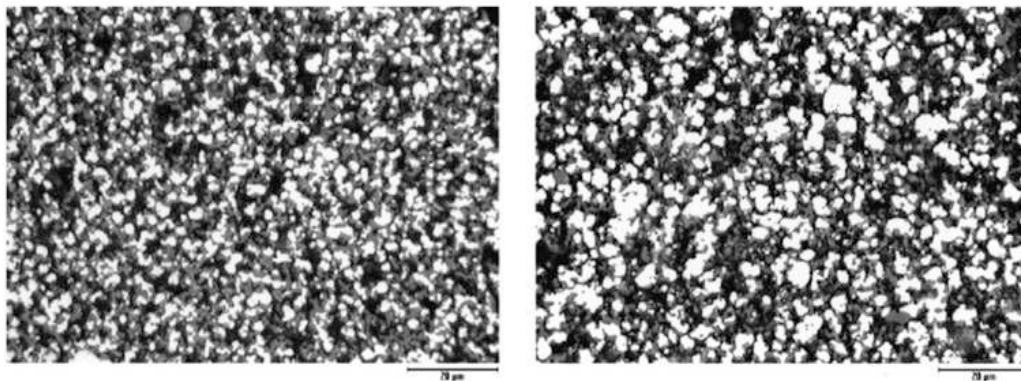


Figure 1.3: Comparison of 2D SEM images before and after exposure of a Ni-YSZ anode to a H_2 environment for 4000 hours (work by Swimonis et al. [2]). The Ni phase consists of white particles that increase in size.

lifetime target of SOFCs. Furthermore, a 3D microstructural characterization is typically labor intensive. Difficulties in the preparation of consistent samples, as well as in the maintenance of precisely controlled environments during long-time experiments, pose additional challenges to understanding the processes that lead to microstructural evolution. However, modeling offers an advantage, allowing systematic investigations of the coarsening process and its effect on the SOFC Ni-YSZ anode performance. To model the Ni coarsening, we propose a phase-field framework that is discussed in Chapter 3.

SOFC cathodes are also made of composite with a rich variety of microstructures. Cathodes can lead to a significant polarization resistance to SOFCs because of slow oxygen-reduction kinetics. To accelerate oxygen reduction, SOFCs are usually operated at high temperatures. However, high-temperature operations also lead to rapid degradation of SOFC components, thus limiting the materials that can be used for SOFCs. For instance, interconnects, which are exposed to both cathodes and anodes, have to simultaneously sustain severe oxidizing and reducing environments. Materials that are sufficiently stable in such environments at high temperatures are generally expensive. Decreasing the operating temperature to an intermediate level ($500 \sim 700^\circ\text{C}$) has therefore become one of the most important goals of recent SOFC

studies [13]. The key to reducing the operating temperature of SOFCs to an intermediate range is to improve the kinetics of cathodic reactions via material design.

Current commercial SOFC cathodes are composites of porous lanthanum strontium manganite (LSM). LSM is utilized because of its high mechanical compatibility with YSZ electrolytes; however, its poor ionic conductivity confines oxygen reduction reactions to a region close to the one-dimensional TPBs where the electrolyte is in contact with both the LSM and the pores. Therefore, in some cases, composites of LSM, YSZ, and pores are utilized to extend the TPBs. Electrochemically active sites can also be extended to 2D surfaces when mixed conductors that conduct both electrons and oxygen ions, such as transition-metal perovskite oxides, are used to replace the primarily electron-conducting LSM as the cathode material. If the electrochemical activity, especially the oxygen reduction kinetics, of the cathode composite can be enhanced in this manner, it should most likely allow decreased operating temperatures to be used.

Although mixed conducting oxides are promising cathode materials for intermediate-temperature SOFCs, their oxygen exchange mechanisms, which include the reactions and the transport processes, are complicated by the presence of various possible intermediates and reaction paths. Both nonstoichiometric thermodynamics [14, 15] and reaction kinetics [16] of the mixed conducting oxides have been studied. Among the experimental techniques used to investigate these oxides, electrochemical impedance spectroscopy (EIS) offers valuable information about the reaction kinetics, including the identification of dominant mechanisms for oxygen reduction (e.g., Ref. [17]). However, there is usually no unique interpretation for an impedance spectrum measured by EIS because EIS measurements are convolutions of multiple factors, such as physical and chemical mechanisms and microstructures. Instead of directly identifying individual mechanisms, which can be a major challenge, EIS results can also be fit to obtain parameters of electrochemical models (e.g., Ref. [18]) or to exclude

certain mechanisms (e.g., Ref. [19]). Specifically, when microstructures significantly affect oxygen exchange mechanisms (for example, when the utilization length of the cathode is shorter than or comparable to the characteristic microstructural length), such electrochemical models are indispensable for analyzing complex EIS data. In Chapter 4, we discuss how EIS can be simulated with complex geometries using the framework of the smoothed boundary method.

1.4 Modeling of SOFCs

Since modeling can provide invaluable guidance for system design, researchers have developed numerous models to study the physical and chemical processes in SOFCs. In very general terms, these models can be categorized into stack-level, intermediate-level, and microscopic models. To assist system design, stack-level models consider fluid flow, heat transfer, and chemical reactions within the entire SOFC stack [20, 21, 22]. In the case of intermediate-level models, mass and charge balances are modeled within the scope of single cell unit, which usually includes the electrode and the electrolyte components [23, 7, 24]. Microscopic models usually focus on the reaction kinetics in the vicinity of the TPBs [18, 25]. Regardless of the type of model, microstructures are usually represented by characteristic parameters, including porosity, permeability, and tortuosity, which may be acquired from empirical models, such as the random packing theory, or from experimental measurements. However, such a coarse-grained description of microstructures may not lead to an accurate prediction of the material responses of multifunctional composites, and thus must be validated by more detailed models.

1.5 Three-dimensional microstructure reconstruction

The usage of simplified geometries and empirical models in SOFC modeling can partly be attributed to the inability to acquire 3D microstructural information, and to the computational complexity of simulating intricate microstructures, such as highly connected, tortuous pore networks. For example, tortuosity cannot be measurable simply based on 2D images because it depends on phase interconnectivity in the 3D space. Additionally, in a multiphase porous electrode, the surface area of a specific phase can be difficult to determine experimentally, e.g., using a Brunauer-Emmett-Teller (BET) analysis.

To address this problem, a method that consists of integrating a focused ion beam (FIB) with a scanning electron microscope has been proposed [26]. This dual-beam microscope couples a destructive ion beam with a nondestructive electron beam. The ion and electron beams can either be simultaneously focused on the same point of the specimen, or operated independently. The ion beam sequentially mills the surface of the specimen while the electron beam serves to image the exposed surface. FIB-SEM has thus been widely used in materials research given its ability to provide 3D images of embedded features or defects of a material.

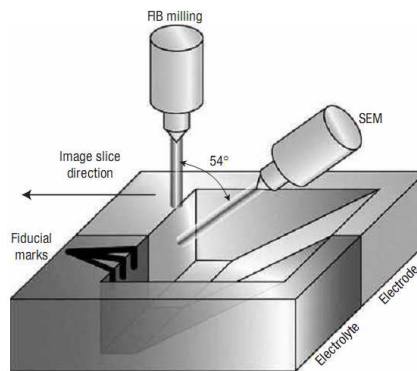


Figure 1.4: Schematic diagram showing the FIB-SEM technique that was used to acquire structural data of a SOFC electrode [3]. The FIB mills the surface of the specimen to expose cross-sections while the SEM images them.

Because the FIB-SEM technique is automated, a streamline throughput of the

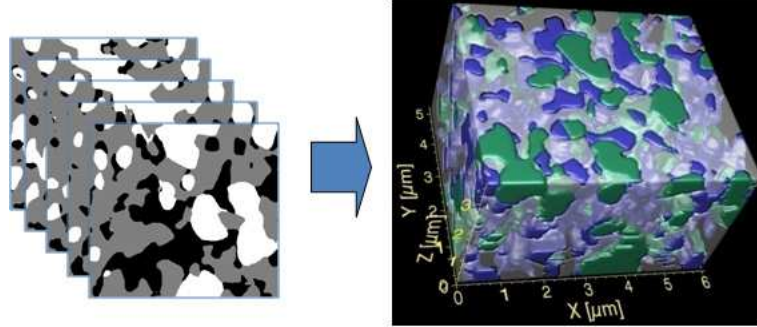


Figure 1.5: The 3D microstructure reconstruction through the stacking of 2D serial images acquired via FIB-SEM [3].

images can be acquired in a timely manner [27, 26]. The FIB-SEM has been used for 3D microstructural reconstructions by processing series of 2D images. The procedures for acquiring 2D sequential images and obtaining a 3D reconstruction of a SOFC electrode by FIB-SEM are schematically shown in Figs. 1.4 and 1.5. They are explained in more detail in [3].

Brifely, a SOFC cell specimen is first cut and cleaned to expose the electrode-electrolyte cross-section. FIB is used to mill a thin layer of the exposed cross-section, and SEM is used to images cross-section contrasts between different phases. The FIB milling and SEM imaging processes are continued until an appropriate number of 2D image slices are obtained. The final 3D reconstruction is given by stacking the 2D SEM images in sequence. An example of a 3D reconstructed Ni-YSZ anode is shown in Fig. 1.6. To obtain an accurate 3D reconstruction using FIB-SEM, through image cleaning and contrast adjusting, as well as proper image alignment, may be required. One limitation of the FIB-SEM technique is that it destroys the specimen during the procedure, which eliminates the possibility of further study on the same specimen.

FIB-SEM nevertheless provides valuable structural information, such as phase connectivity and tortuosity, which are nearly impossible to acquire from 2D tomography. The gathered 3D structural information can be used to examine the validity of macrohomogeneous assumptions or empirical theories. In this study, the 3D mi-

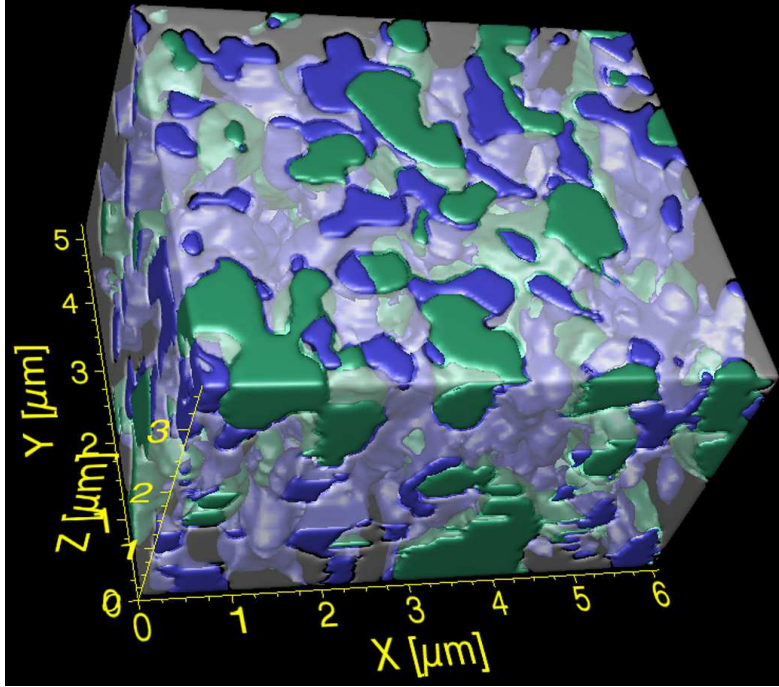


Figure 1.6: View of a reconstructed Ni-YSZ anode using FIB-SEM [3]. The Ni phase is green, the pores are blue, and the YSZ phase is grey.

crostructural data also serve as initial conditions for our simulations to investigate microstructural effects on material properties.

1.6 Thesis overview

This thesis contains five chapters: (1) Introduction; (2) Multifunctionality of Three-Dimensional Composites; (3) Quantitative Modeling of Nickel Coarsening in SOFC Cermet Anodes; (4) Simulation of Oxygen Ion Transport in Mixed-Conducting SOFC Cathodes; and (5) Summary and Future Work.

Chapter 2 discusses the transport properties of 3D, two-phase composites including minimal-surface structures and spinodally-decomposed structures that exhibit excellent simultaneous, competing transport properties. The tortuosity factors of these structures are evaluated using numerical simulations and compared. A similar model is then employed to evaluate the transport properties of experimentally ob-

tained 3D microstructures of composite specimens. The important characteristics of microstructures that lead to enhanced multifunctionality are identified.

Chapter 3 focuses on the study of Ni coarsening in a Ni-YSZ anode. Phase-field models were developed to simulate coarsening of Ni via surface diffusion; experimentally obtained 3D Ni-YSZ anode microstructures are used as initial conditions. Two models that differ in the treatment of the YSZ phase are discussed. An asymptotic analysis is performed to rigorously correlate the simulation and experimental results. Valuable insights into microstructure design for robust anodes are obtained through the analysis of coarsening simulation results, such as the effect of the contact angle on the kinetics of coarsening and stabilization of microstructures.

In chapter 4, the smoothed boundary method (SBM) is utilized to implement a coupled electrochemical-transport model for mixed-conducting SOFC cathodes. The nonstoichiometric thermodynamics, reaction kinetics, and transport mechanisms that yield this model are reviewed. The validity of the SBM implementation is demonstrated by comparing the SBM results with analytical solutions. The effect of microstructures on the utilization length was studied using an experimentally obtained 3D microstructure of a cathode. It is discussed in this chapter.

In chapter 5, the overall contribution of this work is summarized and possible future work is suggested.

CHAPTER II

Multifunctionality of Three-Dimensional Composites

2.1 Composite materials and multifunctionality

The demand for alternative energy solutions has accelerated the pursuit of materials with excellent properties. For example, the electrodes in solid oxide fuel cells must transport multiple species simultaneously to facilitate the electrochemical reactions involved in fuel-cell operation. The ability to support multifunctionality is a clear advantage of composites over natural materials, which can typically be good conductors for either electrons or ions, but not both, in their natural state. Composite materials have begun attracting increasing attention because of their potential for multifunctionality. Hence, hybridizing multiple materials into composites to achieve multifunctionality has become a logical solution in many applications. Furthermore, composite materials play an important role in a wide variety of applications including high-tech electronics, medicine, and defense, in which they are used to improve the performance of materials beyond those of the constituents and to reduce the use of scarce materials, such as precious metals.

In many cases, the fabrication of suitable composites is a trial-and-error process, because the effective properties of the composite depend not only on the inherent

properties of the constituents but also on the geometric distributions of these constituents. Interestingly, the search for composites with optimal properties has opened new doors for the development of many theories and mathematical methods [28].

Given the additional freedom of microstructural control in composite materials, theoretical bounds for effective bulk properties have been extensively studied. In one early study of isotropic two-phase composite materials, Hashin and Shtrikman (hereafter, HS) obtained effective property bounds from variational theorems [29]. These bounds, herein referred to as the HS bounds, apply when constraints on the volume fractions exist and when the bulk property of each phase is given. Bergman further constrained the effective property bounds by considering an additional bulk property for a two-phase composite with either isotropic or cubic symmetry [30]. This type of theoretical bound is referred to as a cross-property bound. Cross-property bounds without symmetry constraints were derived by Prager, who examined variational inequalities [31].

Instead of searching for theoretical bounds, Torquato *et al.* adapted the topology optimization method [32] for the multifunctional optimization of three-dimensional (3D) composites [33]. To illustrate their methodology, they considered two different transport properties in a single-length-scale binary composite system: scalar electrical conductivity, σ , and scalar thermal conductivity, λ . In their competing-transport (“ill-ordered”) scenario, phase 1 has a high thermal conductivity, but low electrical conductivity, whereas phase 2 has a low thermal conductivity, but high electrical conductivity ($\sigma_1/\sigma_2 < 1$ and $\lambda_1/\lambda_2 > 1$). They discovered that bicontinuous structures having interfacial morphologies identical to the triply periodic minimal surfaces maximize the sum of the two competing conductivities when the volume fractions of the two phases are equal [33, 34]. It has been debated whether minimal-surface structures only closely approximate the optimized structures in the ill-ordered scenario and whether the optimization landscape is nearly flat, i.e., many structures with or

without minimal surfaces are close to optimal [35]. However, experimentally created microstructures are diverse in character and have correspondingly different effective transport properties. Therefore, the role of interfacial morphologies in facilitating multifunctionality deserves further study.

In this study, we investigate only the average properties governed by a generic transport equation that applies to electrical conduction, thermal conduction, and diffusion, with a consideration to the structural effects on these properties in two-phase composites. The basic transport equations are as follows [28]:

$$\begin{aligned}
 \mathbf{J}(\mathbf{r}) &= \sigma(\mathbf{r})\mathbf{F}(\mathbf{r}), \\
 \nabla \cdot \mathbf{J} &= 0, \\
 \nabla \times \mathbf{F} &= 0,
 \end{aligned}
 \tag{2.1}$$

where \mathbf{F} is the imposed field or driving force for transport, \mathbf{J} is the resulting flux, and σ is a linear constant that represents the mobility of the transported quantity (e.g., electric charge, heat, or mass). The last equation in Eq. 2.1 is automatically satisfied when \mathbf{F} is a gradient of another field (e.g., electric field, temperature, or concentration). The physical problems and properties considered here are summarized in Table 2.1.

Function	J	F	σ
Electrical conduction	Electrical current	Electric field	Electrical conductivity
Thermal conduction	Heat flux	Temperature gradient	Thermal conductivity
Diffusive transport	Mass flux	Concentration gradient	Diffusion coefficient

Table 2.1: Physical problems governed by the basic transport equations.

2.2 Minimal surfaces and self-assembled composites

Since Plateau’s soap-film experiments in the 19th century [36], the existence of minimal surfaces has been widely known. These surfaces were found to form triply periodic networks by Schwarz [37] and his contemporaries [38, 39]. More infinite periodic minimal surfaces (IPMS) were later modeled and photographed by Schoen [40]. IPMS are a paradigm of interfaces that appear in various naturally-formed cubic bicontinuous structures: equilibrium bicontinuous structures in lipid-water-amphiphile systems under certain intermediate ratios of subvolumes (for example, 40% to 60% for simple cubic symmetry) [41], domain structures in phase-separated diblock copolymers with volume fractions in a certain range (27% - 38% for diamond cubic symmetry) [42], and surfactant layers in aqueous solutions [43].

Studies of IPMS have been revived in recent decades due to their potential applications in nanostructure formation. The manipulation of nanostructures can be achieved in organic or inorganic materials with synthetic chemistry [44]. For example, self-assembled templates for nanofabrication have been demonstrated in systems of block co-polymers [44], thermally-annealed supramoleculars [45], and microemulsions of surfactants [46, 47]. The potential applications of nanofabrication include photonic crystals [48], nano-fibrous scaffolds [49, 50], and other nanocomposites [51]. As a result of the balance between interfacial tension and entropic effects, many of the minimal-surface structures emerge on the phase diagrams of these nanostructured materials [47]. A theoretical understanding of the origins of these periodic structures and their stability would serve to guide nano-composite design.

To facilitate studies of IPMS, a systematic approach that generates these periodic structures is crucial. However, few analytical representations for minimal surfaces are known. These can be derived from Weierstrass equations in terms of elliptical integrals [52], but these integrals are rather difficult to evaluate. Fortunately, the advance of numerical methods eases the construction of minimal surfaces. The numerical pro-

cedure that is commonly used is based on the framework of a Ginzburg-Landau model of microemulsions for ternary amphiphilic systems [53]. With an initial configuration that satisfies the approximate spatial distribution and the symmetry requirement, the curvature minimizing model generates a specific minimal surface. This initial approximation can either be obtained from the arrangement of density distribution in real space [53], which is rather tedious, or from the Fourier series combined with group theory [52]. We utilized the latter for our investigations.

To generate minimal surfaces, we adopt the Fourier expression approach to arrange the initial conditions for the curvature-minimizing model. The Fourier expression for minimal-surface generation is inspired by the exploration of zero potential surfaces (POPS) in ionic crystals [54, 55]. These POPS are invariant to the exchange of positive and negative point charges so that the symmetry information is contained. Their roots define a periodic nodal surface (PNS), which corresponds to certain known periodic minimal surfaces. These PNS with succinct Fourier expressions are found to be particularly useful for periodic-minimal-surface generation. For certain PNS, an improvement has been made in Ref. [52] so that these enhanced PNS better resemble the corresponding periodic minimal surfaces.

A minimal surface is an embedded surface that has a vanishing mean curvature at each point on the surface [37]. It has been shown that the coarsening of structures with minimal surface morphologies creates instability at unequal volume fractions if no effects other than capillarity drive the evolution of these systems [56]. Thus, minimal-surface bicontinuous structures are only thermodynamically favored in certain natural systems that possess length-scale constraints and have volume fractions in intermediate ranges. Fabricating microstructures with minimal-surface morphologies is therefore challenging, often requiring special material processing techniques [57].

In spite of the desirable properties exhibited by minimal-surface structures, an explanation has only been offered for Stokes flow through them [58], and the role of

minimal surfaces in competing transport has not been elucidated. A question arises as to whether we gain insights into the optimization of simultaneous transport by examining the role of interfacial morphologies in transport. The optimal structure for simultaneous transport is not unique in 3D composites. Instead, it depends on the constraints imposed. For example, Torquato *et al.* found the Schwarz P surface (Fig. 2.1, top left) to be the optimal structure in the competing transport scenario when they imposed phase inversion-symmetry, equal volume fractions, and simple cubic symmetry [33], whereas the Schwarz D surface (Fig. 2.1, top right) was the optimal structure when the diamond lattice symmetry was imposed [34]. Their findings beg the question: can any other two-phase composite morphologies that can be easily engineered facilitate simultaneous transport?

Recently, through large-scale simulations, Kwon *et al.* [4] found that coarsening subsequent to phase separation yields bicontinuous structures (Fig. 2.2) that evolve in a self-similar fashion; that is, the structure, when scaled by the characteristic length, becomes time independent in terms of both morphological (Fig. 2.3) and topological (Fig. 2.4) characteristics.

Interestingly, at equal volume fractions these bicontinuous structures evolve in such a way that the *average* mean curvature is zero. Although there is no short-range periodicity or symmetry in these structures (because the computational domains are large), the bicontinuity and zero *average* mean curvature suggest that they may have transport properties similar to those of minimal-surface bicontinuous structures. If these self-assembled composite structures have transport properties that are advantageous for certain applications, the fabrication processes of these materials can be simplified. For example, these bicontinuous composites can be self-assembled via spinodal decomposition. Spinodal decomposition is commonly observed in a wide range of materials including polymers and metals, and it is also relevant in sol-gel processing that creates complex composite structures in oxides [59, 60]. We therefore

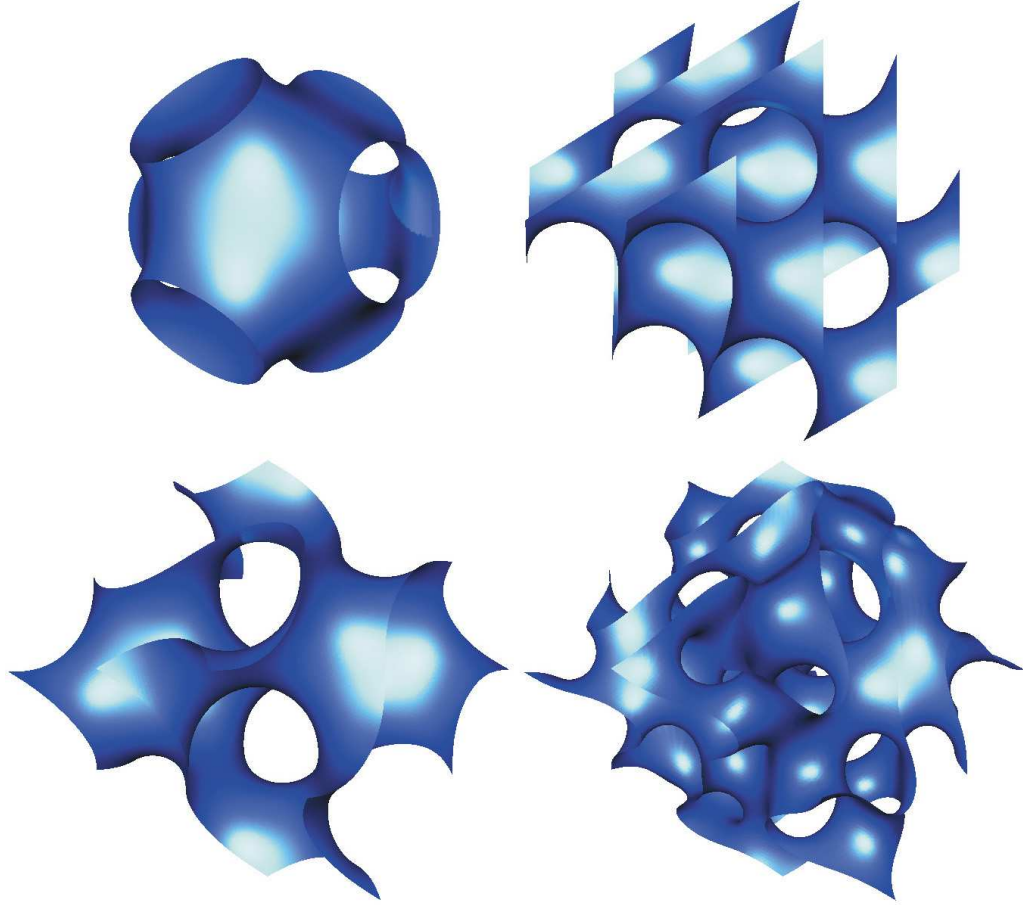


Figure 2.1: Schwarz P (top left), Schwarz D (top right), Schoen's G (bottom left) and S (bottom right) surfaces.

evaluate the transport properties of these bicontinuous two-phase composites formed via spinodal decomposition, which are hereafter referred to as the SD composites.

2.3 Tortuosity and effective transport properties

The tortuosity factor measures the geometric aspect of the transport properties of the concerned structural material. Taking porous materials as an example, the tortuosity factor κ is defined as

$$\kappa = \frac{D\epsilon}{D_{eff}} \approx \left(\frac{L_e}{L}\right)^2 = \tau^2, \quad (2.2)$$

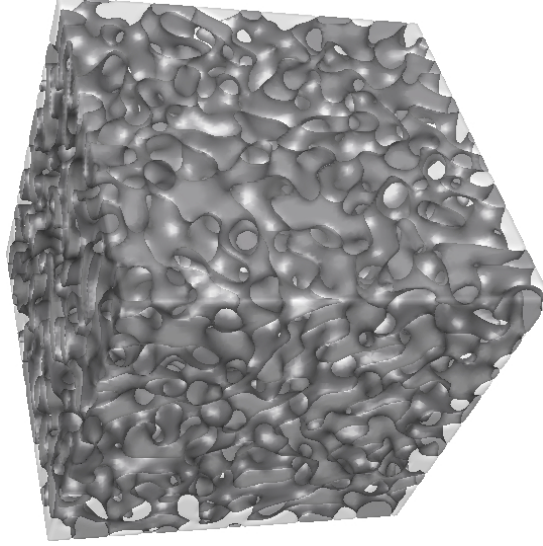


Figure 2.2: A portion (1/64 of the computational domain in volume) of the conserved-dynamics coarsened bicontinuous structure at the dimensionless time of 179200.

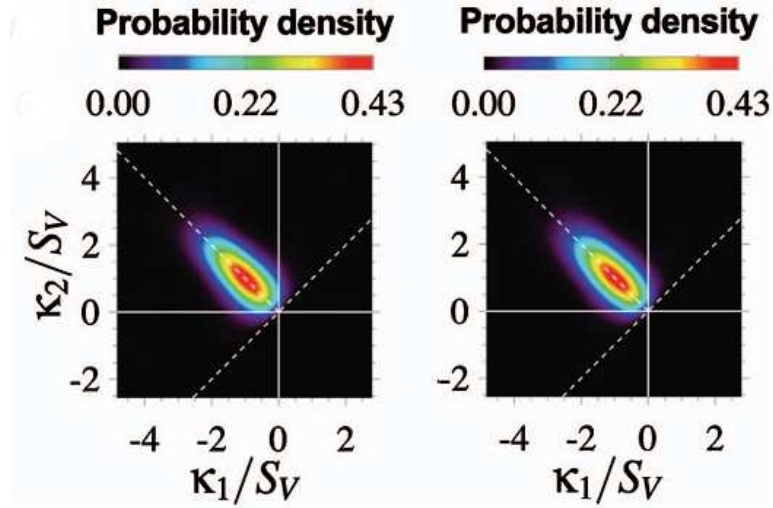


Figure 2.3: Self-similar morphology of the SD composite characterized on the interfacial shape distribution diagram [4].

where D_{eff} is the effective diffusivity in the porous medium, and ϵ is the volume fraction of the porous phase. L_e is the cumulative effective path length that a diffusing molecule takes to diffuse a length L (measured point-to-point through the medium) and τ is the tortuosity. D is the equivalent diffusivity of the diffusing molecules within the porous phase.

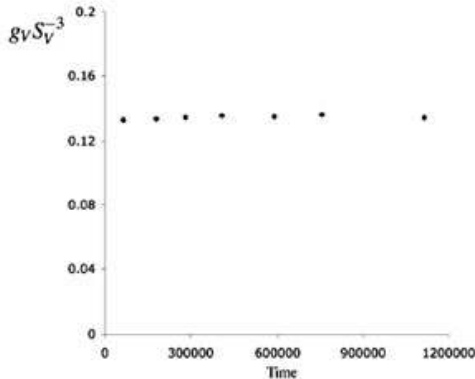


Figure 2.4: Self-similar topology of the SD composite characterized via genus per characteristic volume plotted versus time [4].

Due to the effects of different diffusion mechanisms, the equivalent diffusivity is typically described by the Bosanquet equation:

$$D \approx \left(\frac{1}{D_b} + \frac{1}{D_K} \right)^{-1}. \quad (2.3)$$

The Bosanquet equation indicates that the equivalent diffusivity D is the harmonic mean of bulk diffusivity D_b and Knudsen diffusivity D_K . Knudsen diffusion occurs when the mean free path of molecules is relatively large compared to the pore dimensions, which results in molecules frequently colliding with pore walls. In contrast, bulk or Fickian diffusivity occurs when the mean free path of molecules is relatively small in comparison to the pore size.

The tortuosity factor is intended and defined to reflect purely the geometric characteristics of the porous medium; however, various computational and experimental studies [61, 62] reported that tortuosity factors depend on the mechanism of diffusion. Specifically, the tortuosity factor has often been found to be larger for Knudsen diffusion than bulk diffusion. This contradiction has recently been reconciled for pore fractions of 0.1 to 0.42 [63]. In this work, effective diffusivities for Knudsen numbers of 10^{-3} to 10^{10} were examined using Monte Carlo simulations. A corrected Knudsen diffusion length scale proposed by Derjaguin was used in [63] to demonstrate the fact

that tortuosity factors are independent of diffusion mechanisms for pore fractions above 0.15. Even at a pore fraction of 0.1, the tortuosity factors for the two extreme diffusion regimes were found to differ by less than 18%. Therefore, whereas our study focus on Fickian diffusion, the results are applicable to cases where Knudsen diffusion plays a role for a wide range of microstructures having a volume fraction greater than 10%.

We assume that transport within the porous medium obeys Fick’s law. Thus, we can calculate the tortuosity factor by simulating steady-state diffusion. In this case, the transport can be described by Laplace’s equation

$$\frac{\partial u}{\partial t} = D\nabla^2 u = 0, \tag{2.4}$$

where u represents the concentration of the transporting quantities.

In practice, for the general transport case, the no-flux boundary condition at the transporting-nontransporting interface (internal boundary) is replaced by setting the transport coefficient in the non-transporting phase to be much smaller (by three orders of magnitude) than that in the transporting phase and solving

$$\nabla \cdot (D(\vec{r})\nabla u) = 0, \tag{2.5}$$

where $D(\vec{r})$ is the position-dependent transport coefficient. Although a large ratio of the transport coefficients of the transporting to non-transporting phases is more consistent with the assumption of the model, we take relatively small ratio because a large ratio leads to a numerical instability that unnecessarily requires more computational resources. The test results using artificial microstructures showed that using a factor of 100 between the two transport coefficients ensures that the results are not significantly altered by this approximation. More details are given below.

The tortuosity is then recovered by equating the macrohomogeneously defined flux

with the volume-average flux within the sample volume:

$$-\frac{\epsilon}{\kappa} \frac{\partial u_{MF}}{\partial x_i} = -\frac{1}{V} \int_V \frac{\partial u}{\partial x_i} dV, \quad (2.6)$$

where V is the sample volume. This procedure is performed for the three primary axes $x_i = x, y, z$ of the sample volume to determine the anisotropy of the tortuosity factor. The volume averaging is performed on the right-hand side of Eq. 2.6 to avoid the unevenly distributed flux. The (external) boundary conditions on the sample boundaries are given as follows. For the tortuosity along the x_i -direction, the boundary conditions at the sample boundaries at $x_i = 0$ and $x_i = L_i$, where L_i is the sample size along x_i , are given by $u = C$, a constant, and $u = 0$, respectively. For periodic structures, periodic boundary conditions are imposed on other boundaries. For experimentally obtained microstructures or a portion of simulated microstructures, the mean-field solution to Laplace's equation in the absence of microstructures is imposed as the boundary condition. Specifically, the concentration is set to $u = u_{MF}$, where $u_{MF} = C(1 - x_i/L_i)$. Since the actual boundary conditions are usually unknown in this case, the mean field solution, which reduces the effects of disconnected pore sub-domains caused by the limited sample size, is adopted. This boundary-condition approximation tends to overestimate the flux and thus underestimates the tortuosity. As with all boundary effects, the error resulting from this assumption can be reduced by utilizing larger specimens (containing many microstructural features) in the simulation.

We initially utilized Comsol (cf. www.comsol.com) with a finite-element mesh to measure the tortuosity. However, as the sample domain increased in size and the microstructure increased in complexity, Comsol became computationally too demanding. A parallel version of the software was not available at the time. We thus developed a finite-difference (FD) code to perform the tortuosity calculations with a

FD mesh. We performed a careful error analysis and found that, in the tortuosity calculations for minimal surfaces, the difference resulting from using the regular-shaped (FD) mesh is less than 1% with respect to Comsol’s results, while for the spinodal decomposed structure with very complex geometry the difference is less than 3%. The latter method is also considerably more efficient, and we have had no difficulty in calculating tortuosity for microstructures using this method with our available resources.

The effective transport properties in a two-phase composite are calculated in the manner similar to the tortuosity calculation. We assume that transport can be described by the steady-state diffusion equation, Eq. 2.5, in the computational domain. The equation is discretized and solved using the FD approach. The microstructural morphology information is used to set the transport coefficient $D(x)$ in the FD grid. The Dirichlet boundary conditions are imposed on both inflow and outflow boundaries, as described earlier (see also Ref. [3]), while either periodic or mean-field boundary conditions are imposed on other boundaries. The effective transport coefficient D^e of the composite is calculated from the solution of u by evaluating

$$D_i^e = \frac{\int_V D(x_i) \frac{\partial u}{\partial x_i} dV}{V \left(\frac{\partial u}{\partial x_i} \right)_0}. \quad (2.7)$$

Here, the concentration gradient $(\partial u / \partial x_i)_0$ is given by $\Delta u / L$, where L is the size of the domain along the flow direction, which is indicated by the subscript i .

The tortuosity factor is inversely proportional to the effective transport property in the case where one phase has negligible diffusivity; thus, it is a characteristic of the structure of the transporting phase. The advantage of considering the tortuosity factor is that it provides a means to characterize the effect of structures on the transport properties. The definition of the tortuosity factor we use here, as mentioned

earlier, is based on studies of diffusional transport in a porous medium [64].

2.4 Results

2.4.1 Model validation

As the first attempt to evaluate the tortuosity factor, we utilized Comsol with finite element meshes. Although finite-element based packages can provide high accuracy, importing complex structures into finite element meshes can be especially challenging. In order to circumvent the difficulty of meshing complex geometries in Comsol, we instead interpolated the diffusivities as functions of position (where the microstructure is used to determine which material occupies each position) and solved Eq. 2.5. The resulting u was then used to calculate the tortuosity using Eq. 2.6.

This procedure was examined with the scenarios of embedded non-transporting spheres in the non-transporting cubic matrix. We placed 1, 4, 8, and 27 non-transporting spheres into the transporting matrix, which corresponds to volume fractions of 11.3%, 13.4%, 26.8%, and 38.3% for the non-transporting phase. The convergence criteria was set to be 10^{-6} (the default relative tolerance in Comsol). We find that when the transport coefficient ratios v of the transporting to non-transporting phase are larger than 100, the error of this interpolation procedure compared to the solution based on a surface mesh is less than 0.7%. If the transport coefficient ratio is larger than 1000, the error is less than 0.3% (Fig. 2.5). Thus, we demonstrated that this procedure can achieve high accuracy when the convergence criteria and mesh quality are properly selected.

Although this interpolation procedure with Comsol provides high accuracy, Comsol was limited to running on a single CPU so that the domain size and mesh numbers were confined. In order to perform the tortuosity calculations for large three-dimensional samples, we developed a FD program as previously mentioned in section

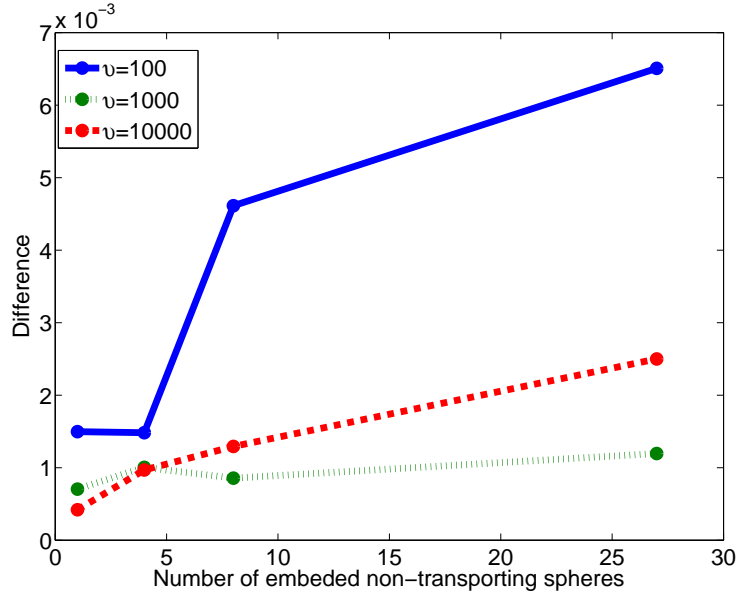


Figure 2.5: The difference of the effective flux calculated with the interpolation method and that calculated with a standard surface mesh.

2.3. To demonstrate the accuracy of our FD procedure, we investigated the tortuosity factors of four different minimal surfaces, P, D, G (Fig. 2.1, bottom left), and S (Fig. 2.1, bottom right), using the FD procedure, and compared the results with those acquired by the interpolation method using Comsol. The P, D, G, and S minimal-surface structures are generated using a Landau model similar to Ref. [53]. As shown in Table 2.2, the deviation of the tortuosity factors of the four examined structures between the two methods is within 1%. Note that the periodic boundary condition is applied in this minimal-surface test so that the potential errors that stem from the boundary conditions are excluded.

Method	P	D	S	G
Interpolation	1.51	1.44	1.49	1.43
FD	1.51	1.43	1.48	1.43

Table 2.2: A comparison of tortuosity factors calculated from our interpolation and FD procedures for different minimal surface structures .

To further validate our method, we utilized the FD procedures to calculate effective transport properties for the Schwarz P bicontinuous structure (Fig. 2.1, top

left). Both ill-ordered ($\lambda_1 = 1$ and $\sigma_1 = 0.1$ while $\lambda_2 = 0.1$ and $\sigma_2 = 1$, antisymmetric) and well-ordered ($\lambda_1 = 1$ and $\sigma_1 = 1$ while $\lambda_2 = 0.02$ and $\sigma_2 = 0.01$) scenarios are examined. Our results in the ill-ordered scenario are consistent with Ref. [32] to three significant digits ($\sigma_e = \lambda_e = 0.427$). While the well-ordered results can only be estimated from a published figure in [34], the difference between our results and theirs appears to be negligible.

2.4.2 Transport in SD composites and minimal-surface structures

As mentioned earlier, in the late stages of its evolution, a two-phase SD microstructure evolves in a self-similar manner, i.e., the structure remains statistically identical when the length is scaled with its time-dependent characteristic length scale. Therefore, the transport properties are expected to remain constant during this evolution regime. To examine the transport properties of the SD composite and its robustness, we evaluate the tortuosity factor of the SD composite at various times during the evolution.

In our examination of the tortuosity factor at seven different evolution times, the average tortuosity factor was found to be 1.577 with a standard deviation of 0.009. As shown in Fig. 2.6, the tortuosity factor of the SD composite thus remains fairly consistent throughout the evolution. Furthermore, the length scale of the structure can be varied to control other properties of the composite. In addition, this finding supports the self-similarity of the coarsening structure following spinodal decomposition, which was originally suggested based on the interfacial shape distribution of the genus.

Other minimal-surface two-phase structures with equal volume fractions also exist. These include complementary P (*i.e.*, C(P)), complementary S (*i.e.*, C(S)), and complementary Y (*i.e.*, C(Y)) surfaces, in addition to the aforementioned Schoen's G and Schwarz P and D, and S surfaces. Because of their morphological and topological

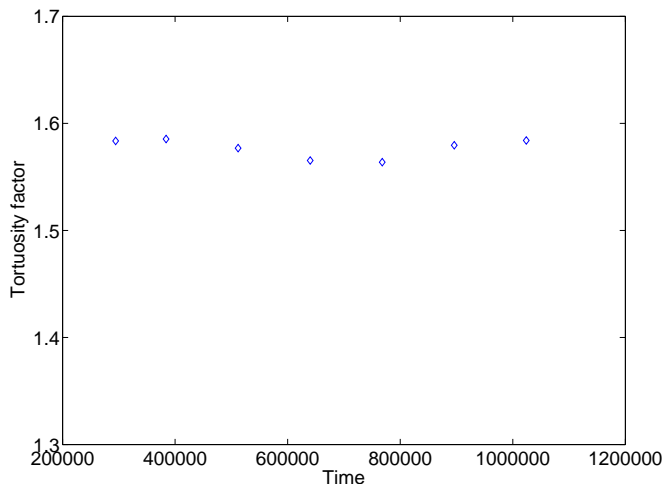


Figure 2.6: Tortuosity factor of the SD composite as a function of coarsening time.

similarities, we have further investigated the transport properties of minimal-surface bicontinuous structures that have equal volume fractions in terms of the tortuosity factor. The results are shown in Fig. 2.7, along with the result for the SD structure. All minimal-surface structures exhibit low tortuosity ($\lesssim 1.5$), with the G-surface structure having the smallest tortuosity. (Note that the trend is different from that in Ref. [58]. The authors of Ref. [58] examined fluid flow, which is affected greatly by the presence of a surface at which a no-slip boundary condition is imposed.) The tortuosity factor of the SD composite (averaged over the seven different times) is only 5% larger than that exhibited by the P surface structure and 10% larger than that of the G surface structure, which possesses the highest transport properties among the structures we examined. This comparison supports the possibility that SD composites could be utilized to achieve highly enhanced simultaneous transport. Therefore, the nearly optimized transport properties in this structure are robust, and the fabrication of these structures is expected to be easily controlled.

We then examined the effective transport coefficients of the self-similar structure of the two-phase SD composite. Interestingly, in the ill-ordered scenario described in Section 2.1, the sum of the two effective transport coefficients we obtained for the

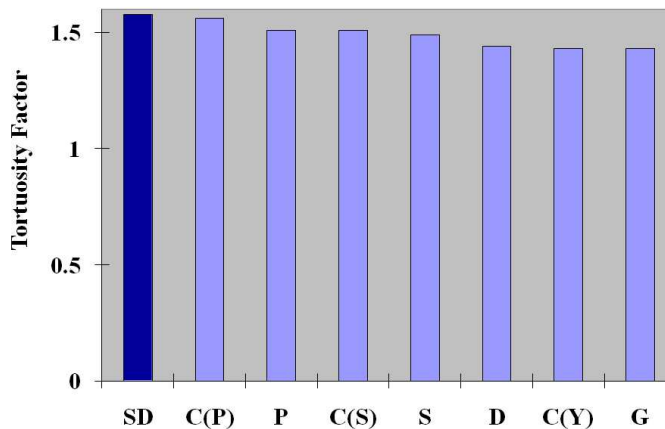


Figure 2.7: Tortuosity factors for the SD composite and minimal surfaces.

SD composite (0.84) is only slightly lower than the sum for the Schwarz P structure (0.85). The SD structure thus performs nearly as well as the Schwarz P bicontinuous structure with this set of transport coefficients. This finding suggests the possibility of self-assembly of two-phase composite materials with nearly optimized simultaneous transport properties through a natural phase separation mechanism.

Two interesting questions regarding minimal-surface structures arise: why can minimal-surface structures offer an optimized transport sum when competing transport is considered, and how does the SD composite achieve transport properties that are similar to those of minimal-surface bicontinuous structures? First, to achieve an optimized transport sum in a competing transport scenario, the binary composite must be bicontinuous. This criterion is satisfied by both minimal-surface structures and SD composites. Second, in this particular ill-ordered scenario discussed in Section 2.1, where the two competing transport coefficients are antisymmetric, the phase inversion symmetry is an important characteristic that facilitates simultaneous transport, because one phase transports most of one quantity and little of the other, whereas the other transports little of the first quantity and most of the other. The SD composite offers advantages that are similar to those of minimal-surface structures due to the morphological similarity between the two comprising phases. Moreover,

for a given topology and symmetry of the structure, any excess surface area implies a more tortuous transport path. Since any deviation of mean curvature increases surface area, the optimizing structure for given symmetry constraints has a minimal surface for an equal volume mixture. For an asymmetric mixture, the optimizing structure is instead a constant-mean-curvature structure, which is consistent with the calculations by Zhou and Li [65]. Therefore, the minimal-surface structures are those structures that optimize transport for a symmetric (50/50) mixture together with other constraints such as the rotational symmetry. Because the evolution of the SD structures is driven by capillarity, they tend to reduce their interfacial area to lower interfacial free energy. This again leads to a less tortuous transport path, though not as perfectly as the minimal-surface structure.

To illustrate the last point, we examine the interfacial curvatures present in the aforementioned structures with the interfacial shape distribution (ISD) diagram [66] (Fig. 2.8). A minimal-surface structure will simply lie on the $\kappa_1 = -\kappa_2$ line, where κ_1 and κ_2 are the principal curvatures, since it has zero mean curvature everywhere. The SD composite possesses zero *average* mean curvature and its interfacial curvatures are centered at the $\kappa_1 = -\kappa_2$ line. While the SD structure possesses interfaces with non-zero mean curvatures, the ISD is distributed around the $\kappa_1 = -\kappa_2$ line. Given that the evolution of the SD structure is driven by the difference in the mean curvature, a coupling of the interfacial mean curvature exists. This coupling effect results in a narrow distribution in the mean curvature for SD composites on the ISD. The morphology of an SD composite thus can be considered rather similar to that of the minimal-surface structures, which results in the highly enhanced transport properties of the SD composite.

In summary, we identified a two-phase structure that forms subsequent to spinodal decomposition as a candidate for a multifunctional composite that has enhanced competing transport properties. The performance was assessed for an equal-volume-

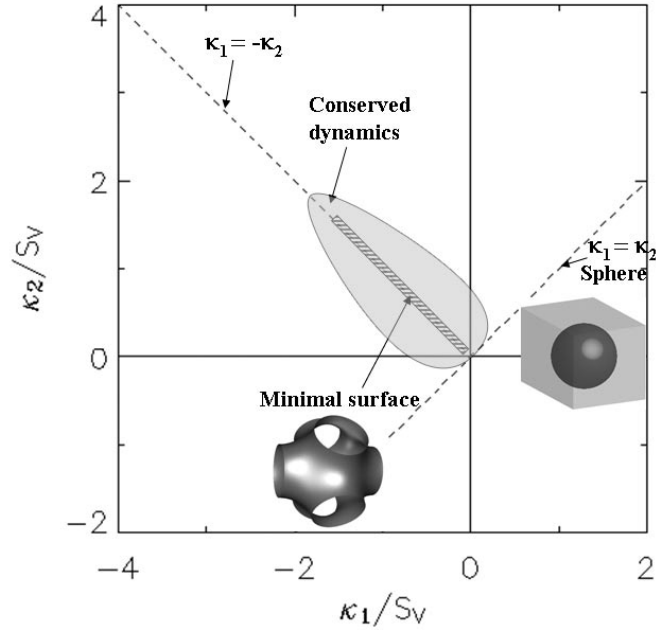


Figure 2.8: A schematic interfacial shape distribution diagram, which is scaled by the surface area per volume S_V and shows the distribution of interfacial principal curvatures [5].

fraction composite by examining the sum of the effective transport coefficients and the tortuosity factor. Unlike minimal-surface structures, which are known to optimize transport properties under sets of constraints, this structure forms naturally and evolves self-similarly, suggesting a practical means for fabrication in many classes of materials. The enhanced transport properties of such composites are explained by identifying analogous features between its structure and those of the minimal surfaces using the ISD diagram. In addition to bicontinuity, the interface having a nearly zero mean curvature is recognized as the key to enhanced transport properties [5].

These identified characteristics and structures, however, pertain to the case of two-phase composites for two competing transports. In order to find optimized structures of SOFC anodes, for instance, electrochemical reaction mechanisms should be included as a functionality in addition to the simultaneous transports.

2.4.3 Tortuosity of experimental composite samples

The methods described previously have a wide variety of applications due to the ubiquity of composite materials that enhance material properties. For example, porous materials are often used for structural materials in order to achieve excellent mechanical properties while reducing the material cost and weight. Therefore, our work involved collaborations with experimental groups that are interested in composite properties of porous alumina as well as SOFC cathodes, which are directly related to our focus topic of energy materials. The results are summarized below.

2.4.3.1 Porous alumina

Alumina, which can be fabricated by thermoreversible gelcasting, is one of the most widely studied composite materials due to its high electrical insulation, high mechanical strength, and high chemical resistance; it is thus used in commercialized products such as tubes, rods, and plates. Since the material properties of alumina are well understood, a porous alumina sample that is fabricated via thermoreversible gelcasting is studied here. The sample is produced using the following procedures: (1) PMMA-PnBA-PMMA triblock copolymers are dissolved in pentanol solvent; (2) alumina and polymer fillers are added; (3) the mixture is ultrasonicated; (4) the mixture is casted into a heated mold; (5) the sample is cooled and demolded; (6) the sample is dried; (7) the filler is burned out to form pores.

The microstructural data of our sample is acquired via computed tomography (CT) scan and subsequent image processing by Prof. Katherine Faber's group at Northwestern University (Fig. 2.9). The sample data is composed of 512 by 512 by 511 voxels, which corresponds to 742.2 μm by 742.2 μm by 742 μm . Since we investigate only the geometric effects on transport, the dimensions reported hereafter are all in the mesh size unit for convenience. The volume fraction of the initial fugitive filler is 35%, and the porosity after burn out is $\sim 23\%$.

As a first attempt to measure the tortuosity, the calculation was implemented by our interpolation procedure using Comsol. We set the transport coefficient ratios v of the transporting (pores) to non-transporting (alumina) phase to be 1000, which warrants accuracy in the calculations. The computer used to conduct the calculations has 8GB RAM. Although there is no size or mesh number limitation for 64-bit Comsol, to resolve this porous alumina microstructure, extra-fine meshes are needed and the computation was especially time-consuming. For example, to calculate the tortuosity factor for a domain of dimensions 181 by 181 by 181, the calculation time on our 8GB-RAM machine was approximately 110 hours.

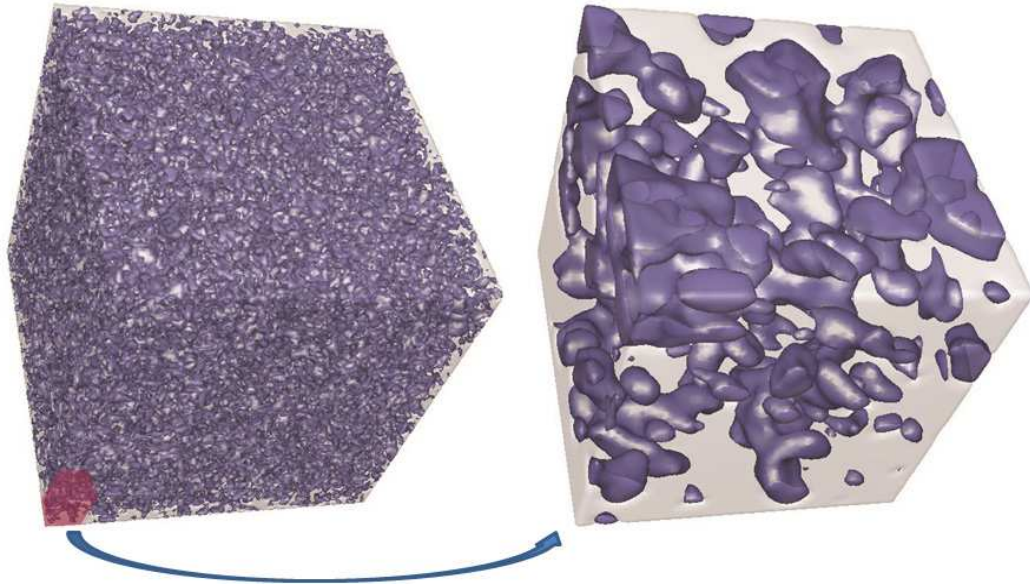


Figure 2.9: The microstructure of a porous alumina sample of dimensions $742.2\mu m$ by $742.2\mu m$ by $742\mu m$ (the entire sample, left), and a $(92.8\mu m)^3$ portion (right). The semi-transparent grey phase represents alumina and the blue phase illustrates pores. This alumina sample has only 23% porosity.

To proceed, we cropped the $[0:100, 0:100, 0:100]$ sub-domain from the original sample, whose volume fraction of the pore phase was 20.58%. The tortuosity factors that we acquired for this sub-domain, at three primary axis, are $(\kappa_x, \kappa_y, \kappa_z) = (4.34, 4.74, 5.40)$. In order to examine the size effect and anisotropy, we increased the sub-domain size to 151^3 ($[150:300, 150:300, 150:300]$) and 181^3 ($[150:330, 150:330,$

150:330]). For the 151^3 sub-domain, the tortuosity factors were found to be $(\kappa_x, \kappa_y, \kappa_z) = (6.12, 6.99, 7.25)$, with a porosity of 22.5%. For the 181^3 sub-domain, the tortuosity factors were $(\kappa_x, \kappa_y, \kappa_z) = (5.00, 5.56, 5.88)$, with a pore volume fraction of 23.2%. These results suggest that a certain degree of anisotropy exists in this sample and the size effect is not negligible for domain sizes under 181^3 .

To minimize the size effect, we developed an MPI-parallelized FORTRAN code based on the FD method to calculate the tortuosity factors for larger sub-domains. As shown in Table 2.3, the tortuosity factors consistently approach the values of the largest domain-size in each axial direction. In Fig. 2.10, we find that the slopes of the 101^3 to 181^3 samples and the 301^3 to 501^3 samples are very different. This slope difference suggests that the dependence of the tortuosity factor on the domain size is nonlinear. The still changing value of the tortuosity factor indicates that the size effect is not fully eliminated when using the 501^3 sample volume. This somewhat surprising result can be understood as the effects of the low volume fraction of the pores, or an artifact arising from boundary conditions. Although thermoreversible gelcasting preserves the connectivity of the pores, the $\sim 22\%$ volume fraction of the pore phase is much lower than the percolation threshold ($\sim 31\%$), and many pore clusters will not be percolated. If these non-percolated clusters are connected to the domain boundaries, the assumed mean-field BC can contribute to extra flux, which results in an underestimation of the tortuosity. This size effect can only be eliminated when the sample size is sufficiently large, that is, when the error introduced from the hypothesized mean-field BC is negligible.

Domain size	κ_x	κ_y	κ_z	κ_{ave}
301^3	7.31	8.85	6.65	7.60
401^3	8.69	10.19	7.14	8.67
501^3	8.97	11.52	7.81	9.43

Table 2.3: A comparison of the tortuosity factors calculated from our FD procedures for different domain sizes.

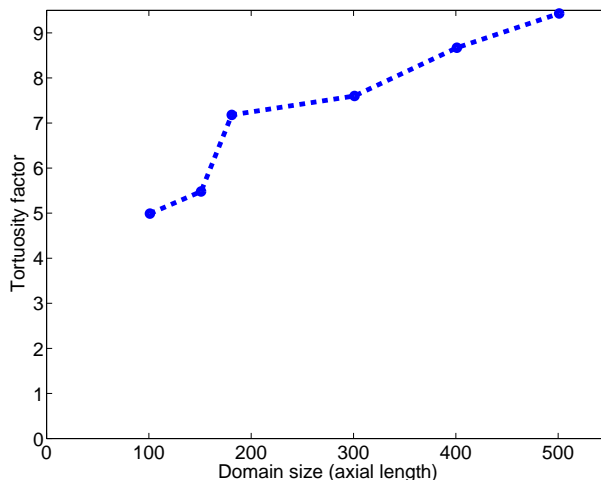


Figure 2.10: The tortuosity factor calculated using our finite-difference code versus the domain size.

2.4.3.2 LSM-YSZ cathodes

One state-of-the-art SOFC cathode material is a composite of $\text{La}_{1-x}\text{Sr}_x\text{MnO}_3$ (LSM) and 8 mol% Y_2O_3 -stabilized ZrO_2 (YSZ). Although many LSM-YSZ studies have used samples with 50 weight% YSZ, few researchers have reported maximum power density or minimal polarization resistance at weight ratios that deviate from 50LSM:50YSZ in such cathodes [67]. A detailed exploration of the LSM-YSZ compositional effects on electrochemical and structural parameters such as surface area densities, TPB densities, and phase connectivities can be found in Ref. [68]. Here, we focus on how LSM-YSZ volume ratios impact the transport properties of the YSZ and pore phases, each of which serves to transport oxygen ions and oxygen gas, respectively. Our samples were composed of the refined ink of mixtures of commercial LSM and YSZ powders, which were screen printed onto the YSZ electrolyte surface then fired at 1175°C for 1 hour [68].

Nine LSM-YSZ cathode samples were prepared with LSM:YSZ weight ratios ranging from 30:70 to 70:30 with an interval of 5%. The microstructural data of all nine samples are reconstructed via FIB-SEM imaging. Fig. 2.11 shows the 3D recon-

structured microstructures of the LSM-YSZ cathodes at two extreme weight ratios. The total volume analyzed for each sample is larger than $500 \mu\text{m}^3$ to provide statistically significant results.

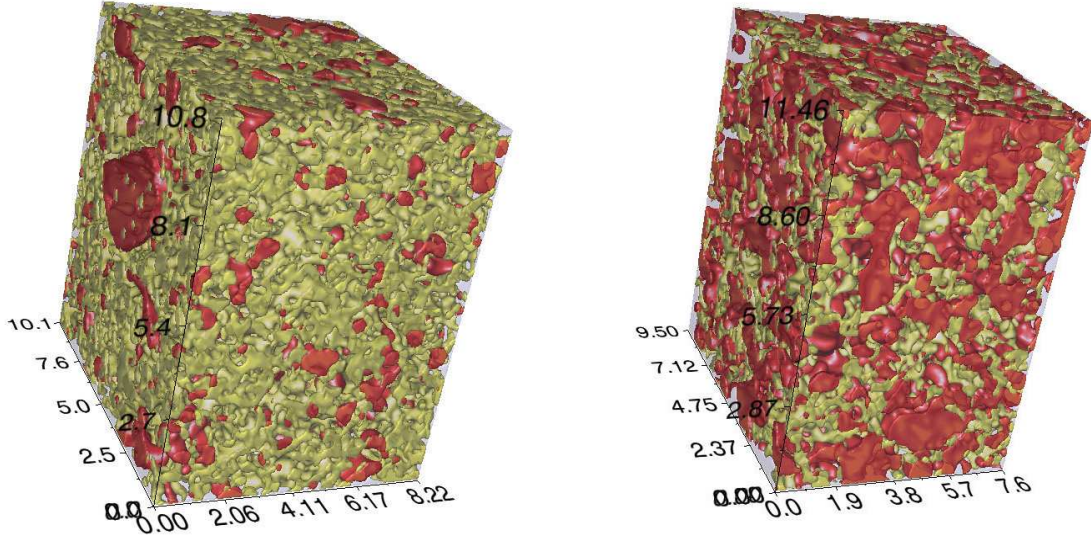


Figure 2.11: A view of the reconstructed LSM-YSZ cathodes. Yellow represents the YSZ phase, red the LSM phase, and grey shading the pore phase. The figure on the left has 70% YSZ and 30% LSM in weight, and the one on the right has 30% YSZ and 70% LSM.

The aforementioned FD method is utilized to calculate the tortuosity factors for all the cathode samples to study the geometric aspects of the transport properties. For all nine samples, the volume fraction of the pore phase remained at $\sim 50\%$ (between 49.8% and 53.1% as shown in Table 2.4), whereas the LSM-YSZ weight ratios were changed significantly. The tortuosity factors of the pore phase in these nine samples have an average of 1.604 with standard deviation of 0.042, which indicates that the compositional variation has no significant effect on the pore volume fraction and possibly on the pore microstructure. We find that the anisotropy in the pore phase is rather minor, which is probably an indication that the sample volume is large enough to be statistically representative.

In contrast, the volume fraction of the YSZ phase varies from 14% to 36% (ap-

Sample	3070	3565	4060	4555	5050	5545	6040	6535	7030
Pore vol.%	49.8%	51.1%	53.1%	50.4%	52.4%	50.2%	51.6%	49.9%	50.5%
κ_x	1.6	1.6	1.5	1.6	1.5	1.6	1.5	1.5	1.6
κ_y	1.7	1.7	1.6	1.7	1.6	1.6	1.5	1.5	1.6
κ_z	1.7	1.6	1.6	1.6	1.6	1.7	1.6	1.8	1.6
YSZ vol.%	36.5%	34.2%	30.5%	29.0%	24.6%	24.3%	19.0%	16.8%	14.1%
κ_x	2.3	2.6	3.0	3.2	3.4	3.5	5.0	5.2	7.0
κ_y	2.3	2.5	3.0	2.9	3.4	3.3	4.4	4.7	6.3
κ_z	2.4	2.6	3.2	2.9	3.5	4.0	5.2	6.7	6.2

Table 2.4: Tortuosity factors calculated for various compositions of LSM-YSZ cathodes. The sample is represented in terms of the LSM:YSZ weight ratios. That is, sample 3070 is denoted by 30LSM:70YSZ.

proximately 30% to 70% of the solid volume) due to the tailored LSM-YSZ weight ratios (Table 2.4). As shown in Fig. 2.12, the tortuosity factors vary with the volume fraction from 6.5 to 2.3. Interestingly, even at the lowest volume fraction of 14%, which is well below the theoretical percolation threshold of simple cubic geometry ($\sim 31\%$ [69]), the tortuosity factor of 6.5 indicates that the microstructure is still percolated sufficiently to support transport. Another noticeable feature is the slope change at a volume fraction of $\sim 26\%$. This slope change may result from a transition of the microstructure from one that is well-networked (nearly continuous) to one that is clustered (more disconnected bodies). In addition, we find that the variation of the tortuosity along different flow directions increases when the volume fraction of the YSZ phase is significantly lower than the volume fraction where the slope change occurs. This result is not surprising because the number of clusters spanning the sample volume decreases as the volume fraction is reduced. The clusters within low volume-fraction samples are unlikely to be triply percolated, which would lead to variations in tortuosity along various directions.

In summary, we have identified the critical volume fraction ($\sim 26\%$) at which YSZ transitions from a well-connected to a clustered phase. We have also found that the

anisotropy of the YSZ phase manifests when its volume fraction is below 19%. These simulation results provide effective transport properties of the material that help to determine the optimized LSM:YSZ weight ratio for the fabrication of the LSM-YSZ cathode.

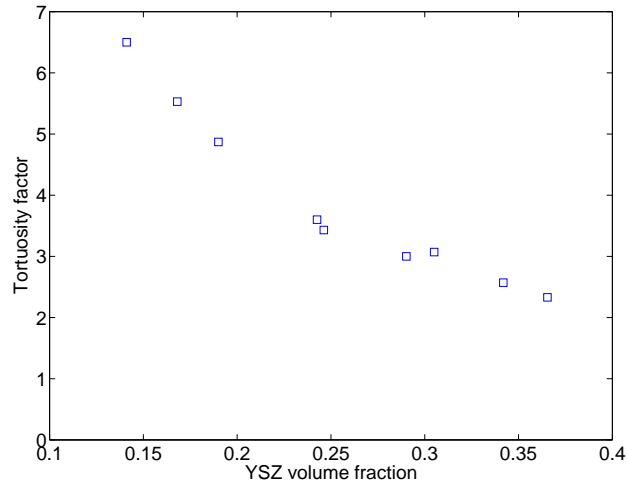


Figure 2.12: Tortuosity factors averaged over three axial directions at different YSZ volume fractions.

CHAPTER III

Quantitative Modeling of Nickel Coarsening in SOFC Cermet Anodes

3.1 Nickel coarsening in SOFC anodes

Solid oxide fuel cells (SOFCs) are one of the most promising clean energy conversion devices for stationary applications because of their low pollutant emissions, high efficiency, and ability to operate using various hydrocarbon fuels. The need for precious-metal catalysts is eliminated in SOFCs because the reaction kinetics is enhanced at their operating temperatures, which are between 500 and 1000°C [70]. However, high operating temperatures also lead to disadvantages such as slow startup, high fabrication costs, and rapid component degradation [71]. For SOFCs to be commercially viable for stationary applications, their lifetime must meet a minimum of $\sim 50,000$ hours. This goal has not yet been achieved. Understanding SOFC degradation mechanisms is therefore crucial to improving their durability.

The degradation mechanisms of SOFCs have been reviewed in a few recent articles [72, 73]. SOFC degradation is usually evaluated in terms of cell power or voltage decrease or area-specific resistance (ASR) increase, which is determined by the electrochemical impedance spectroscopy (EIS). These electrochemical methods are advantageous in that they allow the cell degradation to be monitored in situ. However,

even though a few studies [74, 75] have attempted to address SOFC degradation, it is very difficult to unambiguously characterize the impacts of individual mechanisms using these techniques. Many non-electrochemical methods have been used to identify and monitor the degradation and failure mechanisms of SOFCs in situ or pre-/post-operation (for a review, see Ref. [76] for a review), including X-ray tomography and X-ray diffraction. Among these degradation mechanisms, the microstructural change in a Ni-based cermet anode is one of the least understood, because experiments that can provide detailed time-dependent, 3D structural information are difficult.

The anode of SOFCs is usually made of a composite material of complex morphology that facilitates the transport of fuels, ions, and electrons. The most commonly used anode material is a porous cermet comprised of nickel (Ni) and yttria-stabilized zirconia (YSZ). Electrochemical reactions at the SOFC anode mainly occur in the vicinity of the three-phase boundaries (TPBs), where the pore, Ni, and YSZ phases are in contact [77]. Although the electrochemical reaction mechanisms are not very well understood, the length of the TPBs is considered one of the most important geometrical parameters that dictates the resistance in a SOFC anode [78]. The anode is thus designed to have a complex microstructure and increase the TPB lengths and the simultaneous transport of three different species. However, this intricate anode microstructure is typically not stable. The agglomeration and coarsening of nickel particles have been considered as the major mechanisms responsible for microstructural change in SOFC anodes [2]. Ni coarsening in the SOFC anode is a capillarity-driven phenomenon. Regions with high curvatures have higher chemical potentials than those with lower curvatures in accordance with the Gibbs-Thomson effect. Materials will therefore be transported from higher- to lower-curvature regions when mobility is sufficiently large for the time scale of interest. This leads to lower free energy of the system. This phenomenon increases the resistance in SOFCs and results in cell degradation.

Long-term coarsening experiments have been conducted for thousands of hours to study Ni coarsening in Ni-YSZ anodes. Simwonis et al. [2] measured a 33% decrease in electrical conductivity after 4000-hour exposure of a Ni-YSZ anode to a H₂ environment at 1000°C. They also found a 26% average Ni particle-size increase via analysis of micrographs of cross-sections. They attempted to describe the microstructure-conductivity relationship based on an empirical model proposed in Ref. [79] with microstructural parameters acquired; they claimed to capture the trend fairly well. Thyden et al. [80, 74] performed an aging experiment of a SOFC over 17,500 hours. The cell was operated at 850°C and an initial current density of 1 A/cm² was used. Optical microscopy, field emission-scanning electron microscopy (FE-SEM), SEM-charge contrast (SEM-CC), FIB-SEM, and EIS measurements were utilized to analyze the microstructural evolution in the Ni-YSZ anode. Their results suggested that an increase in the H₂O concentration can promote Ni particle coarsening and lead to conductivity loss within the Ni-YSZ cermet. Tanasini et al. [81] also conducted coarsening experiments for a single SOFC operated at 850°C with humidified H₂. Although cell degradation is often attributed to cathodic processes (e.g., Cr poisoning and cathode-electrolyte interface formation reaction), they reported that the major cell performance reduction stems from the anode degradation due to coarsening. They also found that the cell potential drop and Ni particle size increase reach a plateau after ~ 1000 hours of operation. Despite these experimental efforts, a quantitative correlation between microstructure and coarsening still awaits explication.

On the theoretical side, even though the performance of SOFCs can be largely affected by microstructural changes, only a few models have been proposed to study the effects of coarsening on the performance of electrodes [82, 83, 84]. Due to the inability of acquiring 3D microstructural information for Ni-YSZ anodes, these models were mostly based on empirically fitted parameters or oversimplified microstructures. The use of oversimplified microstructures and empirical parameters without extensive

validations can be problematic because it can lead to incorrect conclusions.

Recently, we have demonstrated that the microstructure of SOFC electrodes can be three-dimensionally reconstructed using dual-beam focused ion beam-scanning electron microscopy (FIB-SEM) [3]. The data can be acquired to produce a wealth of information, including the tortuosity of the individual phases as and the TPB density. While FIB-SEM allows the 3D reconstruction of anode microstructure, this technique damages the material. Thus, no evolution information can be obtained for the specimen after the procedure. However, modeling offers the advantage of allowing systematic analyses of coarsening effects on the performance of SOFC anodes. Although the phenomenon of anode coarsening can be described as a free-boundary problem in the sharp-interface modeling framework, explicit tracking of the evolving phase boundaries is highly impracticable in three dimensions. For a 3D anode with a complex microstructure, it is therefore advantageous to use a diffuse interface approach, such as a phase-field modeling. Therefore, we have developed a diffuse-interface model framework in conjunction with FIB-SEM experiments to quantitatively investigate Ni coarsening.

3.2 The phase-field model

The fundamental basis of the phase-field approach is to define field variables, or order parameters (OPs), that distinguish the phases in a multi-phase system. OPs have a constant value in each bulk phase, while interfaces are represented by finite regions in which the OPs smoothly vary from one bulk value to another. A phase-field model can thus be considered as a type of diffuse interface model, which describes interfaces using a finite thickness. As a result, explicit tracking of the moving boundaries is no longer necessary since the boundary information is embedded in the OPs in the phase-field approach. Implicit tracking of interfaces is a computational advantage of the phase-field approach in modeling multi-phase systems with multiple

interfaces, especially in three dimensions.

The inclusion of OPs into the free energy density is generally attributed to Landau and Ginzburg for their work related to the modeling of superconductivity in the 1950s [85]. Later, in order to describe the interfacial energy of an inhomogeneous system, Cahn and Hilliard [86] proposed to describe the free energy of a system by its OPs and their spatial derivatives. The concept of describing the evolution of an interface between two phases differing in composition with a Ginzburg-Landau-type functional was introduced by Langer [87]. Allen and Cahn [88] developed the theory for the motion of a coherent anti-phase boundary. Formal asymptotic analyses have been used to show that a variety of phase-field models (PFMs) recover the corresponding sharp interface models when the width of the interfaces approaches zero [89, 90].

PFMs have been successfully utilized to describe phase transition in two-phase systems (see, e.g., [89]), dendrite growth (see, e.g., [91]), and Ostwald ripening (see, e.g., [92]). However, in three-phase systems, a PFM with a generic free energy functional may introduce an artificial third-phase contribution at a two-phase boundary, if no special treatment is applied [93, 94]. This effect can compromise the study of cermet anode coarsening since the emergence of a phantom phase at a two-phase boundary can contribute to extra TPBs. This foreign-phase creation will lead to an erroneous estimation of the electrochemically active sites and the evolution kinetics. Nestler *et al.* [93] proposed two types of remedies for this problem in a multi-component liquid-solid system. In each of these approaches, the potentials penalize equal contributions from each of the OPs to reduce the third phase appearance. However, the modified potentials may not eliminate the PFM simulation artifact for a simple three-phase conserved-field system undergoing coarsening. To address this issue, Folch *et al.* [94] developed a specific minimal model for a three-phase system that ensures that there is no third phase invasion at a two-phase boundary. This

model can also accommodate systems with unequal surface tensions by adding tunable saddle-lifting terms. However, the computations become too expensive due to the steeper free-energy landscape needed for large-scale simulations.

The PFM handles the interface implicitly because the interface information is embedded in OPs. Immiscibility and interfacial energy are naturally incorporated in the PFM via the bulk free energy and the gradient energy penalty over the diffuse-interfacial region. The interfacial energy ratios among different interfaces can be specified in the PFM using proper parameterization of the free energy functional. Therefore, we developed a first phase-field model, named Model A, within the context of a multiphase PFM, to model the Ni coarsening in three-phase anodes [95]. As discussed later, Model A allows a small mobility of YSZ, which significantly affects the evolution. Therefore, we developed an alternative model based on the smoothed boundary method (SBM), which is described in the following section.

3.3 The smoothed boundary method

Complex geometries are abundant in naturally and artificially formed objects. To study physical processes or phenomena occurring within such objects, the numerical solution of partial differential equations (PDEs) with prescribed boundary conditions is necessary. A standard scheme requires triangulation of the complex shapes, followed by solving of the PDEs using the finite element method (FEM). However, automatic generation of proper meshes for complex 3D domains is challenging. In addition, in many cases the complex geometries can evolve during a physical process, thus demanding a dynamic remeshing of the evolved domain.

To address these difficulties, one can alternatively embed complex geometries within a larger, simpler domain (such as a cube). The PDEs can then be solved with regularly shaped meshes on the extended domain, provided that the original boundary conditions can be properly applied. Methods employing such a concept in-

clude composite FEM [96], extended FEM [97], the immersed interface method [98], the immersed boundary method [99], and the cut-cell method [100].

The smoothed boundary method differs from the above mentioned methods in that it represents the complex geometries with a phase-field-like function, which varies smoothly across the domain boundary. Thus, the sharp boundaries of the complex geometry $\partial\Omega$ are instead described by a thin interface of finite width. This diffuse-domain approach was utilized to study the diffusion of chemoattractant inside a cell with a no-flux boundary condition (BC) at the cell surface [101]. Spectral methods were later coupled with the SBM to model electrical wave propagation in cardiac tissues with a no-flux BC [102, 103]. In Ref. [104], the SBM was extended to solve PDEs in complex geometries with Dirichlet, Neumann, and Robin BCs. The SBM reformulated PDEs were shown to converge to their sharp-interface formulation using an asymptotic analysis [104]. An alternative but similar approach was independently developed, [105].

In the SBM, an auxiliary variable, a domain parameter ψ , is introduced to identify the domain of interest Ω in which the PDEs are solved. The domain parameter ψ usually has a value of 1 within Ω , 0 exterior to Ω , and $0 < \psi < 1$ in $\partial\Omega$. Since the complex geometry is embedded in a regularly shaped, expanded domain, the exterior of the domain of interest is included only to facilitate computation; any numerical solutions obtained in the external region are devoid of meaningful information. The initial construction of the domain parameter ψ can be achieved by solving a phase-field equation or by transforming the distance function of the domain structure with the hyperbolic tangent.

The framework of the SBM is general and can be applied to different types of PDEs. For an easier understanding, we describe the SBM approach for Poisson's

equation on a stationary domain:

$$\nabla^2\Theta = f \quad \text{in} \quad \Omega, \quad (3.1)$$

where domain $\Omega \subset \Omega_{ext}$. The regularly shaped domain Ω_{ext} is arbitrarily chosen to facilitate the implementation of the SBM. In the case of Neumann boundary conditions,

$$\nabla\Theta \cdot \vec{n} = g \quad \text{on} \quad \partial\Omega, \quad (3.2)$$

where \vec{n} represents the outward unit normal vector to $\partial\Omega$, the SBM is derived by multiplying Eq. 3.1 by the domain parameter ψ . By using the product rule of differentiation, the SBM-reformulated Poisson equation becomes

$$\nabla \cdot (\psi\nabla\Theta) - \nabla\psi \cdot \nabla\Theta = \psi f. \quad (3.3)$$

Because the unit normal vector of the diffuse interface in the phase-field framework is given by $\vec{n} = \nabla\psi/|\nabla\psi|$, the boundary condition, Eq. 3.2, can be rearranged as $\nabla\Theta \cdot \nabla\psi = g|\nabla\psi|$. Substituting the rearranged BCs into Eq. 3.3, the new governing equation is obtained as

$$\nabla \cdot (\psi\nabla\Theta) - g|\nabla\psi| = \psi f. \quad (3.4)$$

Eq. 3.4 incorporates both Poisson's equation and the Neumann boundary conditions and is solved on any domain Ω_{ext} that contains Ω .

In the case of Dirichlet boundary conditions,

$$\Theta = g \quad \text{on} \quad \partial\Omega, \quad (3.5)$$

Poisson's equation is multiplied by the square of the domain parameter ψ to derive the SBM formulation. By using the product rule of differentiation twice, Eq. 3.1 can

be transformed to

$$\psi^2 \nabla^2 \Theta = \psi^2 f = \psi \nabla \cdot (\psi \nabla \Theta) - \nabla \psi \cdot \nabla (\psi \Theta) + \Theta |\nabla \psi|^2. \quad (3.6)$$

The third term on the right-hand side can be identified as the boundary term because it gives non-zero values only at the boundaries of Ω . Therefore, the equation corresponding to Dirichlet boundary conditions $\Theta = g$ is simply substituted into that term. The reformulated governing equation is thus given by

$$\psi \nabla \cdot (\psi \nabla \Theta) - \nabla \psi \cdot \nabla (\psi \Theta) + g |\nabla \psi|^2 = \psi^2 f \quad \text{in } \Omega_{ext}. \quad (3.7)$$

It is generally believed that the YSZ phase has a very low mobility in an operating SOFC anode; that is, YSZ serves as the supporting structure in which Ni coarsens. We therefore propose a model, named Model B, utilizing the SBM for Ni coarsening simulations. In Model B, we assume that YSZ is stationary. It is therefore treated as the geometry within which the Ni and pore phases evolve. We also assume that the triple junctions in the Ni-YSZ anode possess the contact angles deduced from Young's equation for a locally flat surface. The dynamics of this system can thus be modeled by a single OP Cahn-Hilliard equation with two complementary BCs implemented with the SBM: the contact-angle BC at triple junctions and no-flux BC at YSZ interfaces.

3.4 Descriptions of the models and methods

We have proposed two PFMs for coarsening simulations in three-phase SOFC cermet anodes. Our models are based on a free energy functional that is computationally inexpensive and can circumvent the phantom-phase generation issue associated with some other models. To simplify our models, a few approximations have been made.

First, we consider that the volume of each phase in the Ni-YSZ anode is conserved (which is equivalent to mass conservation because the material is incompressible). (Note at ordinary operating temperatures of a SOFC (500 – 1000°C), the evaporation of Ni is negligible [106].) Therefore, we use the Cahn-Hilliard (conserved) equation as the governing equation. Second, the kinetic and thermodynamic properties are estimated at 1000 and 1100°C at which complementary experiments were conducted. In addition, the Ni surface tension is assumed to be independent of crystal orientation because its anisotropy is insignificant at such temperatures [107]. For the surface diffusivity of Ni, we utilize the value measured by the mass transfer method, which can provide the mean value of multiple crystal facets [107] or the value of certain facets of a single crystal [108].

We further simplify our models by identifying the dominant transport mechanism that dictates Ni coarsening in a Ni-YSZ anode. Three mechanisms play a role in the evolution of the Ni microstructure: evaporation-condensation, bulk diffusion, and surface diffusion. The evaporation-condensation mechanism is negligible here due to very low Ni vapor pressures [106]. Assuming that atoms on the interface have similar values of chemical driving force for both surface and bulk diffusion (a quasi-surface-volume equilibrium assumption), the ratio between surface diffusion and bulk diffusion contributing to the transport can be assessed by $\sigma = D_s \delta_s / D_B w$, where D_s and D_B are the surface and bulk diffusivities, respectively. Surface diffusion is considered to occur within the first several lattice layers on the surface within a thickness of $\delta_s \sim 1$ nm. The characteristic length w of Ni particles, as determined from anode microstructural data is between 0.1 μm to 1 μm . According to the literature, at 1000°C, the value for Ni surface diffusivity is on the order of $10^{-10} \text{ m}^2\text{s}^{-1}$ [107, 108], while bulk diffusivity is on the order of $10^{-16} \text{ m}^2\text{s}^{-1}$ [109]. Therefore, the surface to bulk diffusion ratio is $\sigma \approx 10^3$ in this system, which suggests that surface diffusion dominates.

The Cahn-Hilliard evolution equations can be regarded as a type of diffusion equation, where material transport is driven by the chemical potential. This potential is obtained as the variational derivative of the free energy, which is formulated to account for various driving forces of material transport. At ordinary operating temperatures, the three phases that comprise the Ni-YSZ anode can be considered as immiscible. Furthermore, we neglect any contributions of elastic stress to diffusion and external forces. We thus formulate our free energy functional as a simple Ginzburg-Landau functional $F = \int_V f dV$, where the free-energy density f contains both bulk and interfacial contributions and depends on the OPs and their derivatives.

The two PFMs we propose differ in the treatment of the YSZ phase. If we consider that the YSZ phase transports with a small mobility, then the Ni-YSZ anode is a system of three mobile phases (Ni, YSZ, and pores). This system requires two evolution equations to resolve the kinetics. We call this model *Model A*. In *Model B*, we consider the YSZ phase as completely immobile, which can be justified by the fact that its mobility is orders of magnitude smaller than that of the Ni phase. Therefore, only two phases, Ni and pores, are allowed to evolve in between of the YSZ matrix. To incorporate the YSZ phase as the internal boundary in the computational domain, we developed a model utilizing the SBM.

In the following sections, we present the framework of our two models, which quantitatively simulate Ni coarsening. Our models are free from empirical fitting parameters when input kinetic and thermodynamic coefficients are known. We also describe in greater detail how the simulation results of both models are linked to the physical phenomenon using an asymptotic analysis, and how the models are numerically implemented.

3.4.1 Model A

In Model A, the OPs are vectorized as $\vec{\phi} = (\phi_1, \phi_2, \phi_3)$ for generalization. Each vector component represents the volume fraction of the corresponding phase so that an additional constraint $\phi_1 + \phi_2 + \phi_3 = 1$ applies; thus, only two evolution equations are needed. The governing equation sets can be written as

$$\begin{aligned}\frac{\partial\phi_1}{\partial t} &= \nabla \cdot M(\vec{\phi}) \nabla \frac{\delta F}{\delta\phi_1}, \\ \frac{\partial\phi_2}{\partial t} &= \nabla \cdot M(\vec{\phi}) \nabla \frac{\delta F}{\delta\phi_2},\end{aligned}\tag{3.8}$$

where $M(\vec{\phi})$ is the surface mobility.

A standard bulk free energy for a three-phase system should contain three local minima, each of which represents a bulk-phase value. We select the three local minima as $\Phi_a = (1, 0, 0)$, $\Phi_b = (0, 1, 0)$, $\Phi_c = (0, 0, 1)$. However, in the three-phase Cahn-Hilliard dynamics, a foreign phase can be introduced at a two-phase interface. Two remedies are that one can use the procedure developed in [94] to generate a specific free energy, or one can use an interpolation function similar to that described in [110] (the latter method may only reduce the amount of the third phase contribution). Since the three phases in the Ni-YSZ anodes are immiscible, the generation of a foreign phase at a two-phase boundary is a problematic artifact that leads to extra TPB sites that do not physically exist.

Our approach to resolve this issue is to select a free energy functional that can limit a foreign-phase appearance and can also incorporate an unequal surface tension at a reasonable computational expense. In the Cahn-Hilliard dynamics, the excess free energy at the interfaces, i.e., the interfacial energy, is determined by gradient energy coefficients and the bulk free energy at intermediate values of OPs. According to Young's relation, the contact angles among the different phases are determined

by the interfacial energies of the intersecting interfaces. For instance, if phases 1, 2, and 3 are in contact at a triple junction, the contact angle formed in phase 1 is related to the interfacial energy of the interface 2-3 relative to that of the interfaces 1-3 and 1-2. It is, however, easier to understand the interfacial energy as a factor reflecting the affinity of one phase to another. A lower interfacial energy suggests a stronger bonding of the two phases that are in contact. This tendency appears to have profound effects on the long-term microstructural evolution as demonstrated in our simulations [95].

Applying the commonly used gradient and bulk free energy densities for multiple-OP systems, our free energy functional can be written as

$$F = \int_V dV \left(\sum_{i=1}^3 k_i \phi_i^2 (1 - \phi_i)^2 - \sum_{i,j=1, i>j}^3 \alpha_{ij}^2 \nabla \phi_i \nabla \phi_j \right). \quad (3.9)$$

The specific interfacial energy is calculated from the equilibrium solution at a planar interface. To do so, the free energy functional must be minimized subject to a constraint that the sum of the order parameters equals unity. This is carried out by taking the variational derivative of the functional using the method of Lagrange multipliers. The resulting equation is given by

$$\left(\frac{\delta F}{\delta \phi_i} \right)_{\phi_1 + \phi_2 + \phi_3 = 1} = \frac{\delta F}{\delta \phi_i} - \left(\frac{1}{3} \right) \sum_j \frac{\delta F}{\delta \phi_j}, \quad (3.10)$$

, where the variational derivatives at the right hand side of the equation are taken as if all ϕ_i 's were independent [94]. If we consider an interface between phase i and phase j without the existence of the third phase, the interfacial free energy can be calculated from the integration of the free energy density over the interface as

$$\gamma_{ij} = 2\alpha_{ij} \sqrt{(k_i + k_j)} \int_0^1 \phi_i (1 - \phi_i) d\phi_i = \frac{\alpha_{ij}}{3} \sqrt{(k_i + k_j)}. \quad (3.11)$$

Similarly, the interfacial width δ_{ij} can also be found as

$$\delta_{ij} = \frac{\alpha_{ij}}{\sqrt{(k_i + k_j)}}. \quad (3.12)$$

After multiplying Eq. 3.11 by Eq. 3.12 and rearranging the result, we find

$$3\delta_{ij}\gamma_{ij} = \alpha_{ij}^2. \quad (3.13)$$

By choosing $\delta_{12} = \delta_{23} = \delta_{13}$, the relationships between the gradient energy coefficients and the interfacial energy in this three-phase system is simplified as

$$\frac{\gamma_{12}}{\alpha_{12}^2} = \frac{\gamma_{23}}{\alpha_{23}^2} = \frac{\gamma_{13}}{\alpha_{13}^2}. \quad (3.14)$$

The values of the surface free energies can be set to those found in the literature or be left as a parameter if data are missing or uncertain. The interfacial width is a computational parameter that must be chosen to ensure thin-interface limit for accuracy while providing a numerically well-resolved interface. Once the interfacial width δ_{ij} and interfacial energies γ_{ij} are set, the gradient energy coefficients α_{ij} can be calculated from Eq. 3.13, and the bulk energy coefficients k_i can be calculated from Eq. 3.12.

Surface diffusion is generally considered to be the main mechanism of transport for the capillarity-driven microstructural evolution in these SOFC anodes [84]. We have confirmed the validity of this assumption based on an analysis of order of magnitudes. Since the OPs with integer values represent the bulk phases in the PFMs, the surface mobility function in a one-OP, two-phase case is commonly formulated as $M(\phi) = \phi^2(1-\phi)^2$; such a formulation guarantees a non-zero mobility at two-phase boundaries only.

In Model A, the surface mobility function is given by:

$$M(\phi_1, \phi_2, \phi_3) = \sum_{i,j=1,i>j}^3 M_{ij} \prod_{C_l C_h}(\phi_i) \prod_{C_l C_h}(\phi_j) (\phi_i \phi_j (1 - \phi_i)(1 - \phi_j)), \quad (3.15)$$

, where we introduce a boxcar function $\prod_{C_l C_h}(\phi_i)$ to avoid excess mobility resulting from the appearance of a small amount (less than 3% in fraction) of a foreign phase at a two-phase boundary. We choose $C_l = 0.05$ as the lower cutoff OP value in the mobility function, and $C_h = 1 - C_l$ as the upper cutoff value and resulting from the complementary value of the lower cutoff. All three mobility prefactors have positive values, and thus, materials flow from high to low chemical potentials.

3.4.2 Model B

In this model, we assume that YSZ is stationary and that the Ni phase evolves by diffusion along the Ni-pore interfaces. The dynamics of this system can thus be described by a single-OP Cahn-Hilliard equation with one contact-angle BC at triple junctions, and one no-flux BC at YSZ interfaces, where the OP distinguishes the Ni and pore phases.

The treatment of a contact-angle BC in a non-conserved (Allen-Cahn) PFM was proposed by Warren *et al.* [111] to model heterogeneous nucleation. Following [111], we developed Model B using the SBM for a Ni-YSZ anode coarsening with conserved dynamics. This SBM approach is an entirely diffuse-interface treatment that implicitly handles complex geometries (while Warren *et al.* applied delta function [111]). In the following derivation, we demonstrate that both no-flux and contact-angle BCs can be coupled with a Cahn-Hilliard equation to give a single evolution equation using the SBM framework.

For one-OP Cahn-Hilliard dynamics within a SBM framework, the evolution equa-

tion can be written as

$$\frac{\partial\phi}{\partial t} = \nabla \cdot M(\phi, \psi)\nabla\mu. \quad (3.16)$$

We consider the free energy functional as being:

$$\mathcal{F} = \int_V dV \left[\frac{\epsilon^2}{2} |\nabla\phi|^2 + f(\phi) \right], \quad (3.17)$$

where $f(\phi)$ is a generic double-well function. The chemical potential μ is by definition the variational derivative of free energy \mathcal{F} with respect to the order parameter ϕ , *i.e.*, $\mu = \delta\mathcal{F}/\delta\phi = \partial f/\partial\phi - \epsilon^2\nabla^2\phi$. We introduce in the SBM a domain parameter ψ to incorporate general BCs on internal boundaries. In this case, the domain parameter ψ distinguishes regions having YSZ ($\psi = 0$) and other phases ($\psi = 1$), as well as the YSZ interfaces ($0 < \psi < 1$).

Multiplying Eq. (3.16) by ψ and letting $\vec{J} = M\nabla\mu$ the formulation becomes

$$\frac{\partial(\psi\phi)}{\partial t} = \psi\nabla \cdot \vec{J} = \nabla \cdot (\psi\vec{J}) - \vec{J} \cdot \nabla\psi. \quad (3.18)$$

The aforementioned no-flux BC, $\nabla\mu \cdot \nabla\psi = 0$, should be applied to the internal boundaries (YSZ interfaces) to ensure mass conservation. This no-flux BC eliminates the last term of Eq. (3.18) and the equation becomes

$$\frac{\partial(\psi\phi)}{\partial t} = \nabla \cdot (\psi\vec{J}) = \nabla \cdot (\psi M\nabla\mu). \quad (3.19)$$

Like an ordinary OP in a phase-field approach, ψ varies continuously across the interface; thus, the unit interface normal \vec{n} of the YSZ interface can be described as a function of the gradient of ψ , *i.e.*, $\vec{n} = \nabla\psi/|\nabla\psi|$. By assuming that the effects of the YSZ on the Ni phase are only of short range (immiscible) and $\phi = 1$ represents

the bulk Ni phase, the contact angle θ at triple junctions can be formulated as

$$\vec{n} \cdot \frac{\nabla\phi}{|\nabla\phi|} = \frac{\nabla\psi}{|\nabla\psi|} \cdot \frac{\nabla\phi}{|\nabla\phi|} = -\cos\theta. \quad (3.20)$$

The negative sign comes from the convention that $\nabla\psi$ points into YSZ and $\nabla\phi$ points out of Ni.

The mechanical equilibrium at the triple junction corresponds to an extremum of the free energy, i.e., $\delta\mathcal{F} = 0$. We can use the planar solution of the thermodynamic equilibrium condition within the interface to find a useful equality, $|\nabla\phi| = \sqrt{2f}/\epsilon$, which can be substituted into Eq. (3.20) to derive the SBM contact-angle BC as

$$\nabla\psi \cdot \nabla\phi = -|\nabla\psi| \cos\theta \frac{\sqrt{2f}}{\epsilon}. \quad (3.21)$$

This contact-angle BC results in energy only near triple junctions, rather than in the bulk volume, to achieve the force balance at the triple junction that is dictated by Young's equation for a flat surface. The final evolution equation derived from the SBM with no-flux and contact-angle BCs is:

$$\frac{\partial(\psi\phi)}{\partial t} = \nabla \cdot \left\{ \psi M \nabla \left[f_\phi - \frac{\epsilon^2}{\psi} \left(\nabla \cdot (\psi \nabla \phi) + \frac{|\nabla\psi| \sqrt{2f}}{\epsilon} \cos\theta \right) \right] \right\}. \quad (3.22)$$

Again, the gradient energy coefficient ϵ , the contact angle θ , and the bulk energy coefficients in $f(\phi)$ are determined according to the interfacial energies of the Ni-YSZ cermet and the selected interfacial widths.

The mobility function in Model B is formulated as

$$M(\phi, \psi) = M_{Ni-Pore} \prod_{C_l C_h} (\phi) (\phi^2 (1 - \phi^2)) g(\psi), \quad (3.23)$$

, where $g(\psi) = \psi^6(10\psi^2 - 15\psi + 6)$ is introduced to control the mobility at and near triple junctions. This one-sided interpolation function $g(\psi)$ transitions smoothly from 1 to the order of 0.01 as the domain parameter varies from 1 to 0.5. In other words, this choice of the mobility function ensures an immobile YSZ phase by limiting the mobilities at YSZ interfaces. Subsequently, the mobility near a triple junction decreases from the Ni-pore value to a value that is 10^{-6} smaller as ψ varies from 1 to about 0.1.

3.4.3 Nondimensionalization and asymptotic analysis

Having the appropriate values of the mobility prefactors is essential in simulating coarsening kinetics. In order to quantitatively correlate simulation results with physical phenomena, asymptotic analyses are required in PFMs because of their diffuse interface nature. Using an asymptotic analysis, we determined the relationship between diffusivity and mobility and the characteristic simulation time scale. Unlike some of the previous studies, which determined model parameters by fitting coarsening experimental results, our model is a predictive model that is free of fitting parameters when the material properties, such as surface diffusivities, are accurately known.

In the Ni-YSZ anode of SOFCs, coarsening proceeds mostly via surface diffusion. The anisotropic effect of crystal facets on surface diffusion is lumped into one ensemble diffusivity in our models. In this case, the normal velocity V_n of the interface Γ incurred by surface diffusion, in the dimensional sharp-interface form, can be represented as

$$V_n = \frac{\gamma_s D_s \delta_s}{k_B T N_v} \nabla_s^2 \kappa_c = \frac{\gamma_s D_s \delta_s}{k_B T N_v} \frac{\partial^2 \kappa_c}{\partial s^2}, \quad (3.24)$$

, where γ_s is the surface energy, D_s is the surface diffusion coefficient, δ_s is the interfacial thickness, N_v is the atomic number density per volume, κ_c is the local curvature, ∇_s^2 is the surface Laplacian and $\partial/\partial s$ is the gradient operator along the

interface [112].

To link the corresponding diffuse-interface model to the aforementioned sharp-interface model, a pure two-phase boundary in this three-phase system is considered. For both Model A and Model B, the dimensional Cahn-Hilliard evolution equation at a two-phase boundary can be re-arranged as

$$\frac{\partial \phi}{\partial t} = \nabla \cdot (M(\phi) \nabla \mu), \quad (3.25)$$

$$\mu = \frac{\partial f(\phi)}{\partial \phi} - \epsilon^2 \nabla^2 \phi, \quad (3.26)$$

, where ϕ is the OP distinguishing two phases, $f(\phi) = W\phi^2(1 - \phi)^2/4$ is the energy density, and $M(\phi) = 6M_s\phi^2(1 - \phi)^2$ is the surface mobility. Eq. 3.25 and Eq. 3.26 possess the physical steady-state solution for a planar interface, i.e., $\phi(x) = [1 - \tanh(x/2\delta)]/2$, with the interface thickness $\delta = \epsilon\sqrt{(2/W)}$, and the interfacial energy $\gamma = \epsilon\sqrt{(W/72)}$.

Following the derivation in [113], a new set of variables for a non-dimensionalization of the governing equations is utilized. We assume that $\tau = L^4/D$, wherein L is the characteristic length scale of the sample and τ is the characteristic time scale for surface diffusion, and consider that other nondimensional quantities (denoted by overbars) are defined by

$$\begin{aligned} \bar{M}_s &= \frac{36M_s\gamma\delta}{D}, \quad \bar{\delta} = \frac{\delta}{L}, \quad \bar{x} = \frac{x}{L}, \quad \bar{t} = \frac{t}{\tau} \\ \bar{M}(\phi) &= \phi^2(1 - \phi)^2, \quad \bar{f}(\phi) = \frac{1}{2}\phi^2(1 - \phi)^2. \end{aligned} \quad (3.27)$$

Eqs. 3.25 and 3.26 can be written using the non-dimensional parameters to derive the non-dimensional evolution equation as

$$\frac{\partial \phi}{\partial \bar{t}} = \frac{1}{\bar{\delta}^2} \nabla \bar{M}(\phi) \nabla \bar{\mu} \quad (3.28)$$

$$\bar{\mu} = \frac{\partial \bar{f}(\phi)}{\partial \phi} - \bar{\delta}^2 \nabla^2 \phi, \quad (3.29)$$

The asymptotic analysis that was used is similar to that described in [114]. Briefly, we first determine the outer solution. Substituting equation 3.29 into 3.28, dropping the overbars, and replacing the variables δ with ζ , μ with $\mu_{out}(\vec{r}, t, \zeta)$, and ϕ with $\phi_{out}(\vec{r}, t, \zeta)$, we obtain the non-dimensional evolution equations

$$\zeta^2 \frac{\partial \phi_{out}}{\partial t} = \nabla \cdot \left[M(\phi_{out}) \nabla \left(\frac{\partial f}{\partial \phi_{out}} - \zeta^2 \nabla^2 \phi_{out} \right) \right] \quad (3.30)$$

$$\mu_{out} = \frac{\partial f}{\partial \phi_{out}} - \zeta^2 \nabla^2 \phi_{out} \quad (3.31)$$

An outer expansion is performed by expanding the field ϕ_{out} and μ_{out} in our model in powers of ζ as follows:

$$\phi_{out}(\vec{r}, t, \zeta) = \phi_{out}^{(0)}(\vec{r}, t) + \phi_{out}^{(1)}(\vec{r}, t)\zeta + \phi_{out}^{(2)}(\vec{r}, t)\zeta^2 + \dots \quad (3.32)$$

$$\mu_{out}(\vec{r}, t, \zeta) = \mu_{out}^{(0)}(\vec{r}, t) + \mu_{out}^{(1)}(\vec{r}, t)\zeta + \mu_{out}^{(2)}(\vec{r}, t)\zeta^2 + \dots \quad (3.33)$$

Substituting Eq. 3.32 into Eq. 3.30, we obtain to the zeroth order in ζ

$$\nabla \cdot \left[M(\phi_{out}^{(0)}) \nabla \left(\frac{\partial f}{\partial \phi_{out}^{(0)}} \right) \right] = 0. \quad (3.34)$$

Eq. 3.34 is satisfied with the solution of

$$\begin{aligned} \phi_{out}^{(0)}(\vec{r}) &= 1 \quad \forall \vec{r} \in \Omega_+ \\ \phi_{out}^{(0)}(\vec{r}) &= 0 \quad \forall \vec{r} \in \Omega_-, \end{aligned} \quad (3.35)$$

where Ω_{\pm} are the two bulk phase regions. This solution asserts that far from the interface, we have one of the equilibrium phases. By substituting Eqs. 3.32 and 3.33

into Eq. 3.31 and collecting the zeroth order of ζ , we find

$$\mu_{out}^{(0)} = \frac{\partial f}{\partial \phi_{out}^{(0)}}. \quad (3.36)$$

Substituting Eq. 3.35 into Eq. 3.36 yields

$$\mu_{out}^{(0)}(\vec{r} \in \Omega_{\pm}) = 0. \quad (3.37)$$

To denote the inner solution, we replace the variable δ with ζ , μ with μ_{in} and ϕ with ϕ_{in} . To facilitate the inner expansion, we introduce a moving coordinate system (M.C.S.): one coordinate r is parallel to $\nabla\phi$, while the other coordinate is the arclength s along the interface (which is located at $r = 0$). The operators close to the interface ($r \approx 0$) are given by:

$$\nabla = \vec{e}_r \frac{\partial}{\partial r} + \vec{e}_s \frac{\partial}{\partial s}, \quad \nabla^2 = \frac{\partial^2}{\partial r^2} + \kappa_c \frac{\partial}{\partial r} + \frac{\partial^2}{\partial s^2}, \quad (3.38)$$

where κ_c is the local curvature. Introducing a stretched variable $z = r/\zeta$,

$$\nabla = \vec{e}_r \frac{1}{\delta} \frac{\partial}{\partial z} + \vec{e}_s \frac{\partial}{\partial s}, \quad \nabla^2 = \frac{1}{\delta^2} \frac{\partial^2}{\partial z^2} + \kappa_c \frac{1}{\delta} \frac{\partial}{\partial z} + \frac{\partial^2}{\partial s^2}. \quad (3.39)$$

$$\frac{\partial}{\partial t} = \left(\frac{D}{Dt} \right) - V_n \frac{1}{\delta} \frac{\partial}{\partial z} - V_s \frac{\partial}{\partial s}, \quad (3.40)$$

where V_n and V_s are the normal and tangential velocities, and D/Dt represents the material derivative, which is the derivative taken based on the M.C.S. Multiplying Eq. 3.30 by ζ^2 and rewriting it in terms of a new field variable ϕ in the M.C.S. yields

$$-V_n \frac{\partial \phi}{\partial z} \zeta^3 + \left(\frac{D\phi}{Dt} - V_s \frac{\partial \phi}{\partial s} \right) \zeta^4 = \frac{\partial}{\partial z} \left(M \frac{\partial \mu}{\partial z} \right) + \zeta \kappa_c M \frac{\partial \mu}{\partial z} + \zeta^2 \frac{\partial}{\partial s} \left(M \frac{\partial \mu}{\partial s} \right). \quad (3.41)$$

Expanding the fields in the power of ζ gives:

$$\phi_{in}(z, s, t, \zeta) = \phi_{in}^{(0)}(z, s, t) + \phi_{in}^{(1)}(z, s, t)\zeta + \phi_{in}^{(2)}(z, s, t)\zeta^2 + \dots \quad (3.42)$$

$$\mu_{in} = \mu_{in}^{(0)} + \mu_{in}^{(1)}\zeta + \mu_{in}^{(2)}\zeta^2 + \dots \quad (3.43)$$

Substituting Eq. 3.42 and 3.43 into Eq. 3.41 and collecting the zeroth order of ζ leads to:

$$\frac{\partial}{\partial z} \left[M(\phi_{in}^{(0)}) \frac{\partial \mu_{in}^{(0)}}{\partial z} \right] = 0. \quad (3.44)$$

Integrating Eq. 3.44 with respect to z yields

$$M(\phi_{in}^{(0)}) \frac{\partial \mu_{in}^{(0)}}{\partial z} = g_0(s, t). \quad (3.45)$$

Taking the limit $z \rightarrow \pm\infty$ and matching with Eq. 3.37, we obtain

$$M(\phi_{in}^{(0)}) \frac{\partial \mu_{in}^{(0)}}{\partial z} = 0. \quad (3.46)$$

Because $\phi_{in}^{(0)}$ should vary smoothly from 1 to 0 as z transitions from $+\infty$ to $-\infty$, $M(\phi_{in}^{(0)})$ is expected to be nonzero. We thus have

$$\frac{\partial \mu_{in}^{(0)}}{\partial z} = 0 \quad \text{or} \quad \mu_{in}^{(0)}(z, s, t) = g_1(s, t). \quad (3.47)$$

Matching Eq. 3.47 with the zeroth order in outer field, the profile of ϕ_{in}^0 along the z -direction is governed by

$$\mu_{in}^{(0)} = 0 = \frac{\partial f}{\partial \phi_{in}^{(0)}} - \frac{\partial^2 \phi_{in}^{(0)}}{\partial z^2}, \quad (3.48)$$

which leads to the following relationship that is useful in change of variables:

$$\frac{\partial \phi_{in}^{(0)}}{\partial z} = \sqrt{2f(\phi_{in}^{(0)})}. \quad (3.49)$$

Collecting the first order of ζ in Eq. 3.41 gives:

$$\frac{\partial}{\partial z} \left(\frac{\partial \mu_{in}^{(1)}}{\partial z} \right) + \kappa_c \frac{\partial \mu_{in}^{(0)}}{\partial z} = 0, \quad (3.50)$$

which in turn gives $\mu_{in}^{(1)} = \mu_{in}^{(1)}(s)$, or $\mu_{in}^{(1)}$ is independent of z . Similarly, collecting the second order of ζ in Eq. 3.41, we find that $\mu_{in}^{(2)} = \mu_{in}^{(2)}(s)$, or $\mu_{in}^{(2)}$ is independent of z . Finally, by collecting the third order of ζ in Eq. 3.41 and considering that $\mu_{in}^{(1)}$ and $\mu_{in}^{(2)}$ are independent of z , we have:

$$-V_n \frac{\partial \phi_{in}^{(0)}}{\partial z} = \frac{\partial}{\partial z} \left[M(\phi_{in}^{(0)}) \frac{\partial \mu_{in}^{(3)}}{\partial z} \right] + \frac{\partial}{\partial s} \left[M(\phi_{in}^{(0)}) \frac{\partial \mu_{in}^{(1)}}{\partial s} \right]. \quad (3.51)$$

Integrating Eq. 3.51 from $z = -\infty$ to $z = \infty$ gives:

$$V_n = -\frac{\partial}{\partial s} \left[\int_{-\infty}^{\infty} M(\phi_{in}^{(0)}) dz \right] \frac{\partial \mu_{in}^{(1)}}{\partial s} = -I \cdot \frac{\partial^2 \mu_{in}^{(1)}}{\partial s^2}, \quad (3.52)$$

where we assume a constant $I = \int_{-\infty}^{\infty} M(\phi_{in}^{(0)}) dz$ as it is independent of s . Also, substituting Eq. 3.42 and 3.43 into Eq. 3.29 and collecting the first order terms of ζ leads to:

$$\mu_{in}^{(1)} = \frac{\partial^2 f}{\partial \phi_{in}^2} \phi_{in}^{(1)} - \frac{\partial^2 \phi_{in}^{(1)}}{\partial z^2} - \kappa_c \frac{\partial \phi_{in}^{(0)}}{\partial z}. \quad (3.53)$$

Multiplying Eq. 3.53 by $\partial \phi_{in}^{(0)} / \partial z$ and integrating over z from $-\infty$ to ∞ gives:

$$\mu_{in}^{(1)} = -\kappa_c \int_{-\infty}^{\infty} \left(\frac{\partial \phi_{in}^{(0)}}{\partial z} \right)^2 dz. \quad (3.54)$$

Performing a change of variables in Eq. 3.54 using the relationship given in Eq. 3.49 leads to:

$$\mu_{in}^{(1)} = -\kappa_c \int_0^1 \sqrt{2f(\phi_{in}^{(0)})} d\phi = -\kappa_c \cdot J, \quad (3.55)$$

, wherein we assume a constant $J = \int_0^1 \sqrt{2f(\phi_{in}^{(0)})} d\phi_{in}^{(0)}$. Combining Eq. 3.55 and Eq. 3.52 results in:

$$V_n = I \cdot J \cdot \frac{\partial^2 \kappa_c}{\partial s^2} \quad (3.56)$$

Performing the integration of I and J (dropping the superscripts and subscripts for convenience) leads to:

$$J = \int_0^1 \phi(1 - \phi) d\phi = \frac{1}{6}. \quad (3.57)$$

$$I = \int_{-\infty}^{\infty} M(\phi) dz = \int_0^1 \frac{M(\phi)}{\sqrt{2f}} d\phi = \bar{M}_s \int_0^1 \phi(1 - \phi) d\phi = \frac{\bar{M}_s}{6}. \quad (3.58)$$

Substituting I and J into Eq. 3.56 and restoring the dimensions gives:

$$V_n \frac{L^3}{D} = -\frac{\bar{M}_s L^3}{36} \frac{\partial^2 \kappa_c}{\partial s^2}. \quad (3.59)$$

Comparing the dimension-restored equation derived from the asymptotic analysis with the corresponding sharp interface equation, Eq. 3.24, we find

$$\frac{D \bar{M}_s}{36} = M_s \delta \gamma = \frac{\gamma_s D_s \delta_s}{k_B T N_v}, \quad (3.60)$$

, which indicates that $M_s = D_s \delta_s / k_B T N_v \delta$, provided the choice of $\gamma = \gamma_s$; that is, we find that the surface mobility is proportional to surface diffusivity. Choosing $\bar{M}_s = 36$, the model variable D is connected to the surface diffusivity D_s as follows:

$$D = \frac{\gamma_s D_s \delta_s}{k_B T N_v}. \quad (3.61)$$

The time scale that links the simulation time to the physical time is acquired from Eq. 3.61 as

$$\tau = \frac{L^4 k_B T N_v}{\gamma_s D_s \delta_s}. \quad (3.62)$$

3.5 Numerical methods

One of the challenges in modeling Ni-YSZ anode coarsening is the fact that solving Cahn-Hilliard equations with an explicit time iteration scheme is too expensive, especially for 3D large-scale simulations. Thus, we solve the evolution equations with the algorithm based on splitting the fourth-order Cahn-Hilliard equation into two second-order equations and solving them for the OPs and chemical potentials simultaneously [113]. Taking Model B as an example, Eq. 3.22 can be split as

$$\frac{\partial(\psi\phi)}{\partial t} = \nabla \cdot [(\psi M)\nabla\mu] \quad (3.63)$$

$$\mu = f_\phi - \frac{\epsilon^2}{\psi} \left(\nabla \cdot (\psi \nabla \phi) + \frac{|\nabla \psi| \sqrt{2f}}{\epsilon} \cos \theta \right), \quad (3.64)$$

We use the central-differencing method for spatial discretization and Newton's method for non-linear terms. We consider the relationship $B = \psi M$, wherein ψ is assumed to be time independent, $M = M(\phi)$, and the mesh dimension is uniform ($\Delta x = \Delta y = \Delta z = h$). The finite-difference equations are then

$$\begin{aligned} \phi^{n+1} + \frac{dt}{2h^2\psi} & \left[(B_{i+1} + B)(\mu_{i+1}^n - \mu^{n+1}) - (B + B_{i-1})(\mu^{n+1} - \mu_{i-1}^n) + \right. \\ & (B_{j+1} + B)(\mu_{j+1}^n - \mu^{n+1}) - (B + B_{j-1})(\mu_j^{n+1} - \mu_{j-1}^n) + \\ & \left. (B_{k+1} + B)(\mu_{k+1}^n - \mu^{n+1}) - (B + B_{k-1})(\mu^{n+1} - \mu_{k-1}^n) \right] \mu^{n+1} \quad (3.65) \\ = \phi^n + \frac{dt}{2h^2\psi} & \left[(B_{i+1} + B)\mu_{i+1}^n + (B + B_{i-1})\mu_{i-1}^{n+1} + (B_{j+1} + B)\mu_{j+1}^n + \right. \\ & \left. (B + B_{j-1})\mu_{j-1}^n + (B_{k+1} + B)\mu_{k+1}^n + (B + B_{k-1})\mu_{k-1}^n \right]. \end{aligned}$$

$$\begin{aligned}
& \mu^{n+1} - f_{\phi\phi}^n \phi^{n+1} - \frac{\epsilon^2}{2h^2\psi} \left[(\psi_{i+1} + \psi) + (\psi + \psi_{i-1}) + (\psi_{j+1} + \psi) + \right. \\
& \quad \left. (\psi + \psi_{j-1}) + (\psi_{k+1} + \psi) + (\psi + \psi_{k-1}) \right] \phi^{n+1} \\
& = f_{\phi}^n - f_{\phi\phi}^n \phi^n - \frac{\epsilon^2}{2h^2\psi} \left[(\psi_{i+1} + \psi)\phi_{i+1}^n + (\psi + \psi_{i-1})\phi_{i-1}^n + (\psi_{j+1} + \psi)\phi_{j+1}^n + \right. \\
& \quad \left. (\psi + \psi_{j-1})\phi_{j-1}^n + (\psi_{k+1} + \psi)\phi_{k+1}^n + (\psi + \psi_{k-1})\phi_{k-1}^n \right] \\
& \quad - \frac{\epsilon |\nabla\psi| \cos\theta}{\psi} \sqrt{2f}.
\end{aligned} \tag{3.66}$$

Note that in this shorthand notation, if any elements of a spatial index of a variable belongs to the central grid, that is, grid (i, j, k) , that element in the subscript of the variable is not explicitly denoted.

To solve Eqs. 3.65 and 3.66, a pointwise Gauss-Seidel relaxation scheme and a red-black checkerboard iteration scheme are used together to accelerate the convergence rate and facilitate the parallelization. The pointwise scheme is implemented by solving Eq. 3.67 for every mesh point of the entire domain in the sequence of increasing indexes

$$\begin{bmatrix} a_{1,1} & a_{1,2} \\ a_{2,1} & a_{2,2} \end{bmatrix} \begin{Bmatrix} \phi \\ \mu \end{Bmatrix} = \begin{Bmatrix} b_1 \\ b_2 \end{Bmatrix} \tag{3.67}$$

In order to enhance the numerical stability, the Crank-Nicholson algorithm for time discretization is utilized. This semi-implicit scheme significantly reduces the stiffness of the numerical integration, thus allowing a much larger time step size. The

coefficients in Eq. 3.67 are then given by:

$$\begin{aligned}
a_{1,1} &= 1 \\
a_{1,2} &= \frac{dt}{4h^2\psi} \left(M_{i+1}\psi_{i+1} + M_{i-1}\psi_{i-1} + M_{j+1}\psi_{j+1} + M_{j-1}\psi_{j-1} + M_{k+1}\psi_{k+1} \right. \\
&\quad \left. + M_{k-1}\psi_{k-1} \right) \\
b_1 &= \phi^n - \frac{dt}{4h^2\psi} \left(M_{i+1}\psi_{i+1} + M_{i-1}\psi_{i-1} + M_{j+1}\psi_{j+1} + M_{j-1}\psi_{j-1} + M_{k+1}\psi_{k+1} \right. \\
&\quad \left. + M_{k-1}\psi_{k-1} \right) \mu^n + \frac{dt}{2h^2\psi} \left(B_{i+\frac{1}{2}}\mu_{i+1}^{m+\frac{1}{2}} + B_{i-\frac{1}{2}}\mu_{i-1}^{m+\frac{1}{2}} + B_{j+\frac{1}{2}}\mu_{j+1}^{m+\frac{1}{2}} \right. \\
&\quad \left. + B_{j-\frac{1}{2}}\mu_{j-1}^{m+\frac{1}{2}} + B_{k+\frac{1}{2}}\mu_{k+1}^{m+\frac{1}{2}} + B_{k-\frac{1}{2}}\mu_{k-1}^{m+\frac{1}{2}} \right).
\end{aligned} \tag{3.68}$$

$$\begin{aligned}
a_{2,2} &= 1 \\
a_{2,1} &= -f_{\phi\phi} - \frac{\epsilon^2}{2h^2\psi} \left(\psi_{i+1} + \psi_{i-1} + \psi_{j+1} + \psi_{j-1} + \psi_{k+1} + \psi_{k-1} + 6\psi \right) \\
b_2 &= f_{\phi} - f_{\phi\phi}\phi^n - \frac{\epsilon^2}{4h^2\psi} \left(\psi_{i+\frac{1}{2}}\phi_{i+1}^m + \psi_{i-\frac{1}{2}}\phi_{i-1}^{m+1} + \psi_{j+\frac{1}{2}}\phi_{j+1}^m \right. \\
&\quad \left. + \psi_{j-\frac{1}{2}}\phi_{j-1}^{m+1} + \psi_{k+\frac{1}{2}}\phi_{k+1}^m + \psi_{k-\frac{1}{2}}\phi_{k-1}^{m+1} \right).
\end{aligned} \tag{3.69}$$

Here, the superscript m denotes the intermediate time steps in comparison to the superscript n , which denotes the time stepping in Eq. 3.65 and Eq. 3.66.

In most cases, we find this solver is over 100 times faster than the explicit scheme. However, attention must be paid to the choice of the time stepping size. In some cases, when an overly large time step is used in our solver, the simulation results are incorrect even if the numerical scheme is stable.

When solving the coupled governing equations in Model A, the solver is parallelized with the Message Passing Interface (MPI) library to take advantage of multiple processors. In our MPI code, the domain is decomposed equally in size in each axial

direction, if possible, to achieve load balance. For instance, if 64 CPUs are allocated to the computation, the entire domain is decomposed into 4 by 4 by 4 sub-domains; that is, each sub-domain has a domain size of 1/64 of the original domain in volume or, more explicitly, 1/4 of the length of the original domain in each axis (assuming there are no residuals).

The solver for Model B is parallelized with both the MPI and openMP libraries. Because only one Cahn-Hilliard equation is solved, it is much more numerically stable and efficient in comparison to the Model A solver.

3.6 Error analysis: contact angles and the interfacial width

The phase-field model is known to smooth out microstructures with length scales below the diffuse interface thickness. This artificial smoothing process introduces errors during the early stages of a simulation, but has no negative effects on the analysis of long-term coarsening kinetics. In contrast, microstructural evolution kinetics can only be accurately resolved in PFMs when the length scale of the microstructure is larger than certain multiples of the interfacial thickness. In other words, there is a critical ratio between the microstructural length scale and the interfacial thickness that is required to obtain a sufficient agreement with the sharp-interface limit. For example, if a system contains particles with typical radii a few times smaller than the interface thickness, the simulations of its evolution will incur a large error. The commonly recognized critical ratio is of about 10. However, in large scale 3D simulations, to resolve a complicated system with microstructural features of different length scales, achieving this critical value for all features is impracticable because it would require a very high resolution. In practice, we use a smaller ratio, especially when there are smaller features among a range of feature sizes within the microstructure, and quantify the errors introduced by the selected value.

Because the coarsening kinetics of Ni-YSZ anodes has been found to depend

strongly upon the Ni-YSZ contact angle, an error analysis is performed via the investigation of the contact angle of Ni on the YSZ phase in two dimensions (2D). The two-dimensional domain is initialized with a bottom that is half occupied by YSZ and a top half that is equally divided into the Ni and pore phases with a 90° contact angle. The remainder of the domain is filled with the pore phase. The domain size is designed to be large enough so that no-flux BCs have negligible effects on the contact angles at the triple junction. The system is evolved with our Model B to its steady state. The final contact angle θ_C is calculated from the average value of the dot product of the normal,

$$\frac{\nabla\psi}{|\nabla\psi|} \cdot \frac{\nabla\phi}{|\nabla\phi|} = -\cos\theta_C. \quad (3.70)$$

over the region where the domain parameter ψ and the order parameter ϕ are both between 0.1 and 0.9, indicating the TPB region.

Two contact angles are studied: 120° and 93° . The 120° case is selected as a reference case because the cosine function is away from the extrema or inflection point at this contact angle. The 93° case corresponds to a physical contact angle of Ni on the YSZ phase that is based on our selected interfacial energies.

As the characteristic length of the system, we choose the domain size, which is varied from 10 points to 100 points in each direction, while the interfacial width is held at 4 grid points. Therefore, the ratio of the domain size to the interfacial width varies from 2.5 to 10. For the 10×10 domain, the interfacial region (either the domain or order parameters are between 0.1 and 0.9) occupies about half of the domain. As the domain size increases, the fraction becomes very small. The contact angles normalized to the set value versus the ratios of the domain size to the interfacial width are plotted in Fig. 3.1. In the case of a 120° contact angle, we find that the angle deviate from the sharp-interface value by less than 0.2° when the ratio is larger than 5. Even at a ratio of 2.5, the deviation is below 1 degree or 1%. In the case of a 93° contact angle, the contact angle differs from the sharp-interface value by less

than 0.5° , or 0.5%.

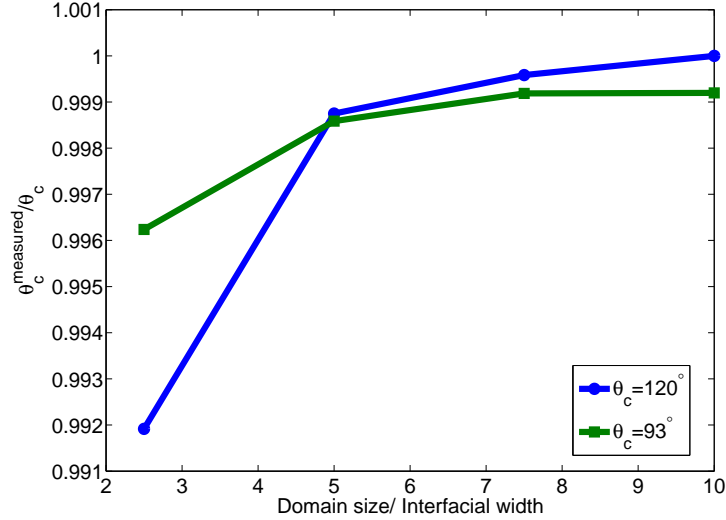


Figure 3.1: Normalized angle plotted with the ratio of the domain size to the interfacial width. The error decreases with an increasing ratio of the domain size to the interfacial width.

The interfacial width utilized in coarsening simulations is approximately $0.13 \mu\text{m}$. Based on our error analysis results, the contact angles of the Ni particles in the active and dead-end categories with a length scale larger than $0.32 \mu\text{m}$ can fairly accurately be modeled by using our Model B. In the isolated network, a length scale larger than $0.64 \mu\text{m}$ is needed for a fair accuracy. For the $(4 \mu\text{m})^3$ domain, only 3% in volume of the Ni phase belongs to clusters outside the accurate range. In addition, based on Young’s equation for a flat surface, a 0.5° difference in contact angle of the Ni phase corresponds to a 1.1% difference in Ni-YSZ interfacial energy. In other words, this model error has very limited effects on the coarsening kinetics of the Ni-YSZ anode.

3.7 Parameterization of the models

The aforementioned asymptotic analysis provides the mathematical ground for correlating simulations on the coarsening phenomenon with experimental results. However, to quantitatively model the physical process, the material-specific param-

eters in the governing equations must be specified based on the material properties. Most of these parameters can be found in the literature.

3.7.1 Mobility prefactors

As demonstrated in our asymptotic analysis, the mobility prefactor corresponding to the Ni-pore interface should be proportional to the surface self-diffusivity of Ni, which is usually anisotropic or depends on the crystallographic orientation. The Ni diffusivities based on the field ion microscope (FIM) measurements range from $10^{-13} \text{ m}^2\text{s}^{-1}$ in (110) to $10^{-9} \text{ m}^2\text{s}^{-1}$ in (331) at 1273 K [115, 116, 117]; these values are extrapolated at high temperatures and could be inaccurate, because FIM can be conducted only at low temperature regions ($T < 0.2T_m$, T_m is the melting temperature). On the other hand, the surface smoothing method (SSm) measures mass-transfer diffusion at high temperatures ($T > 0.7T_m$), which is generally averaged over crystallographic orientations [115]. The latter method provides a more appropriate value for the diffusivity ($\sim 10^{-10} \text{ m}^2\text{s}^{-1}$) during Ni coarsening at the modeled temperature (1000°C). In addition, the anisotropy of the Ni surface diffusivity was found to be relatively small in high temperature regions ($0.82 T_m < T < T_m$) in [108]. We thus consider an ensemble value $\sim 10^{-10} \text{ m}^2\text{s}^{-1}$ for the Ni surface diffusivity in our model.

Cation diffusion in oxides is related to various parameters, such as valence, atomic radius, impurity, and oxygen activity. In Ref. [118], it is reported that the bulk diffusivity of yttrium in YSZ (containing 10 to 32 mol% Y_2O_3) is slightly larger than that of zirconium in YSZ, and that the difference is less than an order of magnitude. The surface diffusion of Zr in YSZ is calculated from the measurements of the surface area reduction in powder compacts during sintering in Ref. [119], and the diffusivity at 1000 °C is found to be $\sim 10^{-16} \text{ m}^2\text{s}^{-1}$. We thus consider a surface diffusivity of YSZ of $10^{-16} \text{ m}^2\text{s}^{-1}$ in our simulations.

The diffusion mechanisms at metal-ceramic interfaces are less understood than those on metal or ceramic surfaces. The cohesiveness of the Ni-YSZ interface, which depends on the process used to fabricate the porous cermets, determines the interfacial structure and affects the effective interfacial diffusivity. A series of diffusion bonding experiments indicated that the metal-ceramic interface does not act as an efficient vacancy sink or mass transport path [120]. These findings suggest that the diffusivity at the Ni-YSZ interface should be much smaller than that of the Ni surface and the YSZ surface. In addition, the exact value of the diffusivity at the Ni-YSZ interface is not as important as that of Ni because the redistribution of Ni is observed to be the dominant morphological change during anode coarsening. The diffusivity of the Ni-YSZ interface is considered to be approximately $\sim 10^{-20} \text{ m}^2\text{s}^{-1}$.

Using these values, the mobility ratios among the three materials are set at $M_{\text{NiP}} : M_{\text{YP}} : M_{\text{NiY}} = 1 : 10^{-6} : 10^{-10}$, where the subscript Ni represents nickel, Y the YSZ and P the pore phase. For non-dimensionalization, a mobility scale of $10^{-10} \text{ m}^2\text{s}^{-1}$ is used.

3.7.2 Bulk and gradient energy coefficients

In a PFM, the balance between the bulk and the gradient energy terms in the free energy functional determines the thickness of the interface. The ratio of the interfacial thickness to the characteristic length of the system and the ratio of the domain size to the characteristic length are crucial for the validity of a PFM. It is known that an interface that is too thin can cause an unphysical pinning or halting of coarsening, whereas an interface that is too thick can lead to unphysical dissolution of particles [121]. Therefore, our task is to select bulk and gradient energy coefficients that result in an appropriate interfacial energy, while keeping the interfacial thickness sufficiently large so that the computation is feasible.

In a multi-phase system, using an unequal interfacial thickness among different in-

interfaces without a special treatment can cause erroneous evolution kinetics in a PFM simulation because the interfacial thickness changes the ratio of the simulation time scale to the physical time scale. Therefore, a single value for the interfacial thickness of all interfaces is set. For example, we set $\delta_{ij} = \Delta x$, which gives 4 points in the interfacial region to avoid the aforementioned pinning while optimizing the computational efficiency (Δx depends on the selected length scale in a non-dimensionalization). The interfacial energies are obtained from existing experimental or computational studies. These choices are then used in Eqs. 3.13 and 3.12 to determine the bulk and gradient energy coefficients.

The three interfaces that exist in the Ni-YSZ anode are the Ni surface (Ni-pore interface), the YSZ surface (YSZ-pore interface), and the Ni-YSZ interface. The Ni surface free energy has been widely investigated and the values reported in the literature are in good agreement. At 1000°C, the surface energy of $\sim 1.9 \text{ Jm}^{-2}$ for Ni has been measured [122]. A 8YSZ surface (8 mol % Y_2O_3) has been reported in Ref. [123]. It was studied at 1300~1600°C using a multiphase equilibrium technique. The YSZ surface free energy γ_{YSZ} was found to decrease linearly from 1.26 to 1.13 Jm^{-2} in the range of temperatures studied. By extrapolating this data, one obtains $\gamma_{\text{YP}} \sim 1.4 \text{ Jm}^{-2}$ at 1000°C. This value is used to parameterize our model. In Ref. [124], ab initio calculations have been reported with γ_{YP} ranging from 1.04 to 1.75 Jm^{-2} at $T = 0$, depending on the crystallographic orientation.

The free energy of a heterogeneous Ni-YSZ interface depends on the interfacial structure, which is complicated and depends on the fabrication process. Nikolopoulos *et al.* experimentally measured the non-reactive contact angle between molten Ni and 8YSZ at 1500°C and found a value of 117°, which suggests an interfacial energy of 1.95 Jm^{-2} [125]. Although this wetting experiment was not conducted at normal SOFC operating temperatures, the result implies a poor wettability at the Ni-YSZ interface.

Several ab initio calculations on bond formation at Ni-YSZ interfaces have been reported [126]. A strong bonding between Ni-Zr and Ni-O was found at the Ni(100)/ZrO₂(100) polar interfaces, and an interfacial tension of $\sigma_{(100)} = 1.04 \text{ Jm}^{-2}$ was reported. Another local minimum appeared at the ZrO₂/Ni(111) interface where $\sigma_{(111)} = 1.80 \text{ Jm}^{-2}$ [127]. However, Ni-YSZ interfaces formed subsequent to sintering are multifaceted. Despite the lack of understanding of these interfaces, we know the range of reasonable interfacial energies at Ni-YSZ interfaces. In our simulations, $\gamma_{\text{NiY}} = 1.50 \text{ Jm}^{-2}$ is used.

In view of the above discussion, we assume that the gradient energy coefficient ratios are $\gamma_{\text{NiP}} : \alpha_{\text{NiY}}^2 : \alpha_{\text{YP}}^2 = 1.9 : 1.5 : 1.4$ based on a surface energy scale of 1 Jm^{-2} , which derives the bulk energy coefficient ratios as $k_{\text{Ni}} : k_{\text{Y}} : k_{\text{P}} = 1 : 0.5 : 0.9$.

3.8 Initial smoothing, boundary filling, and post processing of Model B

An initial construction of the domain parameter ψ is required for Model B simulations. To retain the topological and morphological features of the 3D reconstructed data and to develop the diffuse interfacial profile of the domain parameter, a conserved Allen-Cahn dynamics is used. The governing equation sets for a three-phase system can be written as

$$\frac{\partial \phi_1}{\partial t} = -M (\mu_1 - \bar{\mu}_1), \quad (3.71)$$

$$\frac{\partial \phi_2}{\partial t} = -M (\mu_2 - \bar{\mu}_2),$$

where M is the mobility, ϕ_i represent the order parameters with a constraint $\sum_{i=1}^3 \phi_i = 1$, $\mu_i = \delta F / \delta \phi_i$ is the chemical potential, and $\bar{\mu}_i$ is the average of μ_i over the computational domain.

This initial smoothing using Eq. 3.71 usually requires only around 1 unit of di-

dimensionless time (with Δx set to unity) to achieve the development of the interfacial profile of ψ . As shown in Figs. 3.2 and 3.3, the topological features are retained well with only slight morphological changes after this initial smoothing.

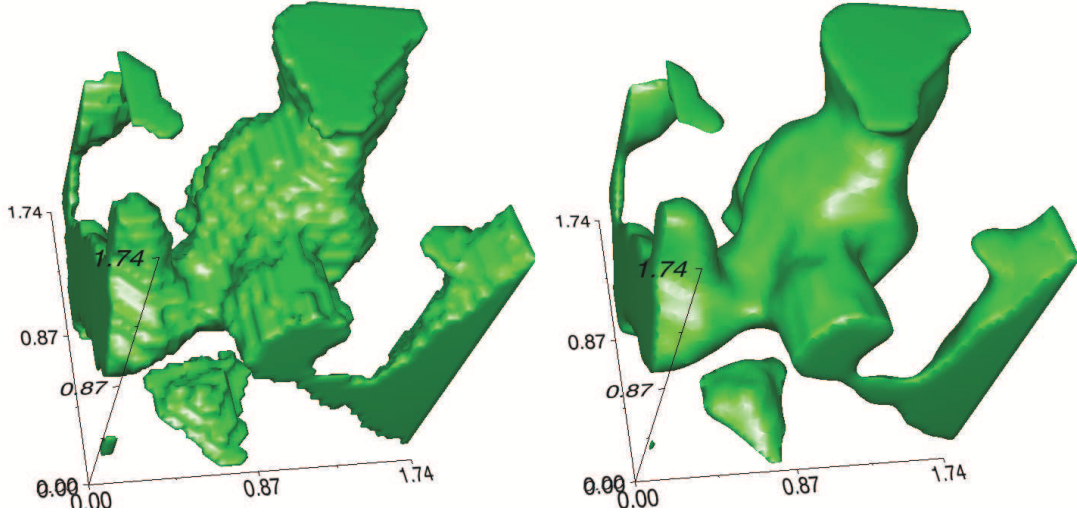


Figure 3.2: Comparison of microstructures of the Ni phase of a $(1.74\mu\text{m})^3$ sample. The left figure shows the voxelated experimental data and the right figure shows the smoothed structure using Allen-Cahn dynamics (evolved for 0.8 unit of dimensionless time with grid spacing of one).

After acquiring the smoothed structure, a “domain boundary filling” procedure is required to avoid the unphysical mass loss that stems from a self-filling of the interfacial regions of the domain boundaries at the beginning of the simulations. This boundary self-filling is required by the SBM for contact angle BCs so that the interfacial normals are well defined in the TPB regions. To prevent this mass loss, ϕ values are set to 1 in regions where $0.5 < \psi < 0.95$ and $0.05 < \phi < 0.95$ before a simulation is carried out. The upper bound of 0.95 is chosen to be consistent with the mobility cutoff. This value has very small effects on the mass since the boundary self-filling occurs rapidly and the gap will be filled very soon. Another reason for choosing this initial boundary-filling criteria is demonstrated in a moving droplet test shown in Fig. 3.4. After evolution, a droplet that is filled above $\psi > 0.5$ is found to have mass only 2% less than the initial setup, whereas the one filled above $\psi > 0.1$

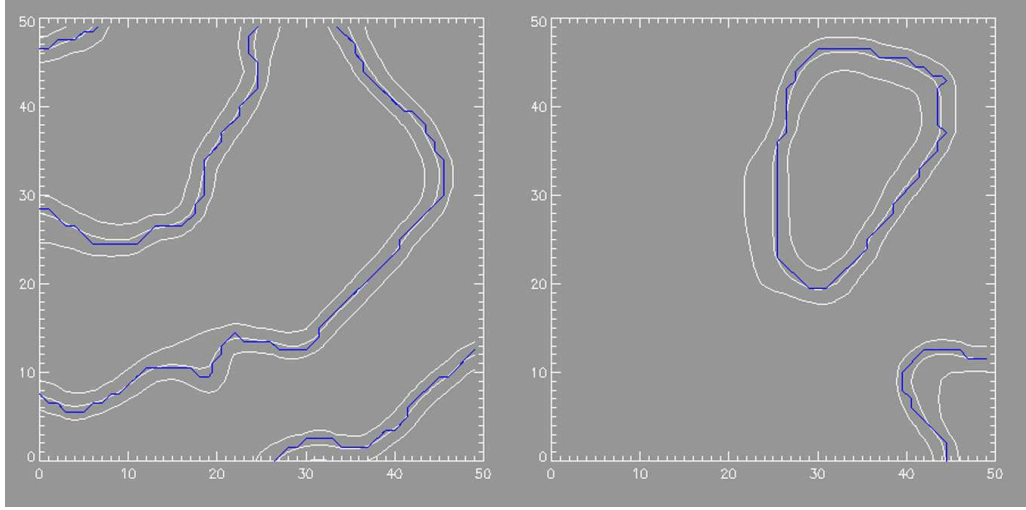


Figure 3.3: 2D contour plots of the Ni phase of a $(1.74\mu m)^3$ sample. The axes are represented in the mesh unit, each of which equals $0.348\mu m$. The left figure shows the $z=20$ slice, and the right one represents the $z=40$ slice. White curves are the 0.1, 0.5, and 0.9 contours of the smoothed Ni OP values. The blue curves indicate the Ni interfaces of the experimental data. The 0.5 contours differ from the original Ni interfaces by less than one mesh size for the most part, which indicates that the initial smoothing generally preserves the original morphological features.

leads to a mass that is approximately 30% larger. Even though the mass differs, the center of mass of the droplets in the two cases are nearly identical after evolving for a significant amount of time. That is, the amount of boundary filling has very limited effects on the evolution dynamics when the mass of the original phase is not significantly altered due to the filling.

Another difficulty associated with Model B is that the information of one of the phase (in our case, the pores) is missing because the domain parameter ψ and the order parameters for the other two mobile phases (namely, ϕ_1 and ϕ_2) are no longer constrained by $(1 - \psi) + \phi_1 + \phi_2 = 1$. A post processing of the Model B results is thus necessary to restore the information of the three phases for further analyses.

Here, the post processing is performed according to the algorithm as follows. Because the domain parameter ψ represents the complementary domain of the YSZ phase, the order parameter of the YSZ phase can be determined as $\phi_{\text{YSZ}} = 1 - \psi$.

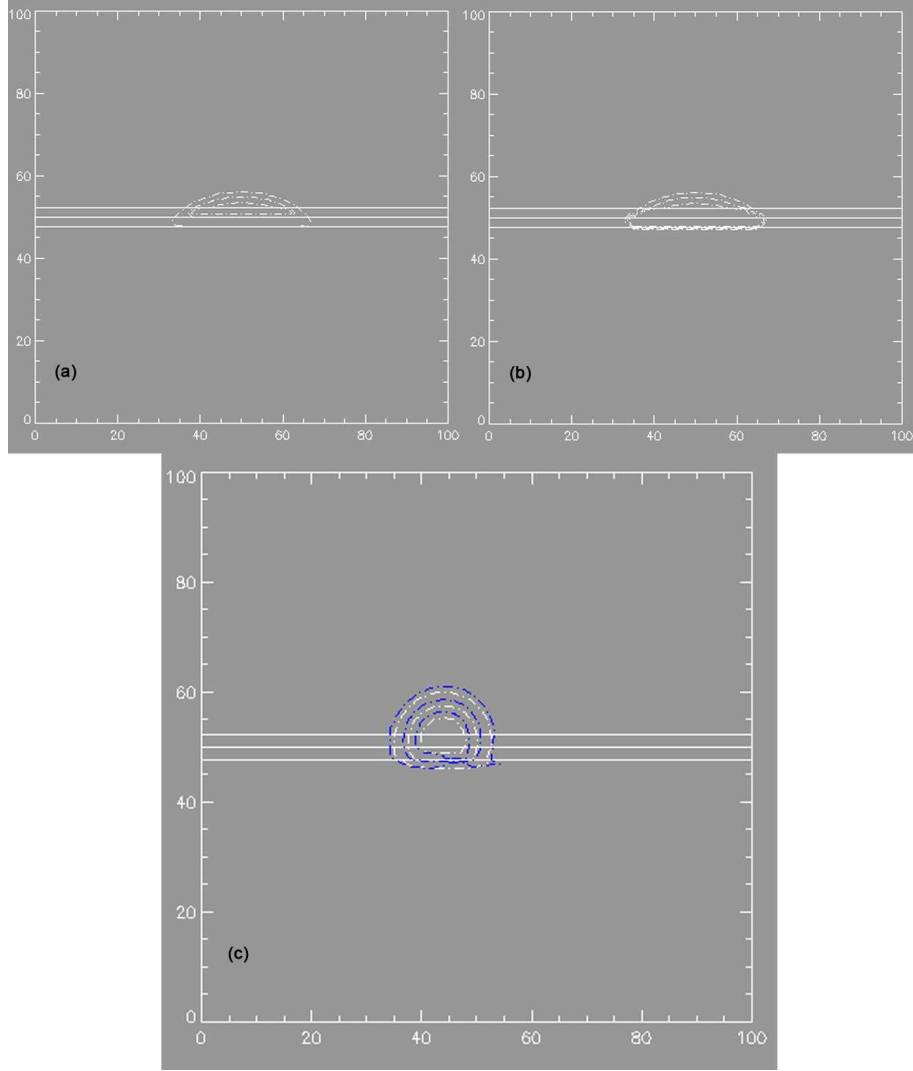


Figure 3.4: Moving droplet tests for the boundary filling effect on evolution dynamics. The droplet motion is driven by unequal surface tensions and the mass transport is mediated by surface diffusion. The top left figure (a) shows the initial shape of a droplet that is filled above $\psi = 0.5$ whereas the top right figure (b) shows a droplet that is filled above $\psi = 0.1$ (dashed curves are contours of ϕ). Solid lines are contours of ψ at levels 0.1, 0.5, and 0.9 (from the bottom to top). In the bottom figure, blue dash-dot curves represent the contour of the 90% filled droplet, whereas the white ones show the half-filled droplet. After 2500000 dimensionless time of evolution (with $\Delta x = 1$), the center of mass of the two droplets are nearly identical, even though the initial filling slightly altered the mass.

The order parameter of Ni, ϕ_{Ni} , is calculated using the following criteria to modify the value of the order parameter ϕ in Model B formulation: an intermediate variable

ϕ' is introduced as

$$\phi' = \begin{cases} 1, & \text{if } 0.5 < \psi \text{ and } \phi < 1, \\ \phi, & \text{otherwise.} \end{cases} \quad (3.72)$$

Then, the Ni order parameter ϕ_{Ni} is determined by

$$\phi_{\text{Ni}} = \phi' \cdot \psi. \quad (3.73)$$

The order parameter for the pore phase, ϕ_{pore} , is thus obtained as

$$\phi_{\text{pore}} = 1 - \phi_{\text{Ni}} - \phi_{\text{YSZ}}. \quad (3.74)$$

As shown in Fig. 3.5, the profile of ϕ_{Ni} at the overlapped Ni and YSZ interfacial regions are accurately described after this post treatment.

The combination of the initial filling of the boundary region and post processing leads to a net reduction of mass by less than 2% throughout the simulation which mainly takes place during the early evolution when mass redistributes within the domain boundary regions. This amount of mass change has very limited effects on analyses of the coarsening dynamics, as demonstrated in a moving droplet test shown in Fig.3.4.

Another post processing procedure is used to obtain the phase information for the TPB calculations because of the aforementioned boundary self-filling. This is because the order parameters identified above can not completely eliminate the pore phase at Ni and YSZ boundaries. Although this small amount of pores have very limited effect on the mass, it can lead to mis-identification of TPBs. Thus, alternative order parameters are identified based on the following criteria:

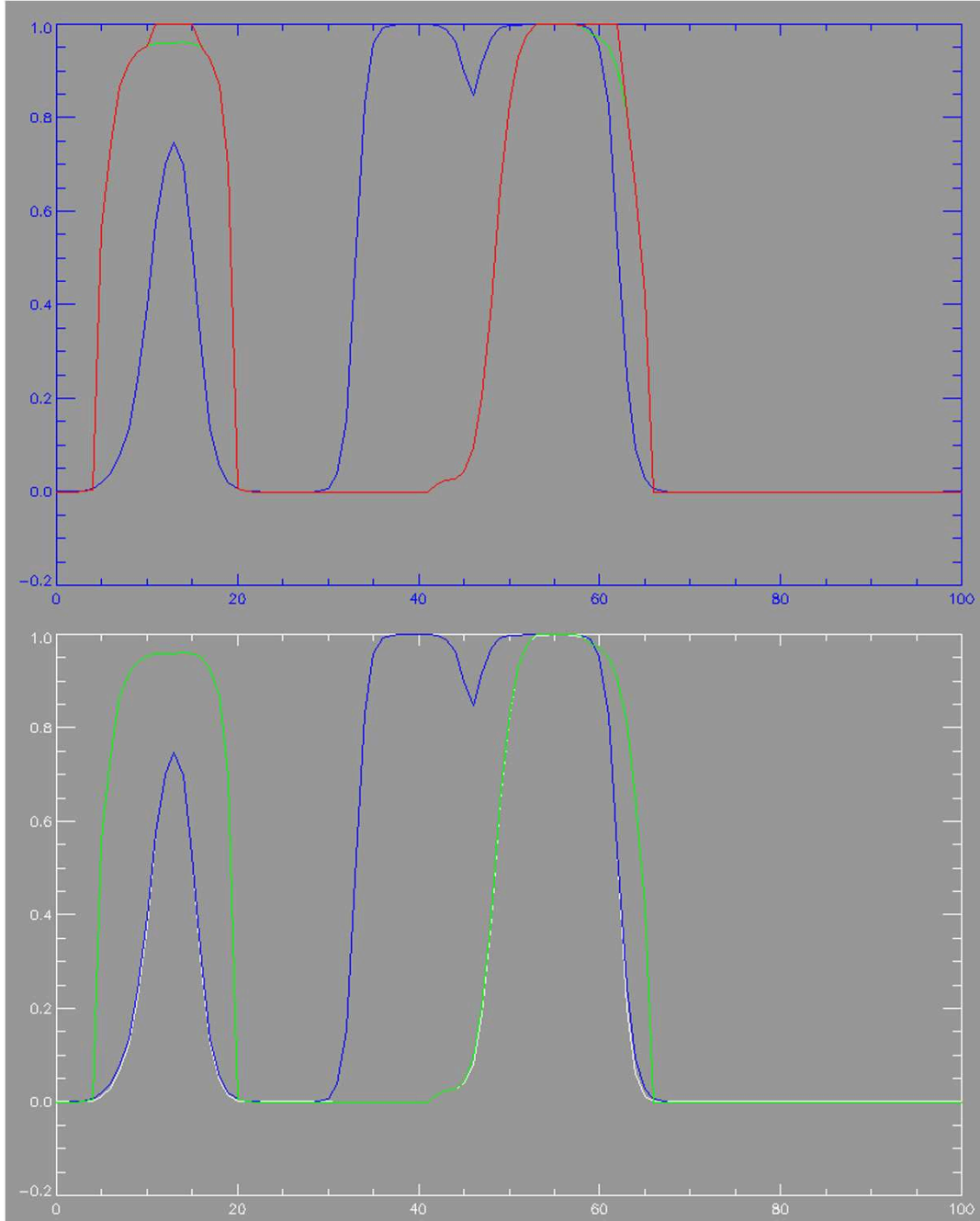


Figure 3.5: A 1D profile of the order and domain parameters from Model B simulation. The blue curve shows the profiles of ψ , green shows that of ϕ , the red curve indicates the profile of the intermediate variable ϕ' , and the white curve is the profile of ϕ_{Ni} . The profile of ϕ_{Ni} at the overlapped Ni and YSZ interfacial regions are accurately described with the proposed post processing.

$$\begin{aligned}
\phi_{\text{Ni}}^{\text{TPB}} &= \phi' \cdot \psi, = \phi_{\text{Ni}}, \\
\phi_{\text{YSZ}}^{\text{TPB}} &= 1 - \psi = \phi_{\text{YSZ}}, \\
\phi_{\text{pore}}^{\text{TPB}} &= \max(1 - 1.2 \cdot (\phi_{\text{Ni}}^{\text{TPB}} + \phi_{\text{YSZ}}^{\text{TPB}}), 0)
\end{aligned} \tag{3.75}$$

Then, a skeletonization procedure is used to thin the overlapped voxels where $0.05 < \phi_{\text{Ni}}^{\text{TPB}} < 0.95$, $0.1 < \phi_{\text{YSZ}}^{\text{TPB}} < 0.9$, and $0.15 < \phi_{\text{pore}}^{\text{TPB}} < 0.9$ to determine the TPBs. The slightly different threshold values are selected to compensate for the shrinkage of the Ni profile, which leads to a small value of $\phi_{\text{pore}}^{\text{TPB}}$ after the post processing. The skeletonization algorithm will be further discussed in the next section. As shown in Fig. 3.6, TPBs are accurately identified from Model B results with this processing.

3.9 3D data analysis

In three dimensions, a boundary at which three phases coincide has only one degree of freedom in space, i.e., the TPB is a line in the Ni-YSZ anode where the Ni, YSZ, and pore phases are all in contact. However, to identify the TPBs based on the microstructure reconstructed by FIB-SEM, some data processing is necessary since the microstructural data are represented by a 3D matrix. In this matrix, each phase is represented by regions in which voxel values are equal to a pre-determined constant. There are several methods to determine the TPB length in 3D volumetric data. For example, in Ref. [128], the TPBs are identified as the edges where three different voxels, each of which belongs to a different phase, are in contact. With some geometric corrections, the TPB length can be acquired with fair accuracy, but is limited by the resolution.

In our work, we adopt a thinning, or skeletonization, algorithm to determine the TPB regions, and count the voxels. In PFM simulations, the interfacial region is commonly identified as the zone over which an OP varies from 0.1 to 0.9. Because the interfaces in PFMs span multiple grid points, one can identify the diffuse TPB

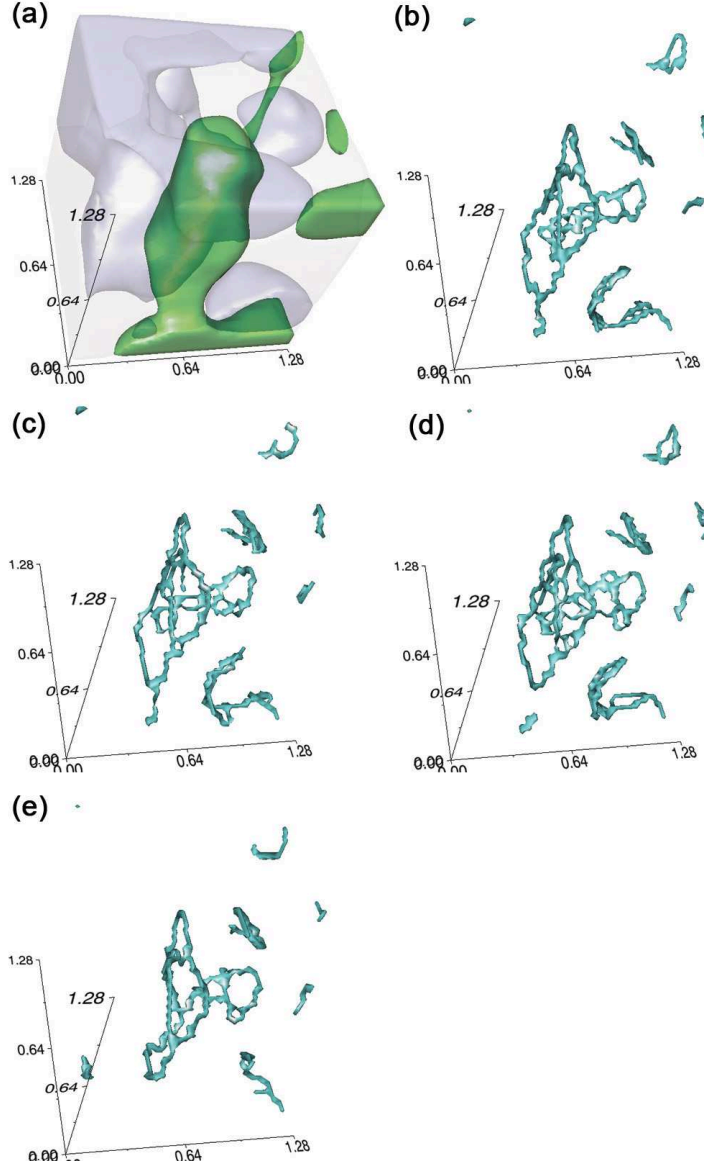


Figure 3.6: Comparison of the microstructure (a) and TPB distributions in a $(1.28\mu\text{m})^3$ portion of a 3D anode sample after initial-smoothing (b) (TPB density of $5.5\mu\text{m}^{-2}$), boundary filling (c) (TPB density of $5.7\mu\text{m}^{-2}$), and ten-second coarsening using Model B (d) (TPB density of $5.5\mu\text{m}^{-2}$). The Ni, pore, and YSZ phases are represented in green, semi-transparent blue, and semi-transparent grey, respectively. TPBs (light blue) are accurately identified with our post processing. While there are small changes between (b) and (c), they are not significant compared to the change of TPBs after evolving over a long time (here, 11 hrs) (e)

regions as voxels in which all three OPs are between 0.1 and 0.9. (For Model B, the threshold values are slightly different due to the reason described in Sec. 3.8.)

In order to recover the one-dimensional nature of TPBs from this data, we use a thinning algorithm developed in Ref. [129], which reduces the diffuse TPB regions to the corresponding skeleton of chains of voxels. The key feature of this algorithm is that it preserves the topological characteristics of the original image/voxelated data (i.e., it does not allow the pinching or connection of regions).

The final TPB length is calculated via a multiplication of the physical grid size and the total number of TPB voxels after skeletonization. The used procedures may either overestimate or underestimate the TPB lengths depending on the angle at which the TPB lies within the grid; for an isotropic distribution of lines, the over/underestimation has been determined to be less than 13%. Because we have nearly isotropic distribution (i.e., anisotropy that only results from statistical variations), the error should be relatively consistent throughout the coarsening process and therefore not impact our investigation of the temporal evolution of the TPB length.

Not all of the TPBs are active; active TPBs must be simultaneously in contact with the three active phases that facilitate simultaneous transport of fuel, electrons, and oxygen ions. Since the electrochemical reactions occur only at or near these active TPBs, it is these active TPBs that contributes to the anode performance. Before identifying the active TPBs, we must first identify the active phases. Physically, a Ni phase cluster is active only if it connects the TPB sites to the current collector; a YSZ cluster is active only if it connects the TPBs to the electrolyte; and a pore cluster is active only if it connects the TPBs to the gas flow channels. However, the determination of such connectivities is feasible only if an anode structure that spans from the electrolyte to the current collector and to the gas channel is available. Our reconstructed microstructure, in contrast, constitutes only a portion of the entire span.

As a compromise, we follow the procedures described in Ref. [128], which categorize each bulk region into active, dead-end, or isolated clusters. Active clusters are

clusters that are connected to at least two sides of the sample domain boundaries, while isolated clusters are those that are not connected to any of the sides and are therefore electrochemically inactive. Dead-end clusters are defined as those that are in contact with only one side of the sample domain. In Ref. [128], a pre-smoothing procedure is used before this calculation to avoid artifacts resulting from image processing. Because PFM simulations naturally smooth microstructures over the length scale of the interfacial thickness, the pre-smoothing procedure is not necessary in our analysis. Note that in this procedure, a voxel is assumed to belong to a cluster if at least one of the 6 nearest neighbors is in the cluster. The active TPBs are then identified as those simultaneously in contact with the active networks of all three different phases. The TPB is marked as inactive as long as one of the phases adjacent to a TPB voxel is isolated. The remainder of the TPBs are considered unknown in terms of activity.

3.10 Results and Discussion

3.10.1 Contact angles at triple junctions

To validate our models, the mechanical equilibrium at a triple junction is examined in two dimensions with $\gamma_{13} : \gamma_{23} : \gamma_{12} = 1.9 \text{ Jm}^{-2} : 1.4 \text{ Jm}^{-2} : 2.2 \text{ Jm}^{-2}$. As shown in Fig. 3.7, the contact angles in both Model A and Model B are found to obey Young's equation at equilibrium. Note that in this case the initial profile of the domain parameter in Model B is given by the hyperbolic tangent.

One model that may be considered is Model A (with two OPs) where one of the OPs is held constant after proper initialization. Such a model has been proposed and applied by others [130, 131]. We find that this model would work only if the mobile phase completely wets the stationary phase as described in Ref. [131], but not when three-phase boundaries are involved. In a PFM, the interfacial energy is

controlled by the bulk and gradient energy coefficients, and an interface possesses the prescribed interfacial energy when the OP interfacial profile is in equilibrium (or near equilibrium when the interface is evolving). In Eq. (3.8), if one OP is held constant as proposed in Ref. [130], the other OPs cannot develop their equilibrium profiles. This leads to contact angles at triple junctions that are inconsistent with the solutions of Young’s equation. The full analysis of this problem is beyond the scope of this study. Here, we simply demonstrate that Young’s conditions are not met in Model A with one OP held constant, as shown in Fig. 3.7(C).

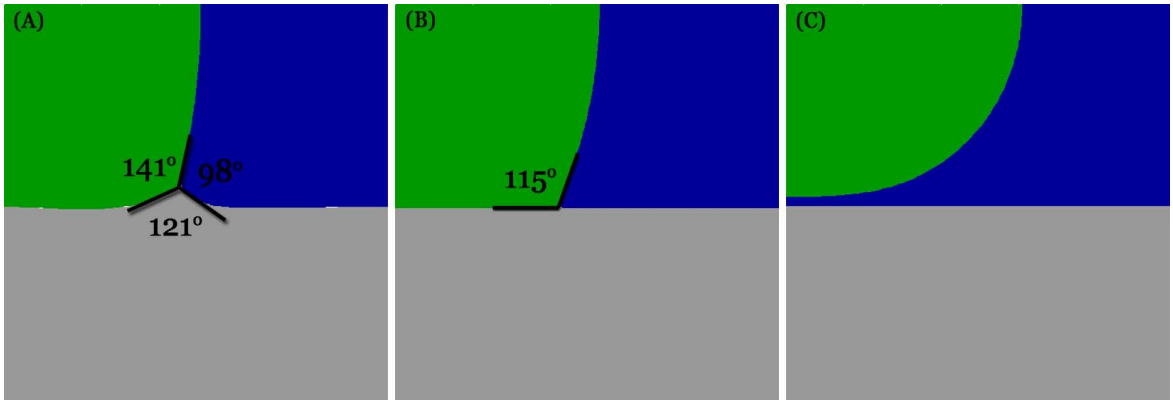


Figure 3.7: A comparison of equilibrium contact angles at triple junctions with three different models; phase 1, 2, and 3 are represented in green, gray, and blue, respectively: (A) the result of Model A; (B) the result of Model B; and (C) the result from evolving one order parameter in Model A. Note that the triple junction no longer exists at equilibrium in (C).

3.10.2 Comparison of Model A, Model B, and experimental results

To compare the coarsening kinetics in Model A and Model B, we use a Ni-YSZ anode microstructure with dimensions 3.48 by 3.48 by 3.48 μm^3 (Fig. 3.8, left) as initial conditions for both models to simulate Ni coarsening. This specimen is experimentally reconstructed from a functional layer of a Ni-YSZ anode via FIB-SEM [3], and then smoothed with the conserved Allen-Cahn dynamics, as discussed earlier. For convenience, subscripts 1, 2, and 3 are used here to represent the Ni, YSZ and pore phases,

respectively. To compare the simulation results with the complementary coarsening experiments, model parameters M_{ij} and γ_{ij} are determined based on the physical properties of the Ni-YSZ cermet at 1100°C as described in Sec 3.7. To summarize, the surface tensions of Ni and YSZ are set as $\gamma_{13} \cong 1.9 \text{ Jm}^{-2}$ and $\gamma_{23} \cong 1.4 \text{ Jm}^{-2}$ [123], and the corresponding surface diffusivities used are $D_{13} \cong 3 \times 10^{-10} \text{ m}^2\text{s}^{-1}$ [107, 108] and $D_{23} \cong 3 \times 10^{-16} \text{ m}^2\text{s}^{-1}$ [109]. The interfacial properties of Ni-YSZ interface are not well studied. We therefore use estimated values of $\gamma_{12} = 1.5 \text{ Jm}^{-2}$ [126, 127] and $D_{12} = 3 \times 10^{-20} \text{ m}^2\text{s}^{-1}$. For the reference case, $M_{13} : M_{23} : M_{12} = 1 : 10^{-6} : 10^{-10}$ and $\gamma_{13} : \gamma_{23} : \gamma_{12} = 1.9 : 1.4 : 1.5$ are used with a mobility scale of $3 \times 10^{-10} \text{ m}^2\text{s}^{-1}$ and a surface energy scale of 1 Jm^{-2} .

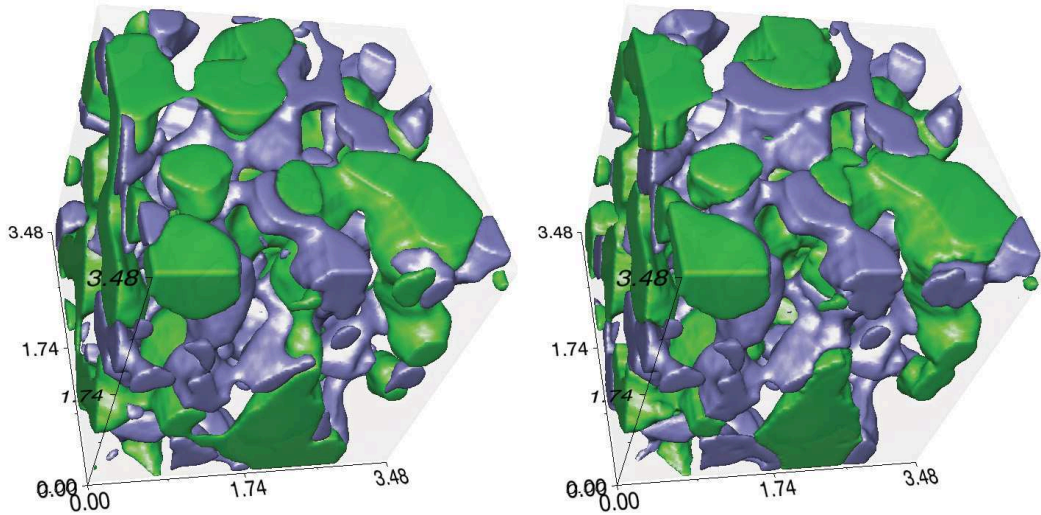


Figure 3.8: Comparison of the three phase anode before (left) and after (right) coarsening for 100 hours using Model B for the reference case. The Ni, pore, and YSZ phases are represented in green, blue, and semi-transparent, respectively (with volume fractions 26.9%, 16.6%, and 56.5%, respectively). The initial TPB density is $\sim 6.74 \mu\text{m}^{-2}$, and was reduced by 32.4% after coarsening.

A comparison of the anode microstructure before and after coarsening for 100 hours at 1100°C using model B is shown in Fig. 3.8. The evolution of the microstructure appears to be confined within a short distance. It is noteworthy that there are a few regions where the YSZ structure appears to evolve. These regions are, however,

visualization artifacts. As shown in Fig. 3.9, Model B predicts that the three-phase boundary (TPB) length becomes nearly constant after coarsening for tens of hours, while Model A indicates that the TPB continues to decrease slowly after a rapid early evolution. These results suggest that the Ni phase can be trapped in metastable or near metastable states when YSZ is immobile. Interestingly, the major portion of the total TPB reduction occurs during a relatively early stage of the coarsening in both models.

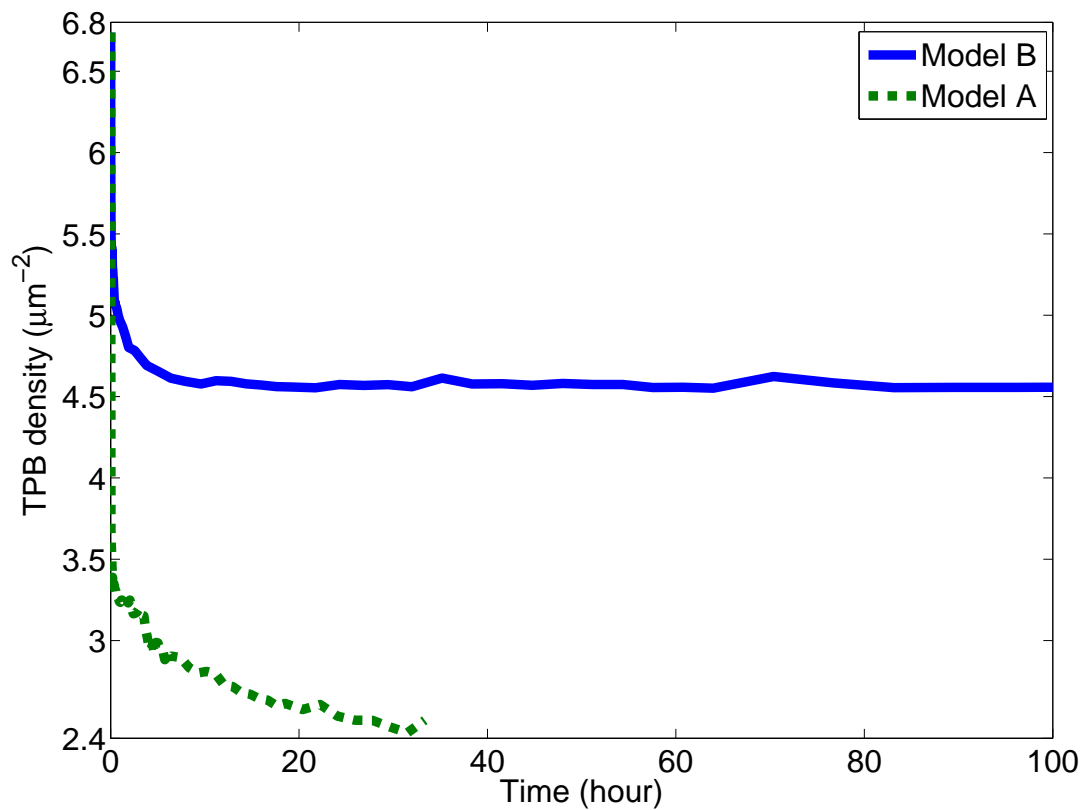


Figure 3.9: Comparison of the TPB reduction of Model A and Model B for the reference case.

For Model B, the overall TPB reduction after a 100-hour coarsening was found to be 32.4%. A preliminary experimental result for the corresponding case was found to be approximately 26% [132]. This difference is most likely introduced by the deviation of TPB densities within different samples or at different locations of a sample.

For instance, in the latter simulations we found approximately 20% of TPB reduction in a sample with a $5.22\mu\text{m}^{-2}$ initial TPB density. Because this particular sample has a $6.74\mu\text{m}^{-2}$ initial TPB density, small microstructural features with a larger driving force for coarsening are expected in this sample, which leads to a more rapid TPB density reduction. Other sources of uncertainties involved in our simulations include the values of diffusivities (which change the time scale), the interfacial/surface energies (which change the morphological evolution and the time scale), statistical variations of the microstructure in the selected volume, and a possible initial smoothing of very small unresolved structures. TPBs in Model A decreased by 62.7% after a 33-hour coarsening. The reduction was thus significantly overestimated by this model. The overestimation is mainly due to the fact that the mobility function used can introduce excess mobility at triple junctions, even with the cutoff, especially when the mobility values differ by orders of magnitude, as is the case here. Therefore, we find that Model B more accurately predicts the coarsening kinetics than Model A. As a result, the following analyses are all based on Model B.

3.10.3 Effects of contact angles at triple junctions on anode stability

A parametric study of three different Ni-YSZ interfacial energies (leading to three different sets of contact angles) is performed using Model B. The three selected scenarios are $\gamma_{\text{Ni-YSZ}} = 1.2 \text{ Jm}^{-2}$, $\gamma_{\text{Ni-YSZ}} = 1.5 \text{ Jm}^{-2}$, and $\gamma_{\text{Ni-YSZ}} = 1.8 \text{ Jm}^{-2}$, which correspond to the contact angles, $\theta_{\text{Ni-YSZ}} = 84^\circ$, $\theta_{\text{Ni-YSZ}} = 93^\circ$, and $\theta_{\text{Ni-YSZ}} = 102^\circ$, respectively. As shown in Fig. 3.10, the general trend of the coarsening behavior remains the same for all parameter sets. However, TPBs stabilize at an earlier time with less reduction when the Ni-YSZ interfacial energy is smaller, which corresponds to a smaller contact angle of Ni on YSZ. Such a case is thus found advantageous to preserve TPBs in the Ni-YSZ anode. This result indicates that there is an opportunity for improving the long-time performance of SOFC anodes by controlling

the surface/interfacial energies of materials. For example, this improvement can be accomplished by doping Ni with additives [123].

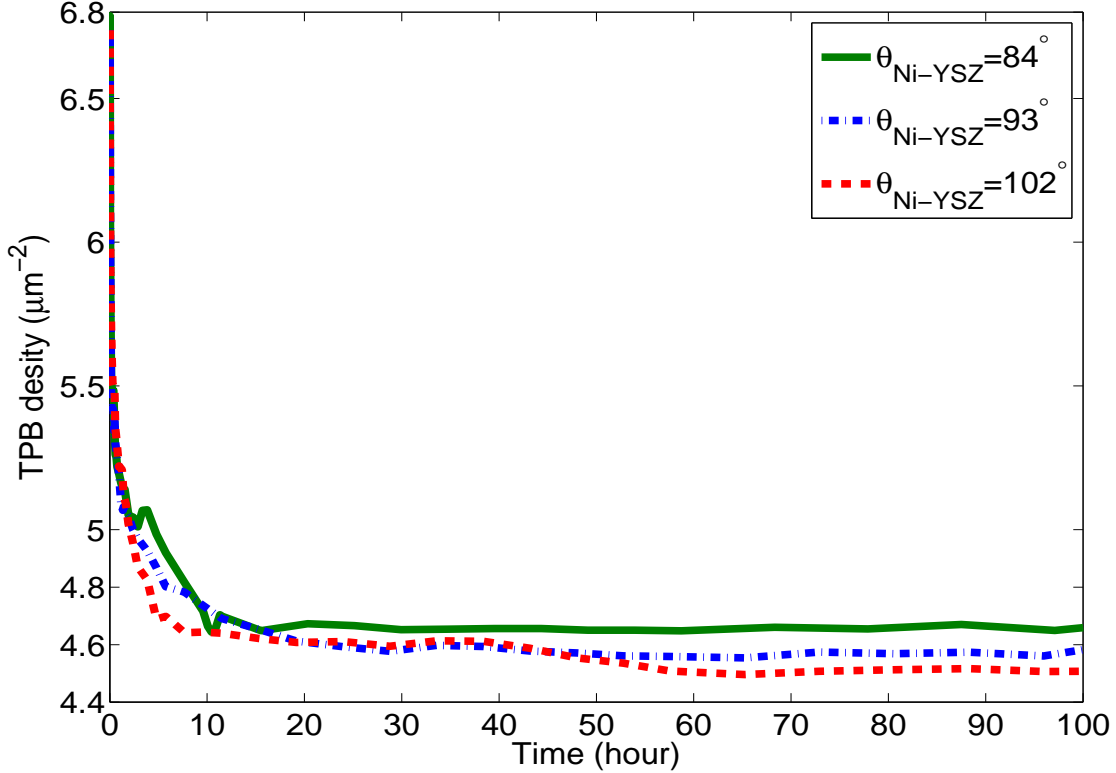


Figure 3.10: Comparison of the TPB reduction among three different Ni-YSZ interfacial energies using Model B.

3.10.4 Phase connectivity and TPB activity

TPB length has been recognized as one of the most important geometric parameter in a three-phase SOFC anode that influences the electrochemical performance. However, how the coarsening of microstructures affects the TPB activity has not been fully explored, partly due to the inability to acquire 3D microstructural information. As previously mentioned, TPBs are active only if they are simultaneously connected to conducting ionic, electronic, and gaseous transport pathways (phases). Therefore, the connectivity evolution of a phase induced by coarsening can alter the activity of

TPBs and the effective conductivity of that phase. In addition, the evolution of the anode microstructure results in changes in the amounts and distributions of TPBs. In turn, coarsening has significant impacts on the overall performance of the electrode.

By simulating coarsening with our models, a series of microstructures are acquired at various stage of evolution. Using the methods described in section 3.9, we can analyze the evolution of the active TPB length based on the evolving TPB structures and phase connectivity during coarsening.

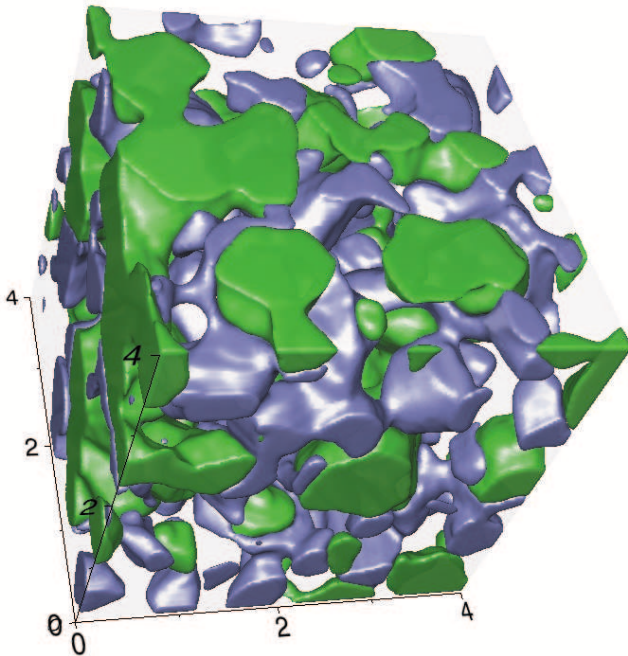


Figure 3.11: Initial Ni-YSZ anode microstructure for a set of larger simulations. The dimensions of the microstructure are $4 \mu\text{m} \times 4 \mu\text{m} \times 4 \mu\text{m}$. The Ni, pore, and YSZ phases are represented in green, blue, and semi-transparent, respectively (with volume fractions 23.8%, 18.7%, and 55.4%, respectively). The initial TPB density is $\sim 5.2 \mu\text{m}^{-2}$.

The initial microstructure of our simulation is based on a 3D restructured SOFC anode of dimensions $9.73 \mu\text{m} \times 8.35 \mu\text{m} \times 11.2 \mu\text{m}$ [3]. We selected a $4.0 \mu\text{m} \times 4.0 \mu\text{m} \times 4.0 \mu\text{m}$ portion of the specimen (Fig. 3.11), resolved by a domain of a $126 \times 126 \times 126$ computational grid. The governing evolution equations are solved using the finite difference algorithm implemented using Open-MP. No-flux boundary

conditions are imposed on the computational domain boundaries to reflect the fact that materials that comprise the SOFC anode is conserved.

In the simulated sample, the volume fractions are 23.8%, 18.7%, and 57.5% for the Ni, pore, and YSZ phases, respectively. Each phase region is categorized as an active, isolated, or dead-end cluster according to the procedure described in Sec. 3.9. By examining the YSZ phase with the aforementioned nearest-neighbor scheme, we find that, in the initial sample, the entire YSZ phase is fully percolated and active within the volume. Using the same procedure, we find that there are 89.1% active, 6.2% isolated, and 4.7% dead-end clusters within the Ni phase, and 94.7% active, 1.9% isolated, and 3.4% dead-end clusters in the pore phase.

Because our 3D microstructure data are represented as a set of voxels with values corresponding to various phases, this categorization procedure seems similar to the problem that consists of identifying the percolating clusters in a finite system on the basis of a simple cubic network with a coordination number of 6. According to the percolation theory, the site percolation of a phase in a simple cubic network is achieved when the volume fraction of that phase is above a threshold value of 0.3116. The YSZ phase in our sample is thus fully percolated and active because its volume fraction is much higher than this threshold value. However, it is surprising that nearly 90% of the volume of the Ni and pore phases are active while their volume fractions are much lower than 0.3116. This finding may be attributed to two reasons. First, the functional layer of our Ni-YSZ anode sample is fabricated by sintering a 50/50wt% NiO-YSZ mixture and exposing it to humidified H_2 to reduce NiO to Ni. This specific fabrication process results in highly percolated pore and Ni phases, even at volume fractions below 0.3116. Second, in our characterization algorithm, a cluster is considered active if it connects any two domain boundaries of the sample volume. Therefore, a cluster with a length scale smaller than the sample dimensions can be active as long as the cluster connects two neighboring domain boundaries

of the sample. In terms of identifying the percolated clusters, this criterion is less stringent than the percolation theory that requires that the cluster is percolated over an infinite volume.

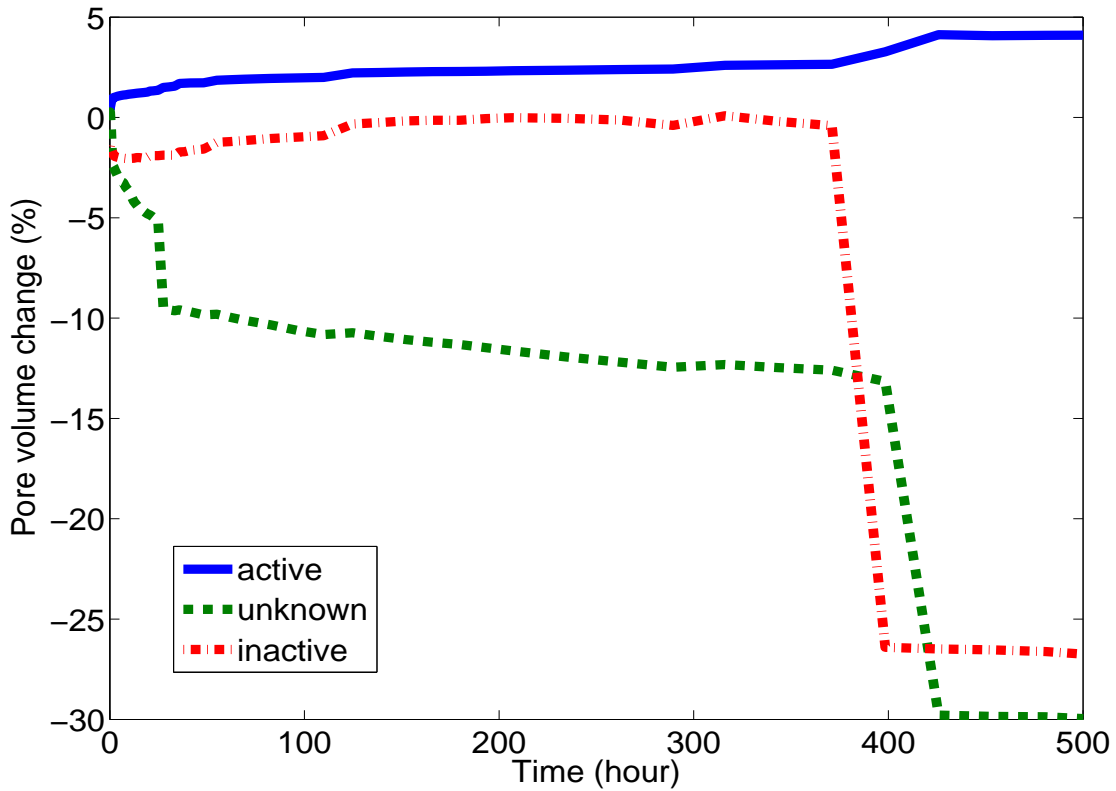


Figure 3.12: The pore volume change in three different categories over 500 hours of coarsening. The change in each category is relative to its initial value.

A crucial question arises is how these phase clusters evolve with coarsening. The coarsening dynamics are greatly simplified in Model B because the Ni surface is the only mobile interface in the system and the YSZ phase is immobile. While coarsening progresses, the system reduces its total energy by reducing mobile regions with high curvatures (which possess smaller length scales and larger surface to volume ratios). Because the Ni and pore phases share the same Ni-pore interface, the mobile surfaces are the same for both phases. The driving force for material transport thus depends on the curvature gradient, which is inversely linked to the characteristic length scale

that is the inverse of the interfacial area per unit volume of the phase (S_V^{-1}). For example, the characteristic length scale of the Ni structure is defined by the volume of Ni divided by the total interfacial area of Ni. Note that this definition of the characteristic length scale is well suited for analyzing multiphase composites with unequal volume fractions because it takes into account the effects of volume on the typical size of a phase domain. For example, if the volume fraction is large, then we expect that the typical size of the domain be larger even if the surface area is the same (this is the case in a two-phase system where that phase is the majority phase). Using this definition, an average Ni length scale 36% larger than the average pore length scale is found in our sample. Inactive pore regions should thus evolve faster and possibly merge with active regions.

According to the simulation results, during the first 500-hr simulation, the Ni volume fractions in each category and the mean Ni length scale remain roughly constant. In contrast, as shown in Fig. 3.12, the dead-end and isolated pore volumes decrease significantly, which confirms the faster evolution of regions associated with smaller length scales during coarsening. Interestingly, the active-pore volume increases in our simulation due to the fact that the smaller isolated and dead-end clusters merge into the larger pore clusters, that are most likely in the active cluster category. One interesting observation is that even though clusters with higher curvatures possess higher free energy than those with lower curvatures, they may be trapped in a local equilibrium state because the transport pathway is confined to the Ni-pore interface. This kinetic constraint explains why the isolated and dead-end clusters in the pore phase did not suffer major loss of volume after 500 hours of coarsening.

The evolution of TPBs is correlated with the evolution of the phases that comprise the SOFC anode. The material transport among different clusters of each constituting phases not only changes the distribution of the TPBs but also dictates their activity. As shown in Fig. 3.13, the reduction trend of the active TPB density agrees well

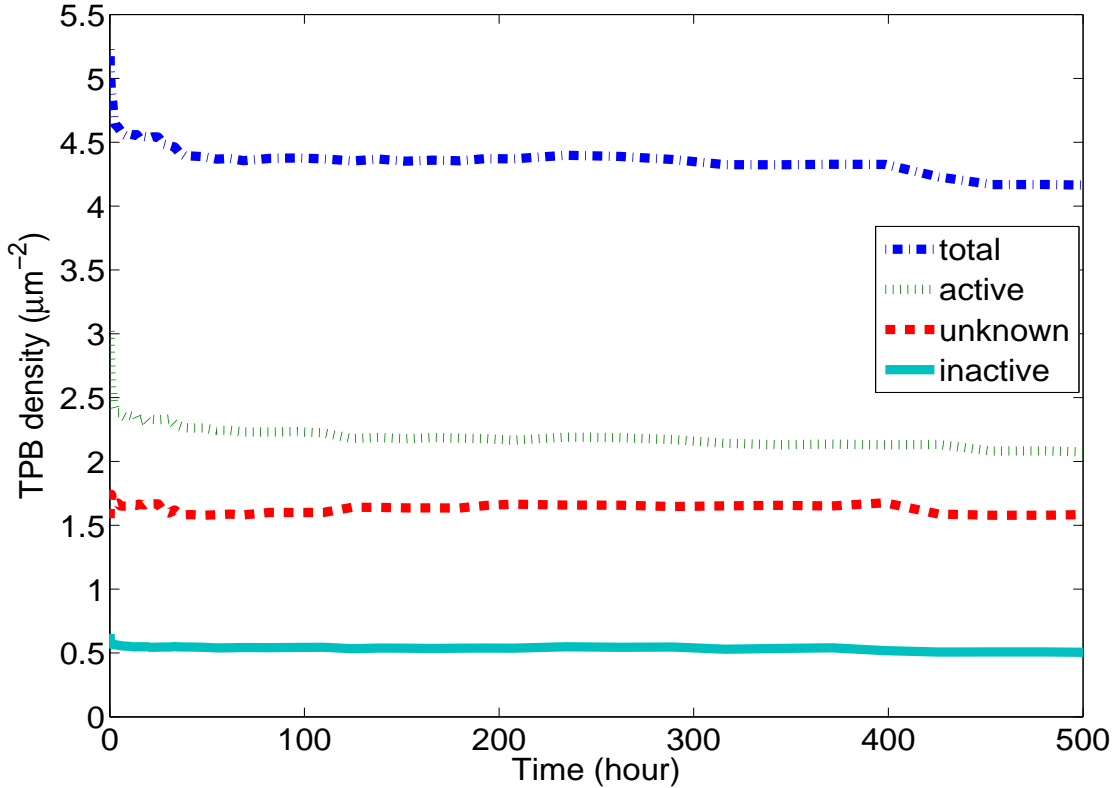


Figure 3.13: TPB density change in each category over 500 hours of coarsening. The active TPB length reduction is $\sim 89\%$ of the total TPB reduction after 500 hours.

with the total TPB density. The overall TPB density decreased by 20.2% after a 500-hour coarsening, while the active and isolated TPB density decreased by 31.4% and 22.3%, respectively. In contrast, the unknown TPB density slightly increased by 1.6%. Most of the TPB density reduction comes from the 31.4% decrease in the active TPBs. At the early stage of coarsening, the rapid reduction of active TPBs is due to the local coarsening of high-curvature microstructural features. The small increase in the unknown TPBs observed in the early stage of evolution stems from coalescence of inactive Ni domains, which occurs rarely. Since the evolution of TPBs is sensitive to local microstructural features, it is only indirectly correlated to the coarsening kinetics.

To summarize, our findings indicate that the coarsening of a Ni-YSZ anode con-

sumes the mobile phase clusters with high curvatures. The isolated and dead-end pore clusters are thus the first clusters that evolve, leading to coarsening of the pore phase, which is indicated by the change of $S_{V(pore)}^{-1} = 0.1105 \mu\text{m}$ to $S_{V(pore)}^{-1} = 0.1154 \mu\text{m}$, i.e., a 4.4% increase over 500 hours. While the Ni phase has the same mobile area as the pore phase, its mean characteristic length scale, which is defined by $S_{V(Ni)}^{-1}$, is significantly larger than that of the pore phase and results in a slower evolution. In addition, the Ni-pore area reduction is found to be balanced by the increase of the Ni-YSZ interfacial area. The coarsening has thus no significant effect on the mean length scale of Ni, which varies from $S_{V(Ni)}^{-1} = 0.1711 \mu\text{m}$ to $S_{V(Ni)}^{-1} = 0.1719 \mu\text{m}$ (which corresponds to a 0.5% change during the course of our simulation. In turn, the coarsening leads to a significant reduction in TPBs and the active TPB sites decreases in a very similar fashion as the overall TPBs. However, the TPB evolution is sensitive to microstructural details and is only weakly linked to the evolution of the bulk phases during coarsening.

3.10.5 Tortuosity of pores

Tortuosity represents the geometric aspect of the transport property of a phase that comprises a composite. Therefore, the tortuosity of the pore phase plays a crucial role in the generation of electricity because the fuels need to be transported through the pores to reach the reaction sites. The tortuosity factors of the pore phase are evaluated in three orthogonal directions over a 500-hr coarsening period. As shown in Fig. 3.14, although the absolute values differ, the tortuosity factors decrease moderately in all directions during coarsening. This trend is consistent with the fact that the active pore volume increases slightly during coarsening (see Sec. 3.10.4, Fig. 3.12). These results indicate a coalescence of pore clusters and a lack of breakup of active clusters, which lead to somewhat enhanced transport properties.

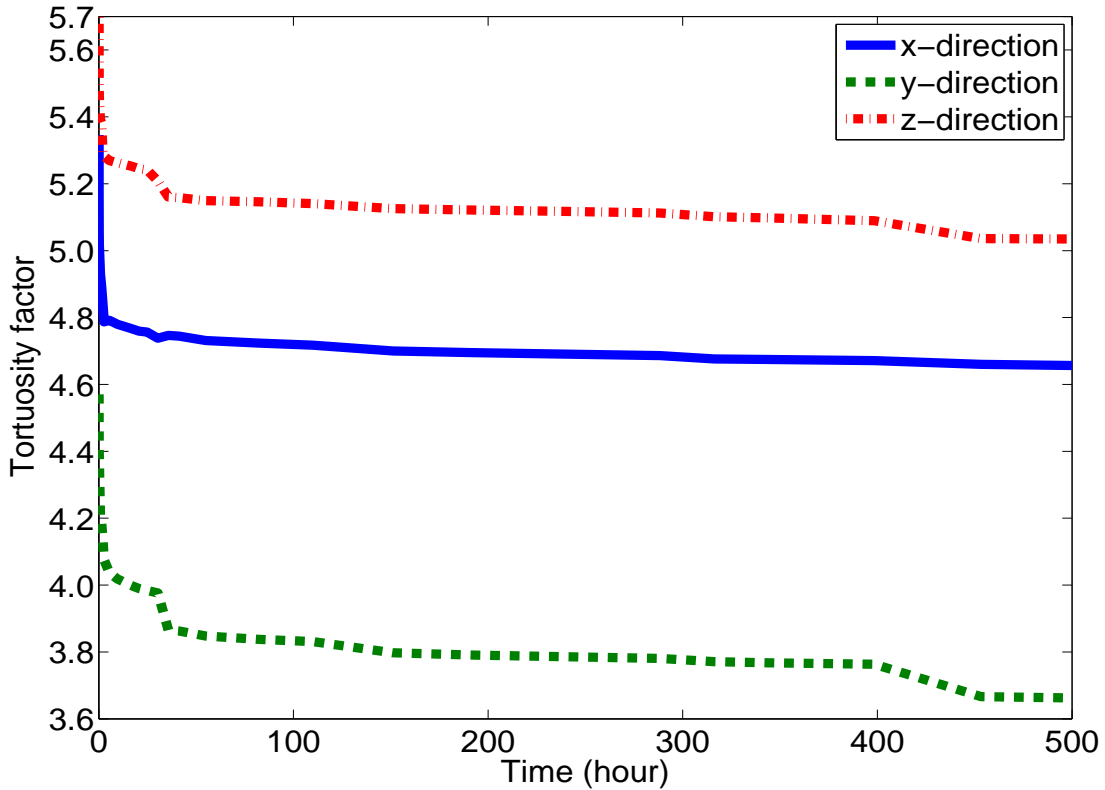


Figure 3.14: Tortuosity factors in three orthogonal directions of the pore phase over 500 hours of coarsening.

3.10.6 The active Ni surface

One advantage of SOFCs is their ability to operate with hydrocarbon fuels as well as hydrogen. This is because hydrocarbon fuels can be internally reformed to hydrogen with the catalytic effect of Ni at the typical operating temperatures of SOFCs. This reforming rate is highly related to the active Ni surface area. Depending on the fuel, the reforming kinetics can be very different and involve multiple elementary reaction steps; however, the reforming reactions of all types of fuels involve gas species and electron transfer, regardless of the detailed reforming mechanisms. Therefore, the active Ni surface for hydrocarbon reforming must reside at the interface of active pore clusters and active Ni clusters.

To evaluate the catalytic performance of the Ni phase in SOFC anodes, an im-

portant question to ask is how coarsening affects the active Ni surface area. The evolution of an active Ni surface area is dictated by the evolution of active clusters of Ni and pore phases. The active Ni surface is identified as the interfaces between active Ni and active pore clusters. As shown in Fig. 3.15, the active Ni surface decrease by 9% after 500-hr coarsening, while the total Ni-pore interface decrease by 13.6%. Our finding indicates that coarsening reduces more inactive Ni surfaces than those in contact with the active clusters of Ni and pore. This is due to the fact that smaller clusters, which have smaller length scales and thus have larger driving force toward coarsening, coarsen faster than the larger ones.

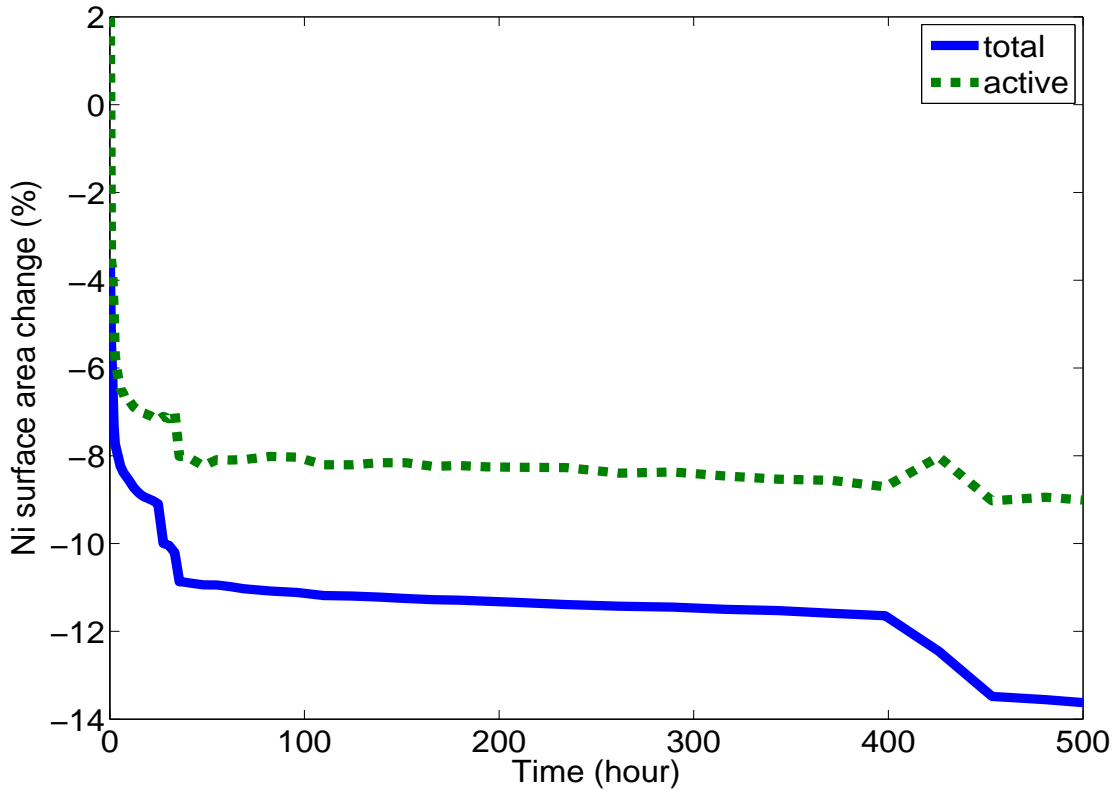


Figure 3.15: Ni surface area reduction over 500 hours of coarsening.

3.10.7 Size effects and evolution kinetics

We next simulate coarsening in Ni-YSZ anode samples of different sizes, namely, $(3.2 \mu\text{m})^3$, $(4.0 \mu\text{m})^3$, and $(4.8 \mu\text{m})^3$, to examine the size effects. Each of these samples is acquired from a portion of the original $914.55 \mu\text{m}^3$ sample. Specifically, the sample of dimensions $(3.2 \mu\text{m})^3$ is cropped from the sample of dimensions $(4.8 \mu\text{m})^3$, while the sample of dimensions $(4.0 \mu\text{m})^3$ belongs to a different portion of the original sample.

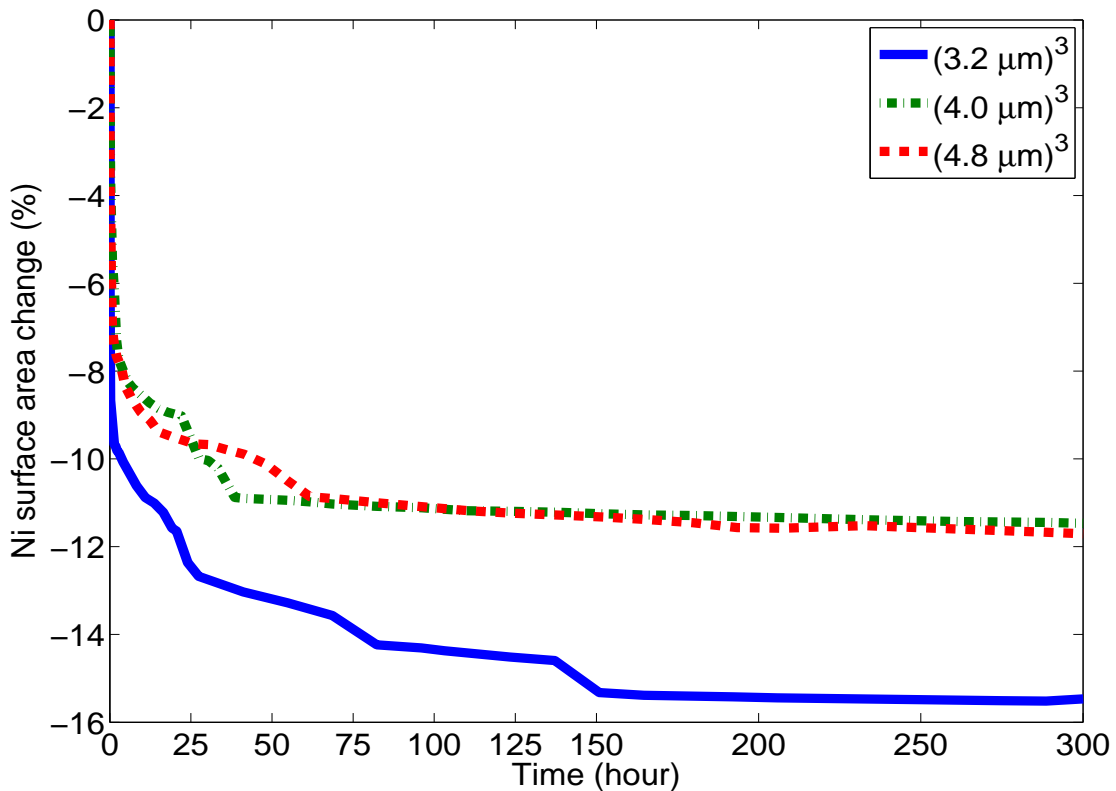


Figure 3.16: Reduction of the Ni surface areas for three different sample sizes over 300 hours of coarsening.

The Ni surface areas and the TPB lengths are compared over the first 300 hours of the coarsening period. The evolution kinetics can be best interpreted from the evolution of the Ni surface area in our Model B simulations. As shown in Figs. 3.16 and 3.17, the Ni surface area reduction rate of the $(4.0 \mu\text{m})^3$ and the $(4.8 \mu\text{m})^3$

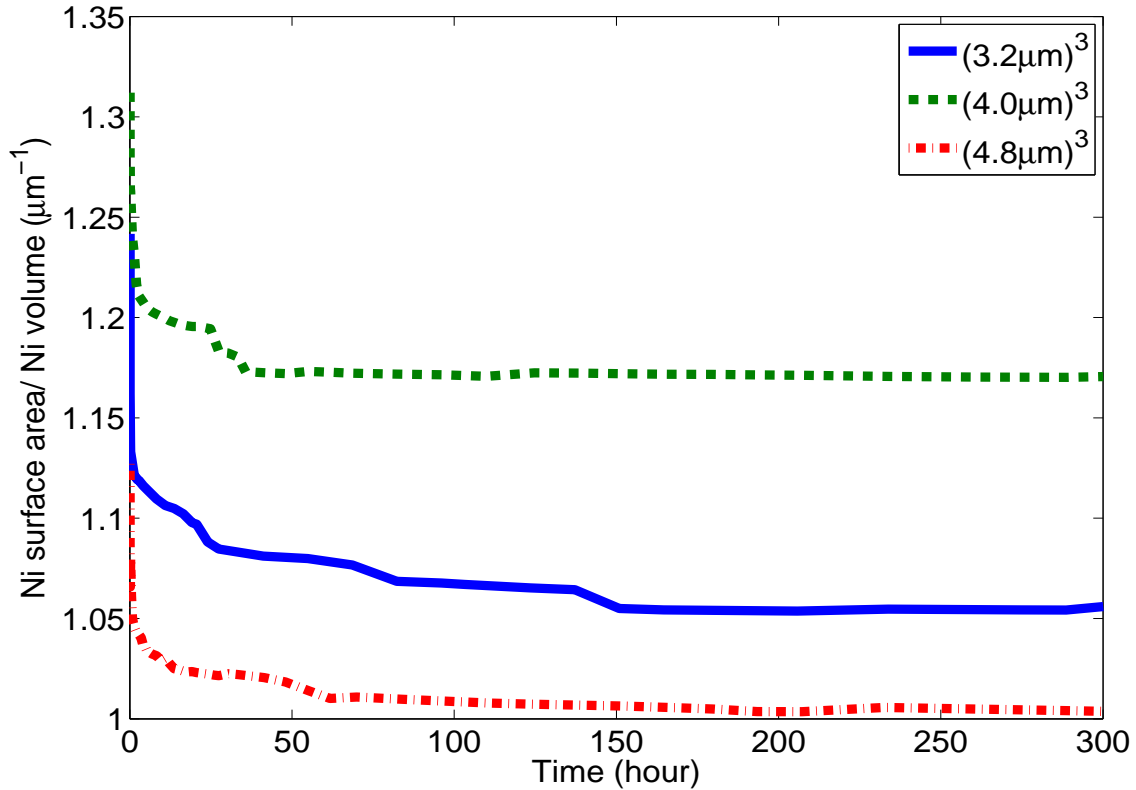


Figure 3.17: Reduction of the Ni surface area per Ni volume for three different sample sizes over 300 hours of coarsening.

specimen are very similar, while the reduction rate of the $(3.2 \mu\text{m})^3$ specimen deviates from the other two significantly even though the specimen is a portion of the $(4.8 \mu\text{m})^3$ sample. In addition, some reduction steps appear in the $(3.2 \mu\text{m})^3$ curve whereas the other two curves are relatively smooth. This suggests that the two larger sample sizes may be sufficient to eliminate the boundary effects from the simulations, while smaller volumes would likely suffer from them and may not contain enough particles or statistics for coarsening simulations.

As shown in Fig. 3.18, the change of the TPB densities of the three specimens are compared over 300-hr coarsening. Although the behavior of the TPBs is only indirectly related to the evolution kinetics, we find similar trend in the TPB evolution among the three specimens as those found in the Ni surface area. Although the TPB

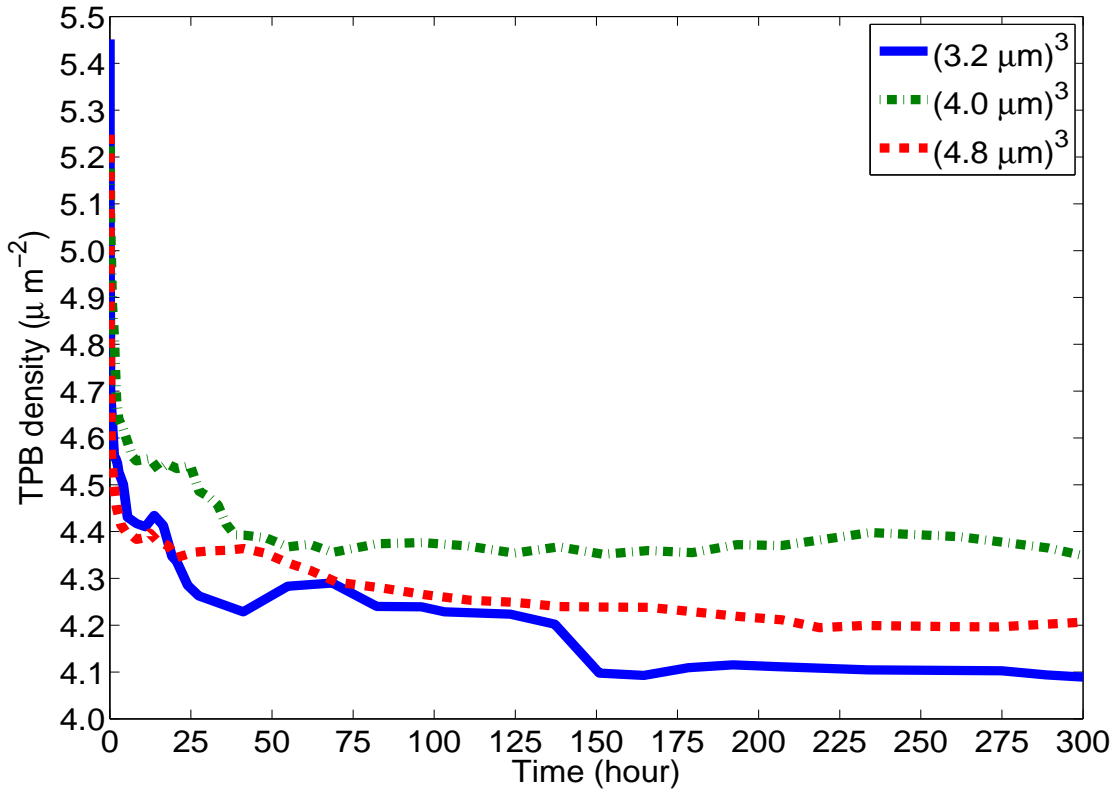


Figure 3.18: TPB densities for three different sample sizes over 500 hours of coarsening. The initial TPB densities of the $(3.2 \mu\text{m})^3$, $(4 \mu\text{m})^3$, and the $(4.8 \mu\text{m})^3$ samples are $5.45 \mu\text{m}^{-2}$, $5.22 \mu\text{m}^{-2}$, and $5.25 \mu\text{m}^{-2}$, respectively.

density reduction kinetics are different, after 300-hour coarsening, the difference of the TPB densities between the two larger samples is less than 3%. Since TPB evolution is more sensitive to microstructures, this difference may serve as the indication of the local variation due to microstructural details. Thus, in order to determine whether the two larger sample volumes are sufficient to represent the microstructure of the anode, we would need to simulate a larger sample volume.

Although rapid reductions of TPBs and the Ni surface area at early stages of coarsening is a result of the large thermodynamic driving force for mass transport, which mostly results from regions with high curvatures, the overly steep slopes in Figs. 3.16 and 3.18 deserve further investigations.

To examine the length scales involved in the microstructures, the mean curvature and the interfacial shape distribution (ISD) of the Ni interfaces in the $(4 \mu\text{m})^3$ specimen are plotted in Fig. 3.19 (a) and (b), respectively. Due to the diffuse interface nature of our models and the model parameters we utilized in our simulations (based on the resolution that made simulations feasible), very small microstructural features with absolute principal curvature values larger than 0.17 (which accounts for approximately 30% of the Ni interfacial area) are not fully resolved. As shown in Fig. 3.19 (c) and (d), if those numerically under-resolved regions are mobile, they will be smoothed out very rapidly, leading to coarsening that is faster than expected.

This numerical smoothing due to under-resolution contributes in part to the rapid evolution in the early stage of coarsening simulations and leads to an overestimation of the TPB reduction rate. However, these mobile, high-curvature regions inherently possess very large thermodynamic driving force and will coarsen sooner or later. Therefore, even though the rapid evolution at the early stage of simulations may be caused by the insufficient resolution of microstructures, the stabilized value of TPB density after further coarsening remains unaffected by it. That is, the prediction of the stabilization of TPBs, as well as its predicted value, remains robust, even though the early kinetics may be overestimated. Since the microstructures of Ni-YSZ anodes are found to stabilize after coarsening for a period of time, the final or stabilized TPB density rather than the short-term evolution kinetics is of importance for the operation of SOFCs.

3.11 Conclusion

We developed two models to study the coarsening kinetics in the Ni-YSZ anode. An asymptotic analysis was conducted to link our simulation results to the physical system. The size effects were studied and an error analysis was performed to validate our models. For the model parameters selected, no obvious boundary effects were ob-

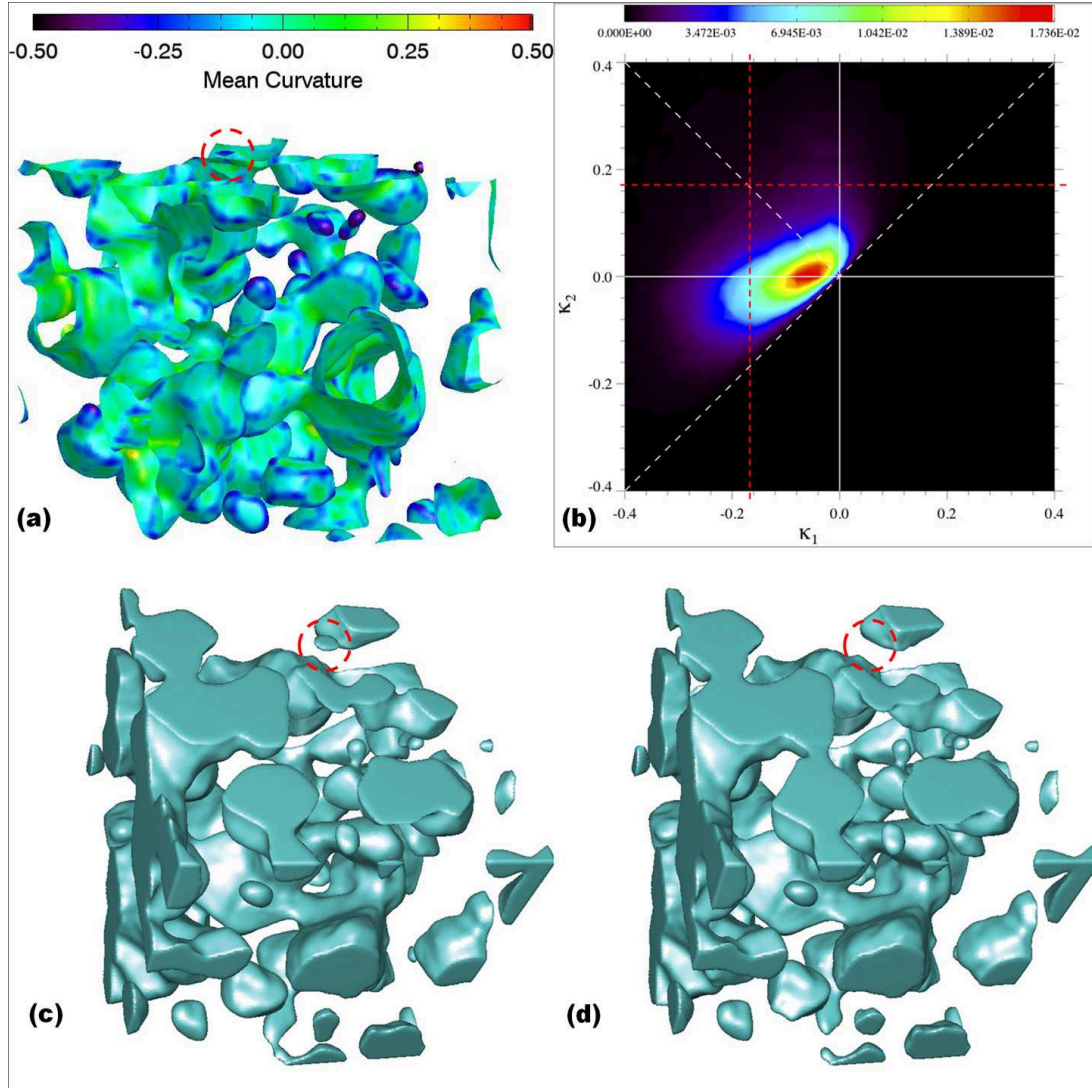


Figure 3.19: Numerical smoothing of Ni microstructures in Model B. The circled particle is numerically smoothed after a very short time of coarsening. (a) mean-curvature ($H = (\kappa_1 + \kappa_2)/2$) plot of Ni interfaces; (b) ISD diagram of Ni interfaces; (c) the Ni microstructure before coarsening; (d) Ni microstructure after coarsening for 3 minutes. (Figures (a) and (b) were plotted by Chal Park in Thornton's group.)

served when the simulated domain was larger than $(4 \mu\text{m})^3$, even though the sample size was still insufficient to be statistically representative of the entire microstructure at this volume. In addition, the use of the selected mesh resolution had very minor effects on the quasi-equilibrium contact angles and evolution kinetics. While the short-term evolution kinetics may be affected by the insufficient resolution of mi-

crostructures, the amount of TPBs and other properties after long-term coarsening can be identified by our simulations.

Although our models contain approximations and the simulation results may be affected by uncertainties in the material properties, a reasonable agreement could be found for the TPB length evolution between coarsening experiments and simulation results using Model B. Unlike Model B, Model A overestimates the TPB reduction due to the evolution of the YSZ structure that is induced by an excess mobility at triple junctions built into the model. Our simulations show that the major portion of TPB reduction occurs during the early stages of coarsening and that stability of TPBs is observed provided that YSZ is nearly immobile. Furthermore, we have demonstrated that a smaller Ni-YSZ interfacial energy can enhance the stability of the TPB density. A more robust anode against coarsening can thus be fabricated by alloying to form a metallic phase or doping the Ni phase.

The evolution of active TPBs, active Ni surface areas, and tortuosity of the pore phase are investigated in our simulations. We found that coarsening has a smaller impact on the active Ni surface areas than on their total respective amounts. In addition, the tortuosity of the pore phase was found to decrease slowly in all three orthogonal directions during coarsening. These phenomena are due to the fact that percolated phase clusters that dictate the active parameters and transport have typically larger characteristic length scales than isolated/dead-end phase clusters. Smaller clusters experience larger driving forces for coarsening, while larger clusters may grow at the expense of these regions if transport can be facilitated between them. Active Ni surface areas are also less reduced than their dead/isolated counterparts, and the transport property of the pore phase is slightly enhanced. In contrast, the reduction of active TPBs are found to account for most of the total TPBs reduction, which suggests that the TPB evolution is sensitive to microstructural details and is indirectly related to the evolution of bulk phases during coarsening.

The proposed coarsening models provide insights into directing the design of anode microstructures. The model framework is general and can be applied to many other three-phase coarsening systems. Further experiments can help validate and improve these models.

CHAPTER IV

Simulation of Oxygen Ion Transport in Mixed-Conducting SOFC Cathodes

The previous chapter discussed the modeling of the Ni coarsening phenomenon in a Ni-YSZ anode. In this chapter, the focus shifts to the electrochemical modeling of oxygen ion transport in a mixed conducting cathode.

4.1 Nonstoichiometric thermodynamics of mixed conducting perovskites

Operating SOFCs in the intermediate temperature (IT) range is advantageous for rapid start-up, slow degradation, and cost-effective fabrication. However, due to the sluggish nature of oxygen reduction reactions, lower operation temperatures lead to even slower oxygen reduction kinetics at cathodes, which is considered to be the major obstacle for advances in IT-SOFCs. Because the cathode contributes a substantial polarization resistance, improving the cathode performance is the key to bringing the SOFCs to intermediate operating temperatures.

The basic function of a porous SOFC cathode is to reduce the oxygen to oxygen ions and transport these ions to the electrolyte. The oxygen reduction reaction can be explained with a half-cell reaction:



This reaction involves three species: the oxygen gas, oxygen ions and electrons. In traditional porous SOFC cathodes comprised of pure electronic-conducting materials, such as $\text{La}_x\text{Sr}_{1-x}\text{MnO}_{3-\delta}$ (LSM), the oxygen reduction reaction, Eq. 4.1, is limited to regions near three-phase boundaries, where the pores, electronic- and ionic- conducting phases are simultaneously in contact due to the poor ionic conductivity of LSM. On the other hand, at elevated temperatures (in the range of IT-SOFC), many of the transition metal perovskite-type oxides (ABO_3 , Fig. 4.1) present increased oxygen vacancies with high mobility. Together with the high electronic conductivity promoted by their perovskite structure, these oxides including $\text{La}_x\text{Sr}_{1-x}\text{CoO}_{3-\delta}$ (LSC) are of interest for IT-SOFC cathodes and other applications.

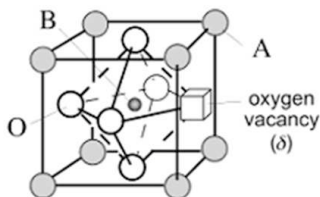


Figure 4.1: Basic atomic structural element of ABO_3 , which consists of a BO_6 octahedron surrounded by charge-compensating A-site cations [6].

The most desirable property of these transition metal perovskite oxides is their ability to accommodate oxygen vacancies, while preserving the lattice structure. In LSC, oxygen-vacancy formation stems from the cation dopant Sr^{2+} , which substitutes for some of the La^{3+} at A sites. This valence change is partially balanced by the formation of oxygen vacancies throughout the bulk of the material. The mixed-conducting LSC cathode can therefore catalyze the oxygen reduction at the solid-pore interface, which is two-dimensional rather than one-dimensional, as in LSM cathodes. This enhancement, however, allows multiple reaction paths, which complicates the picture of oxygen exchange mechanisms [6].

In order to further understand the thermodynamic properties and nonstoichiometric behavior of mixed-conducting oxides, such as LSC, Lankhorst et al. [14] utilized coulometric titration cells to measure the formation of oxygen vacancies. In their coulometric titration experiment, the difference of oxygen chemical potential between the oxide sample and the reference gas ($\Delta\mu_{O_2}$) was evaluated from the electromotive force (EMF), whereas the nonstoichiometry variation of the oxide ($\Delta\delta$) was determined by the integration of the current over time in response to the change of the oxygen partial pressure surrounding the cell ($P_{O_2}^{cell}$) [15]. Based on these experimental results, Lankhorst developed a framework for the nonstoichiometric thermodynamics of transition metal oxides with mixed-conducting properties. Because this framework is applicable to many mixed-conducting oxides, we summarize in the following discussion some of their key results that are relevant to our electrochemical modeling work.

The oxygen reduces to oxygen ions within the mixed conducting oxides, which can be represented with the following equation in Kröger-Vink notation:



Because the oxide and surrounding gas are in chemical contact, the oxygen incorporation reaction, Eq. 4.2, can be used to connect the chemical potential of the involved species. Assuming that this oxygen incorporation reaction reaches equilibrium, the Gibbs free energy of reaction $\Delta_{rxn}G$ equals zero, which yields

$$\Delta_{rxn}G = 0 = 2(\mu_{O_{\text{O}}^x} - \mu_{V_{\text{O}}^{\cdot\cdot}}) - 4\mu_{e^-} - \mu_{O_2}, \quad (4.3)$$

where μ_i denotes the chemical potential of species i . Assuming that the oxygen vacancies $V_{\text{O}}^{\cdot\cdot}$ and lattice oxygen ions O_{O}^x are sufficiently dilute so that they do not

interact, the chemical potential of the oxygen vacancy building unit,

$$\mu_{\{V_{\ddot{O}}\}} = \mu_{O_{\ddot{O}}^x} - \mu_{V_{\ddot{O}}} = \mu_{\{V_{\ddot{O}}\}}^0 + RT \ln C_0 \frac{\delta}{3 - \delta} = \mu_{\{V_{\ddot{O}}\}}^0 + RT \ln(C_0 x_v), \quad (4.4)$$

where δ is the nonstoichiometry parameter, which measures the deviation of the oxygen fraction from the stoichiometry of the oxide; $x_v = \delta/(3 - \delta) \sim \delta/3$ is the mole fraction of the bulk oxygen lattice sites occupied by a vacancy; C_0 is the molar concentration of oxygen lattice sites; R is the universal gas constant; and T is the temperature. The chemical potential of the oxygen gas can be written as

$$\mu_{O_2^{gas}} = \mu_{O_2^{gas}}^0 + RT \ln P_{O_2}. \quad (4.5)$$

The electron chemical potential of transition-metal perovskite oxides, such as LSC, depends on whether the electrons created by vacancy formation are free to wander around (charge-transfer type) or are localized near the lattice sites (charge-disproportionation type) [133, 134]. LSC has been shown to be metallic in nature with a broad electron band and to belong to the charge-transfer type. As a result, the number of available electron states near the Fermi level of LSC is limited, and the entropy contribution in the electron chemical potential is negligible. Therefore, the electron chemical potential of these delocalized electrons, or Fermi level, in the partially filled band is approximately equal to the energy of the highest occupied electron state. Lankhorst derived an approximation of the electron chemical potential in partially filled bands using the electron-gas rigid band model (RBM), which assumes that the electron band does not shift when oxygen ions are removed from the solid, as

$$\mu_e = \mu_e(n^0) + N_A \frac{n - n^0}{g(\mu_e(n^0))}, \quad (4.6)$$

where n^0 is the electron occupation number at which no itinerant electron is in the

considered partially filled band, n is the electron occupation number, N_A is Avogadro's number, and $g(\mu_e(n^0))$ is the density of state at the Fermi level. This equation indicates that the Fermi level shifts upward in response to the addition of electrons into the band. Because the itinerant electrons in LSC are created by the vacancy formation induced by Sr dopant, and are donated to the partially filled band, electroneutrality demands

$$n - n^0 = 2\delta - x. \quad (4.7)$$

By substituting Eqs. 4.3, 4.5, and 4.6 into Eq. 4.3, the nonstoichiometry parameter of the oxide (δ) is related to the oxygen partial pressure of the surrounding gas through

$$\mu_{O_2}^{0gas} + RT \ln P_{O_2} = (-4\mu_e(n^0) + 2\mu_{\{V_{\ddot{O}}\}}^0) - 4N_A \frac{2\delta - x}{g(\mu_e(n^0))} + 2RT \ln C_0 \frac{\delta}{3 - \delta}. \quad (4.8)$$

Rearranging Eq. 4.8, the defect thermodynamics in LSC are derived as

$$RT \ln P_{O_2} = \Delta_{rxn} G^0 - 4N_A \frac{2\delta - x}{g(\mu_e(n^0))} + 2RT \ln C_0 \frac{\delta}{3 - \delta}, \quad (4.9)$$

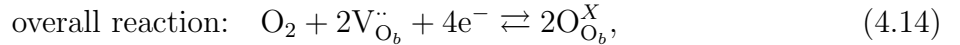
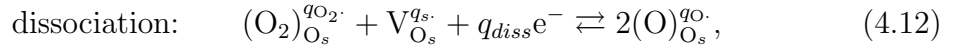
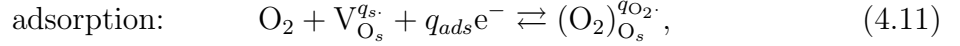
where $\Delta_{rxn} G^0 = 2\mu_{\{V_{\ddot{O}}\}}^0 - 4\mu_e(n^0) - \mu_{O_2}^{0gas}$ is the Gibbs free energy of the oxygen incorporation reaction at a reference state. Both $\Delta_{rxn} G^0$ and $g(\mu_e(n^0))$ can be measured from the coulometric titration experiments by varying the oxygen partial pressure and temperature.

Thermodynamics also affects the kinetics through the thermodynamic factor that appears in the diffusion coefficient. The thermodynamic factor, A , is the partial derivative of the chemical potential with respect to the concentration, which can be acquired by taking the derivative of Eq. 4.9 with respect to the lattice nonstoichiometry $\ln \delta$:

$$A = -\frac{1}{2} \frac{\partial \ln P_{O_2}}{\partial \ln \delta} = 1 + \frac{4\delta}{k_B T g(\mu_e(n^0))}. \quad (4.10)$$

4.2 Surface reaction mechanisms in LSC

Although no consensus has emerged regarding the mechanisms governing the exchange of oxygen with the bulk at gas-exposed surfaces in mixed conducting perovskites, a thermodynamically consistent framework for predicting oxygen reduction rate laws has been proposed by Adler et al. [16]. This framework is based on four assumptions: (1) the adsorption of O_2 requires a vacant surface site $V_{O_s}^{q_s}$ and the dissociation requires a second vacant surface site; (2) oxygen ions on the surface have a fixed oxidation state determined by their bonding configuration; (3) the reaction is limited by a specific rate-determining step; and (4) a neutral building-unit convention is adopted due to the electroneutrality and site conservation. The surface-bulk oxygen exchange reaction can then be described by three elementary steps [16]:



where the primary symbols O_2 , V , and O represent diatomic oxygen, oxygen vacancies and oxygen atoms, respectively. The subscript O_s and O_b indicate the species location at a surface or bulk oxygen site. The superscripts show the charge of species. The charge balance requirement imposes the condition $q_{ads} + q_{diss} + 2q_{incorp} = 4$.

Based on transition state theory, a general mass action law for a reaction that involves both entropic and energetic contributions to the free energy can be written as [16]

$$r_j = \mathfrak{R}_0[1 - e^{-\Lambda_j/RT}], \quad (4.15)$$

where Λ_j is the thermodynamic driving force for the reaction, and the coefficient \mathfrak{R}_0 depends on the activity of the involved species in the reaction, as well as the energetic shifts in the free energy due to the applied driving force. For example, to derive the oxygen reduction rate law for LSC, the nonstoichiometry thermodynamics framework discussed in Sec. 4.1 can be applied because LSC is metallic in nature. If the overall reduction reaction Eq. 4.14 is considered rather than the individual elementary reactions, the thermodynamic driving force Λ in Eq. 4.15 is simply the Gibbs free energy of reaction ΔG_{rxn} defined in Eq. 4.3. Thus, Λ can be derived as

$$\Lambda = RT \ln \left(\frac{C_0^2 x_v^2}{P_{O_2}} \right) + \Delta_{rxn} G^0 - 4N_A \frac{6x_v - x}{g(\mu_e(n^0))}. \quad (4.16)$$

For convenience, we may define the oxygen fugacity in the solid $f_{O_2}^{solid}$ as the effective pressure P_{O_2} that is in equilibrium with the solid at composition x_v , which can be expressed as a simplified reaction



If we further assume that, at the reference state (for example, room temperature and ambient pressure), the chemical potential of oxygen gas $\mu_{O_2, gas}^0$ and that of the oxygen in the oxide $\mu_{O_2, solid}^0$ are equal. The thermodynamic driving force Λ in the rate law Eq. 4.15 for Eq. 4.17 is

$$\Lambda = \Delta_{rxn} G = \mu_{O_2, solid}^0 - \mu_{O_2, gas}^0 + RT \ln \left(\frac{f_{O_2}^{solid}}{P_{O_2}^{gas}} \right) = RT \ln \left(\frac{f_{O_2}^{solid}}{P_{O_2}^{gas}} \right). \quad (4.18)$$

Comparing Eq. 4.16 and Eq. 4.18, the fugacity, an effective pressure, $f_{O_2}^{solid}$ is linked to the bulk vacancy fraction x_v as

$$f_{O_2}^{solid} = C_0^2 x_v^2 e^{(\Delta_{rxn} G^0 - N_A(24x_v - 4x)/g(\mu_e(n^0)))/RT} \quad (4.19)$$

If one of the three intermediate steps (Eqs. 4.11, 4.12, and 4.13) is identified as rate limiting, the reaction kinetics can be significantly simplified because the other two reactions are quasi-equilibrated. In such a case, the rate prefix \mathfrak{R}_0 and the driving force Λ_j in Eq. 4.15 has to be adjusted accordingly, the details of such a correction are provided in Ref. [16].

4.3 Model framework of oxygen reduction and transport in LSC

Electrochemical impedance spectroscopy (EIS) has been one of the most fruitful experimental techniques for studying solid-state ionic materials. Using EIS with thin film materials or patterned electrodes can provide valuable insight into the reaction mechanisms. However, an EIS measurement alone is not well-suited for isolating or identifying individual reaction and transport mechanisms because their interplay can be complex and multiple transport-reaction paths can lead to similar spectra. A unique interpretation of one individual impedance spectrum is thus usually extremely difficult. Impedance spectra can appear to be similar even when different mechanisms (such as bulk diffusion, surface diffusion, or surface reaction) are dominant, especially when the microstructural effects are unknown.

One plausible usage of EIS is to combine the results of kinetic measurements with the rate law of a certain mechanism. By examining a wide range of experimental conditions, such as various temperatures and pressures, a particular mechanism can be eliminated if the measured impedance characteristics are inconsistent with the expected response corresponding to that mechanism. This process of elimination is usually performed in combination with electrochemical models with parameters obtained from EIS measurements. Modeling is therefore an important tool to aid the interpretation of these kinetic studies.

An oxygen exchange model for transition-metal mixed-conducting oxides was developed by Adler et al. (hereafter referred to as the ALS model) [18], which is a one-dimensional macrohomogeneous model that considers only bulk diffusion and surface reactions (hereafter written as the bulk path for short). Although the ALS model succeeded in explaining the impedance features of mixed conductors with a high ionic transport property, the quantitative validity of this model has been debated because it did not consider the surface diffusion. A further weakness is that, due to the macrohomogeneous assumption, the ALS model applies only when the utilization length of the electrode is significantly larger than the characteristic length of the microstructures.

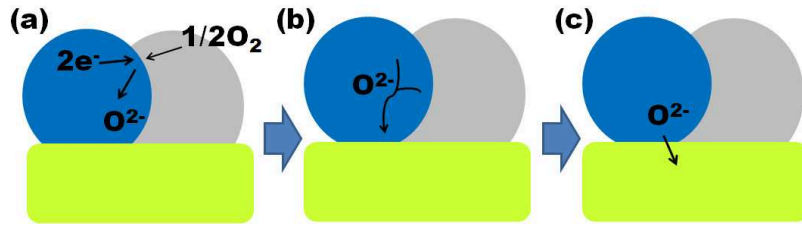


Figure 4.2: The bulk path for oxygen transport following a surface reaction mixed conducting oxides. The blue color represents the oxide, grey shows the gas phase, and green indicates the electrolyte. The oxygen is completely reduced to oxygen ions on the oxide surface (a) then transported through the bulk (b) to the electrolyte (c).

Recently, a dual-path three-dimensional model that considers both bulk and surface transport as well as the surface reaction was developed by Lu et al. [19]. In addition to the commonly recognized bulk path (Fig. 4.2), the model proposed that the surface path (Fig. 4.3) can play an important role in the oxygen exchange in mixed-conducting oxides. Based on the EIS measurements over a range of temperatures and oxygen partial pressures, this model was utilized to study the oxygen exchange mechanisms in LSC with strontium-dopant composition $x = 0.4$ (LSC-64) and $x = 0.2$ (LSC-82). For LSC-64, the impedance features were quantitatively explained with the model under the assumption that only bulk diffusion dominates.

For LSC-82, the existence of a surface diffusion path mediated by an interstitial or adatom mechanism was suggested [19].

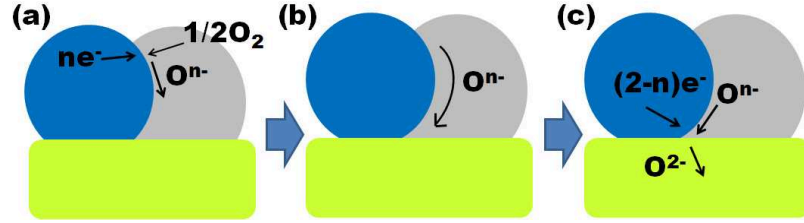


Figure 4.3: The surface path for oxygen transport in mixed-conducting oxides. The blue color represents the oxide, grey illustrates the gas phase, and green shows the electrolyte. The oxygen is partially reduced to intermediate species on the oxide surface (a), then transport on the surface (b), and subsequently fully reduced to oxygen ions before entering the electrolyte (c).

Despite the improvement offered by the dual-path model, the analysis in Ref. [19] was based on a simplified geometry of cylindrical rods with geometric parameters, such as the surface area per unit volume, that were calculated to match experimental measurements. Although this idealized geometry is considered to be equivalent to the experimental microstructure in terms of the matched geometrical parameters, the effects of the details of the microstructure on oxygen-reduction reaction and transport are potentially significant in some operating or EIS measurement conditions and may not be captured by the simplified geometry. Thus, we implement this model with a smoothed boundary method to facilitate the investigation of microstructural effects in experimentally obtained 3D microstructures. The framework of the electrochemical model in Ref. [19] is briefly reviewed in the following discussion.

Some assumptions are made in the model: (1) the LSC phase is assumed to be fully interconnected and to have infinitely high electronic conductivity, but finite bulk oxygen vacancy diffusivity; (2) the gas surrounding the LSC cathode is assumed to consist of uniform oxygen partial pressure P_{O_2} ; (3) a generalized rate law (Eq. 4.15) is assumed for the oxygen reduction reaction in LSC cathode; (4) a quasi-equilibrium

between the bulk and surface of LSC is assumed for oxygen-ion exchange.

In order to model the impedance response of the LSC cathode, an overpotential, η , which is measured relative to a reference electrode of the same ambient exposure, is assumed to be applied at the electrode-electrolyte interface. The new reaction equilibrium at the electrode-electrolyte interface can be obtained from Eq. 4.18 as

$$4F\eta = RT \ln f_{O_2}^{solid} - RT \ln P_{O_2}, \quad (4.20)$$

, where the thermodynamic driving force in this case is $4F\eta$, and F is the Faraday constant. Here, the fugacity of oxygen on the surface of LSC, $f_{O_2}^{solid}$, is a function of vacancy mole fraction x_v and temperature. Based on the framework of nonstoichiometry thermodynamics and reaction mechanisms discussed in Sec. 4.1 and Sec. 4.2, the vacancy fraction x_v at the interface can be derived from the newly equilibrated $f_{O_2}^{solid}$, using a procedure similar to the deriving of Eq. 4.19 for a given rate-limiting reaction.

In EIS measurements, the overpotential typically varies in a sinusoidal wave form due to an AC source. The oxygen vacancy concentration responds to this variation and induces the vacancy transport and reaction in the bulk as well as on the surface. Within the bulk of the LSC phase, oxygen transport is mediated by the oxygen vacancy, which is assumed to obey moderate dilute solution theory. Under the assumption of the infinite electronic conductivity of LSC, the oxygen transport is determined by the oxygen vacancy concentration following Fick's first law:

$$C_0 \frac{\partial x_v}{\partial t} = -\nabla \cdot \mathbf{N}_v, \quad (4.21)$$

where \mathbf{N}_v is the bulk vacancy flux

$$\mathbf{N}_v = -C_0 A(x_v) D_v \nabla x_v. \quad (4.22)$$

Here, $A(x_v) = -(1/2)(\partial \ln f_{O_2}^{solid} / \partial \ln x_v)$ is the thermodynamic factor for oxygen vacancies, and D_v is the vacancy diffusivity (assumed to be constant).

On the LSC surface, the deviation of the oxygen vacancy concentration becomes a driving force for the oxygen reduction reaction. This reaction is assumed to follow the rate law of Eq. 4.15, and both the rate prefactor, \mathfrak{R}_0 , and the thermodynamic driving force, Λ , are correlated with the vacancy fraction, x_v . Despite this general rate law for oxygen-reduction reaction, little is known about other possible mechanisms including the accumulation and dissolution of oxygen on the LSC surface. To proceed, a surface layer of an infinitesimal thickness, in which the accumulation of oxygen on the surface is coupled to the oxygen-reduction reaction and the bulk and surface flux of vacancies, is considered.

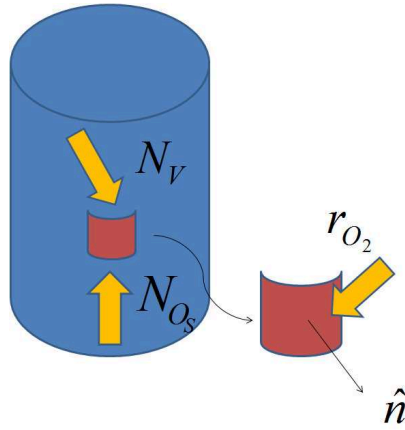


Figure 4.4: A schematic diagram that describes the mass balance at a surface element on mixed conducting oxides. \mathbf{N}_v represents the bulk flux, \mathbf{N}_{O_s} is the surface flux, r_{O_2} is the surface reaction rate, and \hat{n} is the unit normal vector of the surface element.

As shown in Fig. 4.4, the mass balance within a finite element on the LSC surface is thus assumed to be governed by

$$\Gamma_0 \frac{\partial \theta_{O_s}}{\partial t} = -\nabla_s \cdot \mathbf{N}_{O_s} - \hat{n} \cdot \mathbf{N}_v + 2r_{O_2}, \quad (4.23)$$

where \mathbf{N}_{O_s} is the surface vacancy flux (in molecules per meter per second)

$$\mathbf{N}_{O_s} = -\Gamma_0 A_{O_s}(\theta_{O_s}) D_{O_s} \nabla_s \theta_{O_s}. \quad (4.24)$$

Here, $A_{O_s} = -(1/2)(\partial \ln f_{O_2}^{surface} / \partial \ln \theta_{O_s})$ is the surface thermodynamic factor for oxygen vacancies, Γ_0 is the apparent oxygen storage capacity per unit area, θ_{O_s} is the fractional occupancy, D_{O_s} is the apparent surface diffusivity, $\hat{\mathbf{n}}$ is the unit normal vector of the surface element, and r_{O_2} is the rate law for the oxygen reduction reaction.

In EIS measurements, a small amplitude of the sinusoidal perturbation is used. Therefore all equations and boundary conditions can be linearized around the equilibrium of a reference state ($x_v = x_v^0$). In this case, when the applied voltage leads to the overpotential of the form $\eta \approx \tilde{V} \cos(\tilde{\omega}t)$, the current response can be assumed to be $i = (1/2)(\bar{i}e^{j\sigma\tau} + \bar{i}^*e^{-j\sigma\tau})$, where \bar{i}^* is the complex conjugate of the amplitude of the current response \bar{i} . The resulting impedance $Z = \tilde{V}/\bar{i}$.

We may nondimensionalize the governing equations and boundary conditions (BCs) with the nondimensional variables,

$$\phi = \frac{x_v - x_v^0}{x_v^0}, \quad \tau = \frac{tA^0 D_v}{\mathcal{L}^2}, \quad (4.25)$$

where x_v^0 and A^0 are the equilibrium values of x_v and A when in the absence of the applied voltage, and \mathcal{L} is the characteristic length of the LSC microstructure, which is chosen as the length scale for nondimensionalization. Then, the nondimensionalized

governing equations and BCs can be written as

$$\text{LSC bulk:} \quad \frac{\partial \phi}{\partial \tau} = \nabla^2 \phi, \quad (4.26)$$

$$\text{electrode/electrolyte interface: } \phi = -\alpha \cos(\sigma \tau), \quad (4.27)$$

$$\text{far from interface:} \quad \phi = 0, \quad (4.28)$$

$$\text{surface balance:} \quad \xi \frac{\partial \phi}{\partial \tau} = -\hat{n} \cdot \nabla \phi + \kappa \phi + \nu \nabla_s^2 \phi, \quad (4.29)$$

where $\alpha = 2F\tilde{V}/ART$ and $\sigma = \mathcal{L}^2\tilde{\omega}/A^0D_v$ are the dimensionless perturbation amplitude and frequency, respectively. In Eq. 4.29, the three remaining dimensionless parameters κ , ν , and ξ are ratios that characterize the competing processes given by

$$\kappa = \frac{4\mathfrak{R}_0\mathcal{L}}{C_0x_v^0D_v} \equiv \frac{\text{surface oxygen exchange}}{\text{bulk oxygen diffusion}}, \quad (4.30)$$

$$\nu = \frac{\Gamma_0\theta_{O_s}^0D_{O_s}}{\mathcal{L}C_0x_v^0D_v} \equiv \frac{\text{surface oxygen diffusion}}{\text{bulk oxygen diffusion}}, \quad (4.31)$$

$$\xi = \frac{A^0\Gamma_0\theta_{O_s}^0}{A_{O_s}^0\mathcal{L}C_0x_v^0} \equiv \frac{\text{surface oxygen storage}}{\text{bulk oxygen storage}}. \quad (4.32)$$

To solve Eq. 4.26 to Eq. 4.29, we can perform separation of variables of ϕ into spatial and time-dependent components

$$\phi(\vec{r}, \tau) = \frac{1}{2} [\bar{\phi}(\vec{r})e^{j\sigma\tau} + \bar{\phi}^*(\vec{r})e^{-j\sigma\tau}], \quad (4.33)$$

where $\bar{\phi}(\vec{r})$ and its complex conjugate $\bar{\phi}^*(\vec{r})$ are stationary functions that indicate the spatial distribution of the vacancy concentration in response to the perturbation. A set of stationary partial differential equations (PDEs) and BCs can be derived by

substituting Eq. 4.33 into the nondimensionalized governing equations as

$$\text{LSC bulk:} \quad \nabla^2 \bar{\phi} = j\sigma \bar{\phi}, \quad (4.34)$$

$$\text{electrode-electrolyte interface: } \bar{\phi} = -\alpha, \quad (4.35)$$

$$\text{far from interface:} \quad \bar{\phi} = 0, \quad (4.36)$$

$$\text{surface balance:} \quad -\hat{n} \cdot \nabla \bar{\phi} = (\kappa + j\sigma\xi)\bar{\phi} - \nu \nabla_s^2 \bar{\phi}. \quad (4.37)$$

4.4 Model implementation with the smoothed boundary method

In order to apply the dual-path LSC model (Eqs. 4.34 - 4.37) to experimentally obtained microstructures with complex geometry, we utilize the SBM framework to implement this model. The derivation is explained as follows. First, a domain parameter ψ is introduced to distinguish the domain in which the PDEs must be solved from the remainder of the computational domain. This computational domain can have a regular rectangular geometry that is easily meshed into finite difference grids. Shown as an example in Fig. 4.5, the LSC particle is identified as $\psi = 1$ (blue), whereas outside the LSC is identified as $\psi = 0$ (white). The computational domain is indicated by the box surrounding the particle. A pre-smoothing procedure is performed to construct the initial ψ value so that ψ changes smoothly from 0 to 1 over the interfaces.

The governing equation, Eq. 4.34, is then manipulated using ψ and rearranged with the product rule in differentiation to result in

$$j\sigma \bar{\phi} \psi = \nabla \cdot (\psi \nabla \bar{\phi}) - \nabla \psi \cdot \nabla \bar{\phi}. \quad (4.38)$$

To impose the surface balance BC, Eq. 4.37, on Eq. 4.38, the surface unit normal

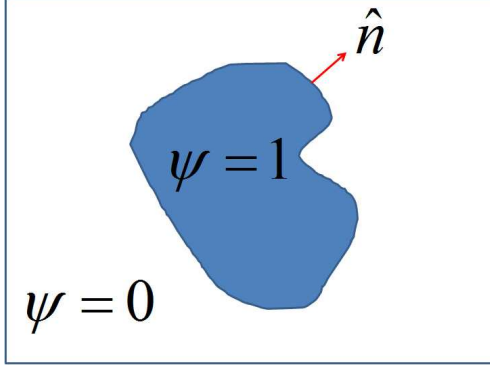


Figure 4.5: A schematic diagram that describes how the domain parameter ψ is introduced in the SBM framework. The irregular shape in the middle is the LSC particle. The rectangular box is the expanded domain for SBM implementation.

vector $\hat{\mathbf{n}}$ is represented in terms of a function of ψ as

$$\hat{\mathbf{n}} = \frac{\nabla\psi}{|\nabla\psi|}. \quad (4.39)$$

Substituting Eq. 4.39 into Eq. 4.37, we obtain

$$\nabla\psi \cdot \nabla\bar{\phi} = |\nabla\psi| [(\kappa + j\sigma\xi)\bar{\phi} - \nu\nabla_s^2\bar{\phi}]. \quad (4.40)$$

The final governing equation that combines both the evolution equation, Eq. 4.34, and the BC on the LSC surface, Eq. 4.37, is obtained by substituting Eq. 4.40 into Eq. 4.38,

$$j\sigma\bar{\phi} = \frac{1}{\psi} \{ \nabla \cdot (\psi \nabla \bar{\phi}) - |\nabla\psi| [(\kappa + j\sigma\xi)\bar{\phi} - \nu\nabla_s^2\bar{\phi}] \}. \quad (4.41)$$

4.5 Results and discussion

4.5.1 Smoothed boundary method validation

To demonstrate the validity of the SBM implementation of the dual-path LSC model, we consider a cylindrical geometry of the LSC phase. We also assume a sim-

plified case where only bulk diffusion and surface reaction mechanisms are important. In addition, we assume that the oxygen storage capacity of the bulk is much larger than that of the surface, which leads to $\xi = 0$, which is a good assumption for LSC. The SBM governing equation can thus be simplified to

$$j\sigma\bar{\phi} = \frac{1}{\psi} \{ \nabla \cdot (\psi \nabla \bar{\phi}) - |\nabla \psi| \kappa \bar{\phi} \}. \quad (4.42)$$

The advantage of modeling such a simplified case is that a semi-analytical solution exists. The analytical solution in this case is a modified Bessel function of the first kind, which is derived in detail in Ref. [19]. In the limit of small κ ($\kappa \sim 1$) and low frequency, $\sigma \sim 1$, an approximation to the analytical solution of dimensionless vacancy concentration $\bar{\phi}$ can be written as

$$\bar{\phi}(z) = e^{-z\sqrt{[(1+2\phi)+2\kappa]/(1+2\nu)}}, \quad (4.43)$$

where z is the cylinder height normalized to the cylinder radius.

The nondimensional parameters in this test are chosen to be $\alpha = -1$, $\kappa = 1$, and $\sigma = 1$ for convenience. The computational domain is arranged according to the conventions of the SBM framework, as shown in Fig. 4.6; that is, $\psi = 1$ within the LSC phase, whereas $\psi = 0$ in the remainder. The bottom of the cylinder was

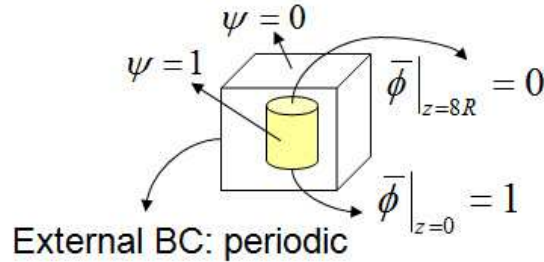


Figure 4.6: The domain configuration for the cylindrical geometry case to demonstrate the validity of the SBM implementation of the LSC model.

considered to be the electrode-electrolyte interface where the sinusoidal perturbation

is applied, i.e., $\bar{\phi} = 1$ according to Eq. 4.35. The solution of Eq. 4.43 indicates that the nondimensional vacancy concentration $\bar{\phi}$ is approximately zero when the length of the cylinder is over five times the cylinder radius (R_{cyd}) for this set of model parameters, i.e., the boundary is far enough from the interface so that Eq. 4.36 applies. Thus, we can safely choose the length of the cylinder to be $8R_{cyd}$ and set $\bar{\phi} = 0$ at the top of the cylinder. Note that, for the ease of computation, the cylindrical domain was embedded in a cubic computational domain with the BCs $\bar{\phi} = 1$ at the bottom and $\bar{\phi} = 0$ at the top, whereas the remaining external boundaries are assumed to be periodic. In the SBM framework, the BCs applied at the domain boundaries where $\psi = 0$ do not affect the results within the domain of interest defined by $\psi = 1$.

Since the governing equation, Eq. 4.42, is only a second-order stationary PDE, the solution was acquired by explicit pseudo-time-stepping methods together with the central-differencing scheme in space. In Fig. 4.7, the finite-difference solution that utilizes SBM is compared with the analytical solution, which is solved numerically using the Fourier sine transformation with Mathematica by Prof. Stuart Adler's group at the University of Washington. The difference between the dimensionless

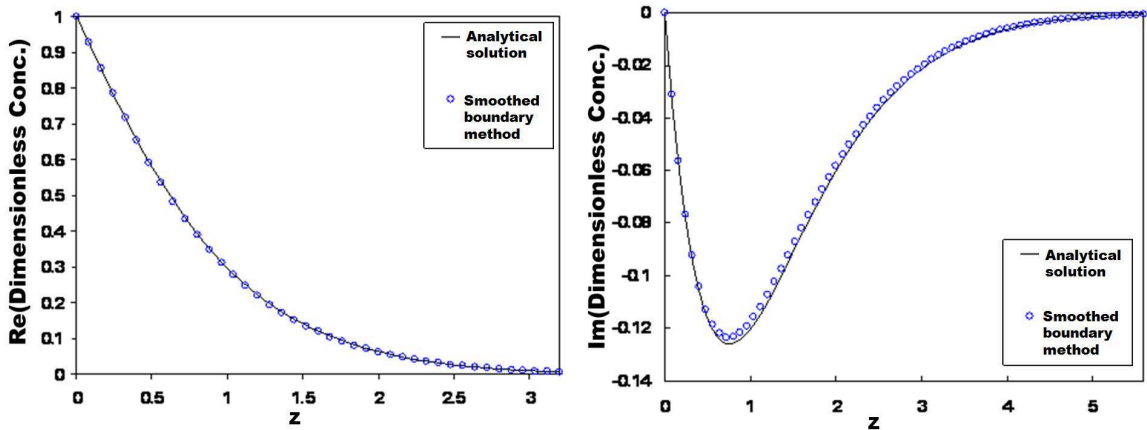


Figure 4.7: A comparison of the analytical solution and the SBM results for a cylinder case. The nondimensional vacancy concentration is plotted versus the cylinder height normalized to the cylinder radius, z .

vacancy concentration $\bar{\phi}$ between the semi-analytical solution and the SBM results

was found to be less than 1% in the real part and less than 4% in the imaginary part. The agreement between the analytical solution and the SBM result demonstrates the applicability of our method to the LSC dual-path model. The error in the solution can be reduced by increasing the resolution of the mesh system and decreasing the thickness of the smoothed boundary in addition to increasing the length of the cylinder to eliminate the domain size effect.

4.5.2 Oxygen vacancy concentration in the experimentally obtained LSC cathode microstructure

We applied the SBM framework described in Sec. 4.4 to model the EIS measurement of an experimentally obtained LSC cathode with complex geometry. The LSC sample modeled here was fabricated by Prof. Stuart Adler's group at the University of Washington, and its microstructure was obtained via FIB-SEM by Prof. Scott Barnett's group at Northwestern University with the instrument at Argonne National Laboratory. The data were cropped to a domain size of 4.8 by 7.5 by 7.4 μm^3 for our simulations, which is shown in Fig. 4.8.

As an initial step in studying the microstructural effects on oxygen reduction and transport in LSC, we considered the simplified case dominated by surface reaction and bulk diffusion. We performed a simulation of the LSC dual-path model for this LSC sample. The logarithm of the magnitude of the dimensionless vacancy concentration is plotted in Fig. 4.9 to represent the utilization lengths (for an AC voltage supplied at the bottom), while the dimensionless vacancy concentration is plotted in Fig. 4.10 to show the microstructural effect (for an AC voltage supplied at the size wall).

The simulation results indicate that when the surface reaction to bulk diffusion ratio is higher, the perturbation to vacancy concentration is more confined to a smaller region near the electrolyte-electrode interface. One important parameter, the utilization length of the material, can be derived analytically for a cylindrical geometry

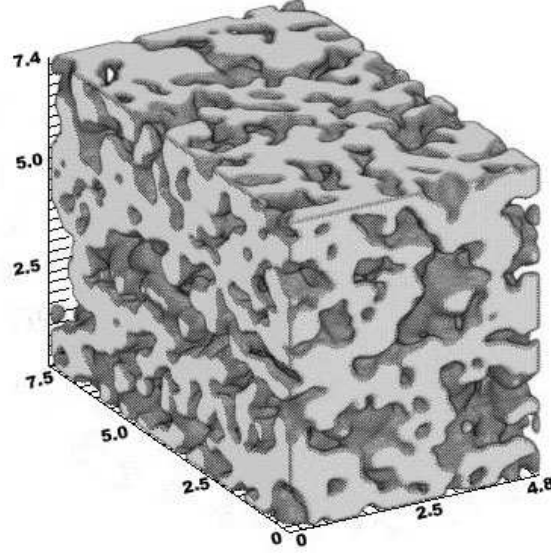


Figure 4.8: A view of the FIB-SEM 3D reconstruction of the LSC cathode. The grey color represents the LSC phase (with a volume fraction of 60.9%), and the transparent space indicates the pores (with a volume fraction of 30.1%).

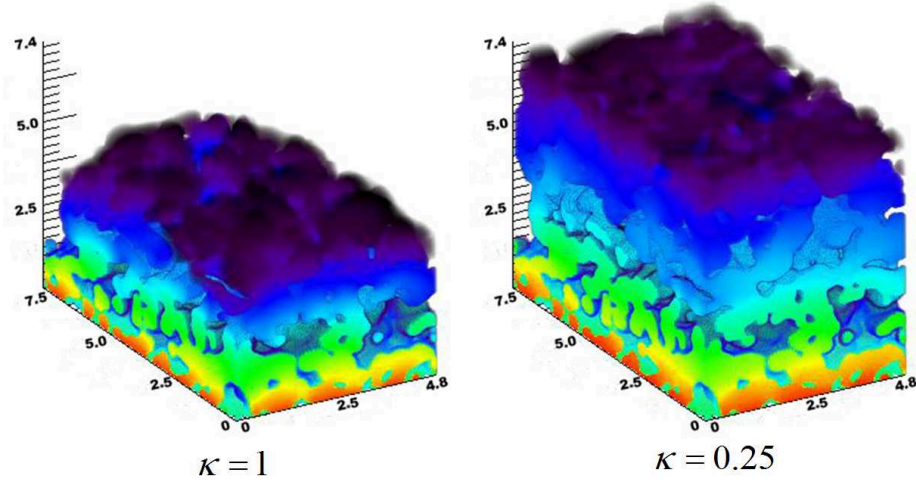


Figure 4.9: A view of the spatial distribution of the dimensionless vacancy concentration in the reconstructed LSC cathode. The color transitions from red to black, which corresponds to high to low logarithm of the concentrations. Note that the distribution is affected locally by the microstructures.

when only the surface reaction and bulk diffusion are considered [19], and it is given by

$$l_\delta \propto \sqrt{\frac{1}{\kappa}}. \quad (4.44)$$

That is, the utilization length of a LSC cylinder is inversely proportional to the square

root of the ratio between the surface reaction and bulk diffusion. The simulation result is qualitatively consistent with this simple relationship, where the $\kappa = 1$ case is expected to have half of the utilization length as compared to the $\kappa = 0.25$ case. However, it is evident in the simulation result that there is inhomogeneity in the magnitude of the dimensionless vacancy concentration, which stems from the underlying microstructure. The inhomogeneity is more apparent as κ increases, or equivalently, as the utilization length decreases. This microstructure effect is manifested when the characteristic length inhomogeneity exists in the specimen, which may result in asymmetric transport within particles of different sizes.

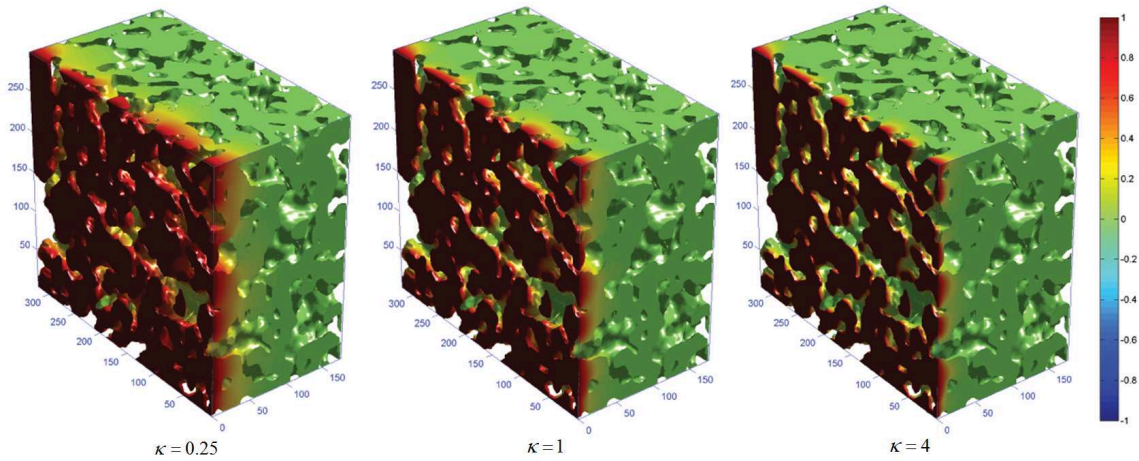


Figure 4.10: A view of the spatial distribution of the dimensionless vacancy concentration in the experimentally acquired LSC cathode, with an AC voltage applied at the side wall. The grid spacing is 25 nm in each axial direction. The utilization length scales inversely with $\sqrt{\kappa}$ in principle, but is affected locally by the microstructures.

By varying the dimensionless frequency, σ , and calculating the impedance, one can obtain the Nyquist plot, where the negative of the imaginary part of the impedance is plotted against the real part of the impedance. The Nyquist plot for the LSC cathode specimen with complex geometry is calculated and is shown in Fig. 4.11, where only the surface reaction and bulk diffusion are considered. Following the standard convention, the impedance values are normalized to the peak imaginary impedance magnitude. Four different surface reactions to bulk diffusion ratios ($\kappa = 0.1, 2.1, 10,$

and 100) are examined. When the reaction kinetics increases, the capacitance effect is weaker, partly due to the shorter utilization length. Therefore, the impedance curve shifts to the right on the Nyquist plot. Thus, when the microstructure is known, it is possible to distinguish systems with different ratios between the surface reaction and bulk diffusion when surface diffusion is known to be negligible.

The spectra on the Nyquist plot acquired via simulations can be compared with experimentally acquired ones to identify or exclude certain transport or reaction mechanisms. For example, the peak frequency at which the peak imaginary impedance occurs can be very different for the surface-path dominant or the bulk-path dominant cases. Depending on the dominant transport mechanism in the mixed conductor, the cathode microstructures may be designed either to maximize the surface area or the bulk volume for optimized performance.

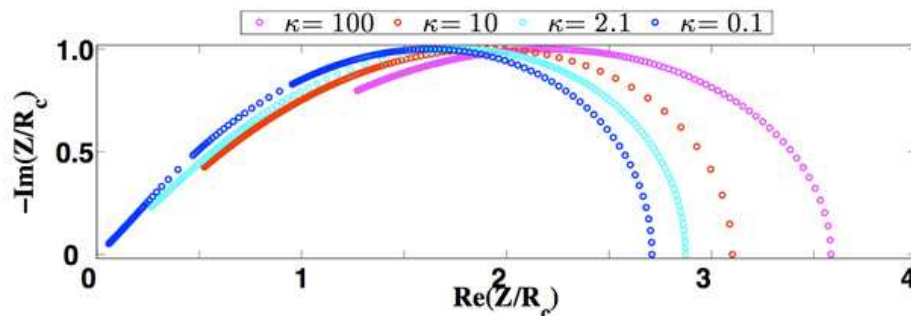


Figure 4.11: The modeled Nyquist plot for the case where the surface transport path is not considered. Each curve contains 200 data points obtained by varying the dimensionless frequency from 0 to 210. (This work was performed by Hui-Chia Yu in Thornton’s group.)

This SBM model framework has now been extended to incorporate surface diffusion in Prof. Thornton’s group at the University of Michigan. The SBM implementation is much more computationally efficient and less labor intensive than the alternative FEM implementation, which requires explicit meshing of the 3D complex geometry, which is tedious and rather difficult. Because creating new meshes is a trivial task, one can use a number of different microstructures, as well as various portions

of the samples, in simulations. This is especially advantageous when active regions can span different volumes, which is the case for the EIS simulations. For example, as shown in Fig. 4.12, when the frequency of the AC excitation is high, to resolve the impedance a much higher resolution of meshes close to the electrode-electrolyte interface is required. In SBM, when the effective utilization length is shorter than or comparable to the grid size, the impedance is not resolvable; however, we would then only need to simulate a small portion of the specimen close to the electrode-electrolyte interface that encloses the electrochemically active regions. The resolution in the direction perpendicular to the interface can be much finer so that the rapid change in concentration along the direction can be resolved accurately. The saving in computation resources and labor is significant, especially when a full spectrum of the Nyquist plot is necessary for interpretation. Our SBM model is thus a powerful tool that can facilitate the interpretation of the EIS measurements and aid microstructural design.

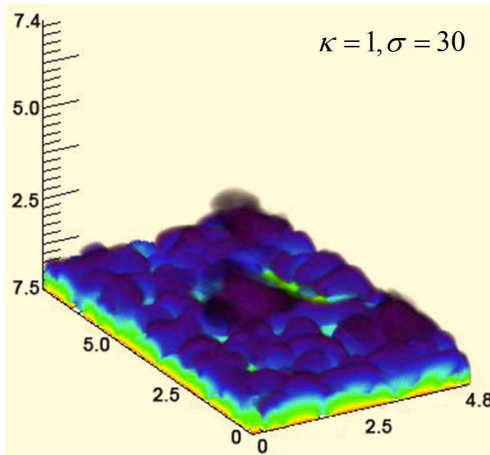


Figure 4.12: The spatial distribution of the dimensionless vacancy concentration in the experimentally obtained LSC cathode (without surface diffusion). Note that at a sufficiently high frequency the utilization length is restricted to a small portion of the specimen height.

CHAPTER V

Summary and Future Work

5.1 Summary of the thesis

This thesis reports research findings that develop our understanding of the relationship between microstructure and properties. Three goals of the work are to identify the characteristics of highly optimized microstructures for competing transport, to elucidate the effects of microstructure evolution during operation on solid oxide fuel cell (SOFC) anodes, and to link microstructures and electrochemical performance of SOFCs. Achieving these goals involves the development of continuum-level models of several different physical phenomena, ranging from diffusion and coarsening to electrochemistry. The target material systems are those that are used as SOFC electrodes. Such systems provide an excellent platform for simulation-based study because they facilitate multiple functions including competing transport and electrochemical reactions, where microstructures play a key role, which hinders investigations that use simpler approaches. Unlike many other theoretical studies that use simplified geometries, we successfully implement geometries for initial conditions and boundary conditions based on microstructures that are experimentally obtained with focused ion beam-scanning electron microscopy (FIB-SEM). State-of-the-art numerical methods, together with parallel computing techniques, are utilized to perform large-scale simulations in three dimensions, which is essential for obtaining accurate

results. The simulations are used to examine the effects of microstructures upon transport, coarsening, and electrochemistry.

The first model, which is described in Chapter 2, evaluates the transport properties of composites. The tortuosity factor is used to characterize the effect of the structure of a phase on its transport properties. A steady-state diffusion equation is solved with a given composite structure to calculate the effective flux, from which the tortuosity factor is calculated. This method is based on the finite-difference method on a Cartesian coordinate, with regular volume meshes, which avoids the explicit meshing of complex geometries.

To examine the multifunctionality of continuous composite materials, tortuosity is used to compare structures with interfaces given by minimal surfaces, as well as structures that form naturally through spinodal decomposition. The spinodally decomposed structure is found to present transport properties that are nearly as efficient as those of minimal-surface structures, which suggests a plausible route to self-assemble two-phase composites that exhibit excellent transport properties.

To demonstrate the broader applicability of this approach, we examine additional microstructures that are experimentally obtained including porous alumina and lanthanum strontium manganite (LSM)-yttria-stabilized zirconia (YSZ) cathodes. In the gelcasted porous alumina study, a relatively large specimen is obtained through a computed tomography (CT) scan (in collaboration with Prof. Katherine Faber at Northwestern University), which provides an opportunity to investigate the size effect in our approach. We find that the size effect is not completely eliminated with the provided specimen due to the low volume fraction ($\sim 22\%$) of pores; instead, it decreases with increasing computational domain size. In the LSM-YSZ cathode study, the slope change in the diagram of tortuosity versus the volume fraction occurring at $\sim 26\text{volume}\%$ indicates a microstructural transition from a highly percolated system to a lower percolated one.

In Chapter 3, Ni coarsening in a Ni-YSZ anode is simulated using two different phase-field models. In Model A, the YSZ phase is considered mobile with a small mobility, and two Cahn-Hilliard equations are coupled to solve the evolution kinetics of this three-phase conserved-field system. In Model B, a stationary YSZ phase is assumed, and the smoothed boundary method (SBM) is utilized to implement the contact-angle and no-flux boundary conditions (BCs) at the YSZ interfaces. Outside the YSZ structure, a one-order-parameter Cahn-Hilliard equation is solved to simulate the Ni coarsening kinetics. The simulation results of these models are linked to experiments via asymptotic analysis, and the model parameters are based on material properties or reasonable assumptions.

To validate our models, the contact angles at a three-phase boundary (TPB) are examined in two dimensions. The contact angles are found to obey Young's equation (of different kinds) in both models. In contrast, a three-phase phase field model that holds one order parameter unchanged is shown to be invalid when TPBs exist. In the case of an experimentally obtained 3D microstructure, we find a reasonable agreement of TPB reductions between some of our Model B simulations and experimental results, but the microstructural variation in different samples can lead to different TPB densities. Model A, however, overestimates the TPB reduction due to its excess mobility at the TPBs.

Error analysis and size-effect studies are further conducted. With the model parameters and the grid system we selected, no obvious boundary effects or contact-angle deviation are found; however, a larger computational domain may be needed to represent the entire experimentally obtained specimen. In addition, a parametric coarsening study with various Ni-YSZ interfacial energies demonstrates that reducing the contact angle of the Ni phase on YSZ, by impurity doping for instance, can enhance the stability of the Ni-YSZ anode.

Furthermore, the evolution of an experimentally obtained anode microstructure is

systematically examined in terms of the active TPBs, the active Ni surface area, and the tortuosity of pores. We find that the phase connectivity, which is highly related to the volume fraction, can have a profound effect on microstructure evolution. More specifically, the active phase clusters, which typically have a larger characteristic length evolve slower, while the isolated clusters of smaller length scales evolve faster. In contrast, the reduction trend of active TPB density is found to agree well with the total TPB density during coarsening, and the active TPB reduction accounts for most of the total TPB reduction. The evolution of TPBs is thus only indirectly correlated to the coarsening kinetics.

In Chapter 4, an electrochemical model that considers the oxygen reaction, surface diffusion, and bulk diffusion mechanisms in a mixed-conducting SOFC cathode is implemented with the SBM framework. This dual-transport-path electrochemical model is developed to aid the interpretation of electrochemical impedance spectroscopy (EIS) measurements. The nonstoichiometry thermodynamics, rate laws, and reaction kinetics on which this dual-transport-path model is based are briefly reviewed. The SBM framework that facilitates the implementation of this model on complex geometries is then derived.

A simulation using the dual-transport-path model with only bulk diffusion and surface reaction mechanisms is conducted in a cylindrical cathode. The excellent agreement between simulation results and analytical solution demonstrates the validity of the SBM implementation. An experimentally obtained LSC cathode is used as the geometry for simulations. We find that, although the utilization length of the material follows the macrohomogeneous solution in general, the vacancy concentration varies locally due to the microstructure. This effect becomes significant when the utilization length is short compared to the characteristic length of the microstructural inhomogeneity. Furthermore, Nyquist plots are presented for various excitation frequencies in addition to the different ratios between bulk diffusion and surface re-

action rates. This SBM implementation is much more efficient computationally and being less labor intensive in comparison to the alternative FEM implementation, and can thus facilitate the interpretation of the EIS measurements and microstructural design.

5.2 Future Work

Many of our coarsening simulations offer insights into how to design more robust microstructures for Ni-YSZ anodes. However, an electrochemical model that can directly link the microstructural effects and the electrode performance still awaits development. An electrochemical model that considers the assembly of the electrodes and the electrolyte is desirable because it can evaluate the cell performance by accounting for the electrode microstructures. For example, a resistor network model may be used [7]. This model considers the conservation of electrical charges and gas species using a finite volume method. In an example of a SOFC anode, as shown in Fig. 5.1, each of the finite volume elements is assigned to be one of the Ni, pore, YSZ, or TPB element based on the microstructure, in which the material properties, including the electrical and ionic conductivities, are assigned accordingly. The conservation of charges can then be solved by Ohm's law. As schematically shown in Fig. 5.2, the boundary conditions of the 3D computation domain can be approximated with the one-dimensional macrohomogeneous solutions.

In addition, electrodes with candidate microstructures of simple geometries or those fabricated by novel techniques can be simulated with our models to examine their stability and multifunctionality. For example, textured Ni-YSZ cermets prepared by the reduction of directionally solidified eutectics have been shown to possess good metal-ceramic adhesion and may present long-term stability as a SOFC anode material [8]. The formation of alternating lamellae using this fabrication process is shown in Fig. 5.3.

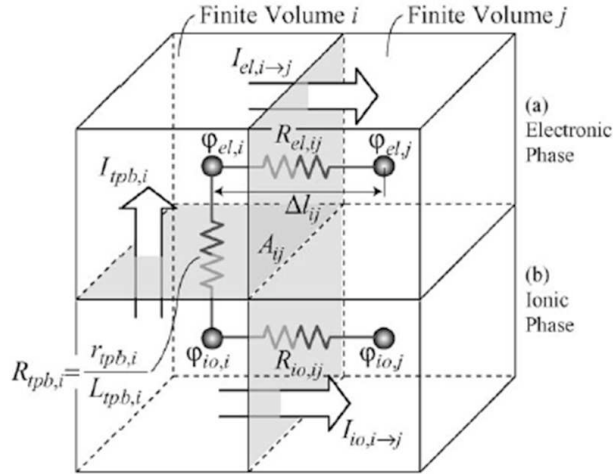


Figure 5.1: A schematic diagram showing the finite volume scheme used in the resistor network model [7]. Each of the finite volume elements is assigned to a material property according to the microstructural configuration. The conservation of charges can then be solved with Ohm's law.

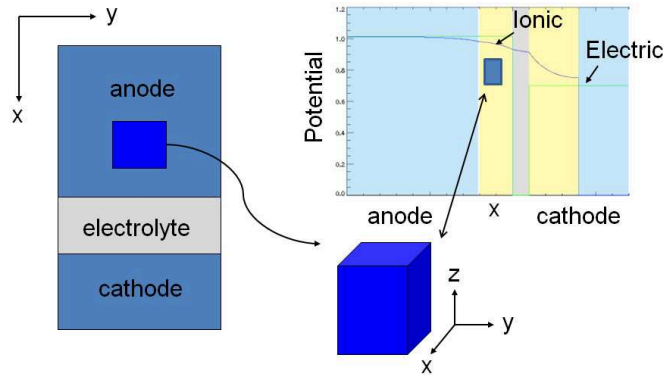


Figure 5.2: A schematic diagram describing how the simulation results of the 1D electrochemical model (top right) can be used as the boundary conditions for the 3D model, which employs the experimentally obtained microstructure (shown as the cube in the bottom).

Experiments have revealed that electrochemistry may have a profound effect on coarsening [80]. In principle, such effects can be incorporated into our models. Experiments that are being conducted in Prof. Scott Barnett's group will help validate our models and assumptions as well as guide their improvement. Polycrystallinity and surface diffusion mechanisms may also have effects on transport properties and may require further investigation.

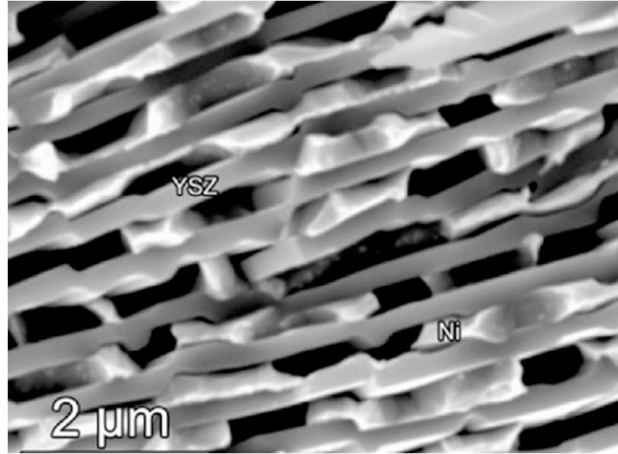


Figure 5.3: SEM image of the textured Ni-YSZ cermet prepared by the reduction of directionally solidified NiO-YSZ eutectics. The lamellar interspacing is a function of growth rate. [8]

In the SBM implementation of the mixed-conductor model, developing an adaptive mesh scheme is desirable because higher computational efficiency and numerical accuracy can be achieved by allowing the flexibility of employing adaptively finer meshes in the interfacial regions while retaining coarse grids in the remainder of the computation domain. The adaptive mesh can also facilitate EIS modeling, especially at high AC frequencies, because it circumvents the need for volume cropping and remeshing. Implementing the adaptive mesh will also benefit large-scale simulations and accelerate other types of models.

BIBLIOGRAPHY

BIBLIOGRAPHY

- [1] R.J. Kee, P. Korada, K. Walters, and M. Pavol. *Journal of Power Sources*, 109:148–159, 2002.
- [2] D. Simwonis, F. Tietz, and D. Stover. *Solid State Ionics*, 132:241–251, 2000.
- [3] J. R. Wilson, W. Kobsiriphat, R. Mendoza, H. Chen, J. M. Hiller, D. J. Miller, K. Thornton, P. W. Voorhees, S. B. Adler, and S. A. Barnett. *Nature Materials*, 5(7):541–544, 2006.
- [4] Y. Kwon, K. Thornton, and P. W. Voorhees. *Phys. Rev. E*, 75:021120, 2007.
- [5] H.-Y. Chen, Y. Kwon, and K. Thornton. *Scripta Materialia*, 61:52–55, 2009.
- [6] S.B. Adler. *Chemical Review*, 104:4791–4843, 2004.
- [7] J. H. Nam and D. H. Jeon. *Electrochimica Acta*, 51:3446, 2006.
- [8] A. Larrea, M.A. Laguna-Bercero, J.I. Pena, R.I. Merino, and V.M. Orera. *Central European Journal of Physics*, 7:242–250, 2009.
- [9] J. Will, A. Mitterdorfer, C. Kleinlogel, D. Perednis, and L.J. Gauckler. *Solid State Ionics*, 131:79–96, 2000.
- [10] K. Kendall. *International Materials Reviews*, 50(5):257, 2005.
- [11] K. Sasaki, J.P. Wurth, R. Gschwend, M. Godickemeier, and L.J. Gauckler. *Solid State Ionics*, 143:530–543, 1996.
- [12] M. Kleitz and F. Petitbon. *Solid State Ionics*, 92:65–74, 1996.
- [13] P. Singh and N. Q. Minh. *Int. J. Appl. Ceram. Technol.*, 1:5, 2004.
- [14] M.H.R. Lankhorst, H.J.M. Bouwmeester, and H. Verweij. *Physical Review Letters*, 77(14):555–567, 1996.
- [15] M.H.R. Lankhorst, H.J.M. Bouwmeester, and H. Verweij. *Journal of Solid State Chemistry*, 133:555–567, 1997.
- [16] S.B. Adler, X.Y. Chen, and J.R. Wilson. *Journal of Catalysis*, 245:91–109, 2007.

- [17] F.S. Baumann, J. Fleig, M. Konuma, U. Starke, H.-U. Habermeier, and J. Maier. *Journal of The Electrochemical Society*, 152:A2074–A2079, 2005.
- [18] S.B. Adler, J.A. Lane, and B.C.H. Steele. *Journal of Electrochem. Soc.*, 143(11):3554–3564, 1996.
- [19] Y.X. Lu, C. Kreller, and S.B. Adler. *Journal of Electrochem. Soc.*, 156(4):B513–B525, 2009.
- [20] S. Campanari and P. Iora. *Journal of Power Sources*, 132:113–126, 2004.
- [21] N. Autissier, D. Larrain, J. Van herle, and D. Favrat. *Journal of Power Sources*, 131:313–319, 2004.
- [22] H. Yakabe, T. Ogiwara, M. Hishinuma, and I. Yasuda. *Journal of Power Sources*, 102:144–154, 2001.
- [23] P. Costamagna, P. Costa, and V. Antonucci. *Electrochimica Acta*, 43:375–394, 1998.
- [24] H.Zhu, R.J. Kee, V.M. Janardhanan, O. Deutschmann, and D.G. Goodwin. *Journal of The Electrochemical Society*, 1:A2427–A2440, 2005.
- [25] A.M. Svensson, S. Sunde, and K. Nisancioglu. *Journal of The Electrochemical Society*, 144:2719–2732, 1997.
- [26] V.G.M. Sivel, J. Van Den Brand, W.R. Wang, H. Mohdadi, F.D. Tichelaar, P.F.A. Alkemade, and H.W. Zandbergen. *Journal of Microscopy*, 214:237–245, 2004.
- [27] L.A. Giannuzzi and F.A. Stevie. *Introduction to Focused Ion Beams, Instrumentation, Theory, Techniques and Practice*. Springer Science+Business Media, Inc., Springer Science+Business Media, Inc., 233 Spring St., New York, NY 10013, 2005.
- [28] G.W. Milton. *The Theory of Composites*. Cambridge University Press, The Edinburgh Building, Cambridge CB2 2RU, UK, first edition, 2002.
- [29] Z. Hashin and S. Shtrikman. *J. Appl. Phys.*, 33:3125, 1962.
- [30] D. J. Bergman. *Phys. Rep.*, (9):377, 1978.
- [31] S. Prager. *The Journal of Chemical Physics*, 50(10):4305–4312, 1969.
- [32] S. Torquato and S. Hyun. *J. Appl. Phys.*, 89:1725, 2001.
- [33] S. Torquato, S. Hyun, and A. Donev. *Phys. Rev. Lett.*, 89(26):266601, 2002.
- [34] S. Torquato, S. Hyun, and A. Donev. *J. Appl. Phys.*, 94(9):5748, 2003.
- [35] L. Silvestre. *Proc. R. Soc. A*, 463:2543, 2007.

- [36] J. A. F. Plateau. *Statique Experimentale et Theorique des Liquides aus Seules Forces Moleculaires*, volume 2. Gauthier-Villars, Paris, 1873.
- [37] H. A. Schwarz. *Gesammelte Mathematische Abhandlung*, volume 1. Springer, Berlin, 1890.
- [38] O. Bonnet. *Note sur la Theorie Generale des Surfaces*, volume 37. Comptes Rendus, 1853.
- [39] E.R. Neovius. *Bestimmung Zweier Speciellen Periodischen Minimalflächen*. J.C.Frenkel, Helsingfors, 1883.
- [40] A. H. Schoen. *Nat. Aero. Space Adm. Tech. Note*, D5541, 1970.
- [41] L. E. Scriven. *Nature*, 263:123, 1976.
- [42] E. L. Thomas, D. M. Anderson, C. S. Henkee, and D. Hoffman. *Nature*, 334:598, 1988.
- [43] W. Longley and T.J. McIntosh. *Nature (London)*, 303:612, 1983.
- [44] F. S. Bates and G. H. Fredrickson. *Physics Today*, 52:32–38, 1999.
- [45] D.A. Hajduk, S.M. Gruner, P. Rangarajan, R.A. Register, L.J. Fetters, C. Honeker, R.J. Albalak, and E.L. Thomas. *Macromolecules*, 27:490–501, 1994.
- [46] P. Schmidt-Winkel, W.W. Lukens Jr., P. Yang, D.I. Margolese, J.S. Lettow, J.Y. Ying, and G.D. Stucky. *Chem. Mater.*, 12:686–696, 2000.
- [47] T. Liu, C. Burger, and B. Chu. *Prog. Polym. Sci.*, 28:5–26, 2003.
- [48] M. Maldovan and E.L. Thomas. *Nature Materials*, 3:593–600, 2004.
- [49] L.A. Smith and P.X. Ma. *Colloids and Surfaces*, 39:125–131, 2004.
- [50] L.A. Smith, X. Liu, and P.X. Ma. *Soft Matter.*, 4:2144–2149, 2008.
- [51] Y. Lu, Y. Yang, A. Sellinger, M. Lu, J. Huang, H. Fan, R. Haddad, G. Lopez, A.R. Burns, D.Y. Sasaki, J. Shelnett, and C.J. Brinker. *Nature*, 410:913–917, 2001.
- [52] U.S. Schwarz and G. Gompfer. *Physical Review E*, 59:5528–5540, 1999.
- [53] W. T. Gozdz and R. Holyst. *Phy. Rev. E*, 54:5012, 1996.
- [54] R. Nesper and H.G. von Schnering. *Angew Che. Int. Ed. Engl.*, 25:110–112, 1986.
- [55] H.G. von Schnering and R. Nesper. *Angew Che. Int. Ed. Engl.*, 26:1059–1080, 1987.

- [56] E.J. Siem and W.C. Carter. *Interface Sci.*, 10:287, 2002.
- [57] L. Yunfeng, Y. Yang, A. Sellinger, M. Lu, J. Huang, H. Fan, R. Haddad, G. Lopez, A. R. Burns, D. Y. Sasaki, J. Shelnut, and C. J. Brinker. *Nature*, 410:913, 2001.
- [58] Y. Jung and S. Torquato. *Phys. Rev. E*, 72:056319, 2005.
- [59] R. Mori, M. Takahashi, and T. Yoko. *J. Mater. Res.*, 21:270–275, 2006.
- [60] A. Gaudon, A. Dager, A. Lecomte, B. Soulestin, and R. Guinebretiere. *J. of the Eur. Ceram. Soc.*, 25:283–286, 2005.
- [61] V.N. Burganos. *Journal of Chemical Physics*, 109:6772–6779, 1998.
- [62] G.L. Vignoles. *Journal de Physique IV*, 5:159–166, 1995.
- [63] J.M. Zalc, S.C. Reyes, and E. Iglesia. *Chem. Eng. Sci.*, 59:2947–2960, 2004.
- [64] N. Epstein. *Chem. Eng. Sci.*, 44(3):777, 1989.
- [65] S. Zhou and Qing Li. *J. Phys. D: Appl. Phys.*, 40:6083, 2007.
- [66] R. Mendoza, I. Savin, K. Thornton, and P. W. Voorhees. *Nat. Mater.*, 3:385, 2004.
- [67] F. Zhao, Y. Jiang, G.Y. Lin, and A.V. Virkar. In H. Yokokawa and S.C. Singhal, editors, *Solid Oxide Fuel Cells VII*, pages 501–510. The Electrochemical Society Proceedings Series, Pennington, NJ, 2001.
- [68] J.R. Wilson, J.S. Cronin, A.T. Duong, S. Rukes, H.-Y. Chen, K. Thornton, D.R. Mumm, and S. A. Barnett. *Journal of Power Sources*, 195:1829–1840, 2010.
- [69] Muhammad Sahimi. *Applications of Percolation Theory*. Taylor and Francis Ltd, Taylor and Francis Inc., 1900 Frost Road, Suite 101, Bristol PA 19007, 1994.
- [70] A. Atkinson, S. Barnett, R. J. Gorte, J.T.S. Irvine, A.J. Mcevoy, M. Mogensen, S.C. Singhal, and J. Vohs. *Nature Materials*, 3:17–27, 2004.
- [71] S. M. Haile. *Materials Today*, 18:24–29, 2003.
- [72] H. Yokokawa, H. Tu, B. Iwanschitz, and A. Mai. *J. Power Sources*, 182:400–412, 2008.
- [73] H. Tu and U. Stimming. *J. Power Sources*, 127:284–293, 2004.
- [74] A. Hagen, R. Barfod, P. V. Hendriksen, Y.-L. Liu, and S. Ramousse. *J. Electrochem. Soc.*, 153(6):A1165, 2006.

- [75] A. Hagen, Y. L. Liu, R. Barfod, and P. V. Hendriksen. *J. Electrochem. Soc.*, 155(10):B1047, 2008.
- [76] J. Malzbender, R.W. Steinbrech, and L. Singheiser. *Fuel Cells*, 9(6):785–793, 2009.
- [77] M. Mogensen and S. Skaarup. *Solid State Ionics*, 86-88:1151, 1996.
- [78] S. Sunde. *J. Electrochem. Soc.*, 142(4):L50, 1995.
- [79] J. Mizusaki, S. Tsuchiya, K. Waragai, H. Tagawa, Y. Arai, and Y. Kuwayama. *J. Am. Ceram. Soc.*, 79:109–113, 1996.
- [80] Karl Thyden. *Microstructural Degradation of Ni-YSZ Anodes for Solid Oxide Fuel Cells*. PhD thesis, University of Copenhagen, H.C. Ørsted Institute, Risoe National Laboratory for Sustainable Energy, DK-4000 Roskilde, Denmark, March 2008.
- [81] P. Tanasini, M. Cannarozzo, P. Costamagna, A. Faes, J.V. Herle, A. Hessler-Wyser, and C. Comninellis. *Fuel Cells*, 9(5):740–752, 2009.
- [82] A.A. Kornyshev A. Ioselevich and W. Lehnert. *J. Electrochem. Soc.*, 144(9):3010, 1997.
- [83] A.A. Kornyshev A. Ioselevich and W. Lehnert. *Solid State Ionics*, 124:221, 1999.
- [84] R. Vaßen, D. Simwonis, and D. Stover. *J. Mater. Sci.*, 36:147, 2001.
- [85] V. L. Ginzburg and L. D. Landau. *J. Exptl. Theoret. Phys. (U.S.S.R.)*, 20:1064, 1950.
- [86] J. W. Cahn and J. Hilliard. *J. Chem. Phys.*, 28:258–267, 1958.
- [87] J. S. Langer. *Directions in Condensed Matter Physics*, volume 1. World Scientific, Singapore, 1986.
- [88] S. M. Allen and J. W. Cahn. *Acta Metall. Mater.*, 27:1085, 1979.
- [89] A.A. Wheeler, W.J. Boettinger, and G.B. Mc Fadden. *Physical Review A*, 45(10):7424–7439, 1992.
- [90] G. Caginalp. *Arch Rat. Mech. Anal.*, 92:205–245, 1986.
- [91] A. Karma and W.J. Rappel. *Physical Review E*, 57:4323–4349, 1997.
- [92] J.A. Warren and B.T. Bruce. *Modelling Simul. Mater. Sci. Eng.*, 4:215–229, 1996.
- [93] B. Nestler, H. Garcke, and B. Stinner. *Physical Review E*, 71:041609, 2005.

- [94] R. Folch and M. Plapp. *Phys. Rev. E*, 72:011602–1, 2005.
- [95] H.-Y. Chen, H.-C. Yu, J. S. Cronin, J. R. Wilson, S. A. Barnett, and K. Thornton. *J. Power Sources*, 196:1333–1337, 2011.
- [96] W. Hackbusch and S. Sauter. *Num. Math.*, 75:447–472, 1997.
- [97] C.A. Duarte, I. Babuska, and J.T. Oden. *Comp. Struct.*, 77:215–232, 2000.
- [98] Y. Gong, B. Li, and Z. Li. *SIAM Journal on Numerical Analysis*, 46:472–495, 2008.
- [99] R. Mittal and G. Iaccarino. *Annu. Rev. Fluid Mech.*, 37:239–261, 2005.
- [100] H. Ji, F.-S. Lien, and E. Yee. *Int. J. Numer. Meth. Fluids*, 52:723–748, 2006.
- [101] J. Kockelkoren, H. Levine, and W.-J. Rappel. *Physical Review E*, 68:037702, 2003.
- [102] A. Bueno-Orovio and V. M. Perez-Garcia. *Numer. Meth. Part. D E*, 22:435–448, 2006.
- [103] A. Bueno-Orovio, V.M. Perez-Garcia, and F.H. Fenton. *SIAM J. Sci. Comput.*, 28:886–900, 2006.
- [104] H.-C. Yu, H.-Y. Chen, and K. Thornton. *arXiv:0912.1288*, 2009.
- [105] X. Li, J. Lowengrub, A. Ratz, and A. Voigt. *Communications in Mathematical Sciences*, 7:81–107, 2009.
- [106] A. I. Zaitsev and N. E. Zaitseva. *High Temperature*, 40(2):197–202, 2002.
- [107] J. M. Blakely and H. Mykura. *Acta Metall. Mater.*, 9:23–31, 1961.
- [108] P.S. Maiya and J.M. Blakely. *J. Appl. Phys.*, 38:698, 1967.
- [109] W. F. Gale and T. C. Totemeier. *Smithells Metals Reference Book*. Elsevier, 8th edition, 2004.
- [110] N. Moelans. *Acta Materialia*, 2010. doi:10.1016/j.actamat.2010.10.038.
- [111] J. A. Warren, T. Pusztai, L. Kornyei, and L. Gransay. *Phy. Rev. B*, 79:014204, 2009.
- [112] R. W. Balluffi, S. M. Allen, and W. C. Carter. *Kinetics of Materials*. John Wiley and Sons, Inc, John Wiley and Sons Inc., 111 River Street, Hoboken, NJ 07030, 2005.
- [113] S. M. Wise, J. S. Lowengrub, J. S. Kim, and W. C. Johnson. *Superlattices Microstruct.*, 36:293–304, 2004.

- [114] D.-H. Yeon, P.-R. Cha, and M. Grant. *Acta Mater.*, 54:1623–1630, 2006.
- [115] E.G. Seebauer and C.E. Allen. *Progress in Surface Science*, 49(3):263–330, 1995.
- [116] R. T. Tung and W. R. Graham. *Surf. Sci.*, 97:73, 1980.
- [117] T.Y. Fu and T.T. Tsung. *Surf. Sci.*, 454-456:571, 2000.
- [118] M. Kilo, M.A. Taylor, C. Argirusis, and G. Borhardt. *J. Appl. Phys.*, 94(12):7547–7552, 2003.
- [119] Akash and M.J. Mayo. *J. Mater. Sci.*, 35:437, 2000.
- [120] B. Derby and C.-D. Qin. *Acta Metall. Mater.*, 40:S53, 1992.
- [121] N. Ma, Q. Chen, and Y. Wang. *Scripta Materialia*, 54:1919–1924, 2006.
- [122] X. Mantzouris, N. Zouvelou, D. Skarmoutsos, P. Nikolopoulos, and F. Tietz. *Journal of Materials Science*, 31:2471–2475, 2005.
- [123] A. Tsoga, A. Naoumidis, and P. Nikolopoulos. *Acta Mater.*, 44(9):3679–3692, 1996.
- [124] Ballabio G., Bernasconi M., Pietrucci F., and Serra S. *Phys. Rev. B*, 70:075417, 2004.
- [125] A. Tsoga and P. Nikolopoulos. *Journal of Materials Science*, 31:5409–5413, 1996.
- [126] A. Christensen and E.A. Carter. *J. Chem. Phys.*, 114(13):5816–5831, 2001.
- [127] J.I. Beltran, S. Gallego, J. Cerda, J.S. Moya, and M.C. Munoz. *Phys. Rev. B*, 68:075401, 2003.
- [128] J. R. Wilson, M. Gameiro, K. Mischaikow, W. Kalies, P. W. Voorhees, and S. A. Barnett. *Microscopy and Microanalysis*, 15:71–77, 2009.
- [129] K. Palagyi and A. Kuba. *Pattern Recogn. Lett.*, 19:613, 1998.
- [130] J. H. Kim, W. K. Liu, and C. Lee. *Comput. Mech.*, 44:683–703, 2009.
- [131] D. J. Seol, S. Y. Hu, Z. K. Liu, S. G. Kim, K. H. Oh, and L. Q. Chen. *J. Appl. Phys.*, 98:044910, 2005.
- [132] J.R. Wilson, J.S. Cronin, and S.A. Barnett. *Scripta Materialia*, 2010. submitted.
- [133] J.B. Torrence and P. Lacorro. *Journal of Solid State Chemistry*, 90:168–172, 1991.
- [134] J. Zannen, G.A. Sawatzky, and J.W. Allen. *Physical Review Letter*, 55:418–421, 1985.